Stellingen

behorende bij het proefschrift
"The spins of resonances in reactions of neutrons with ^{238}U and ^{113}Cd"
Frank Gunsing

1. De kennis van de spins van neutronenresonanties is noodzakelijk voor een correcte interpretatie van zowel metingen van de schending van pariteit als van de schending van tijdsomkeerbaarheid invariantie.
   dit proefschrift

2. Hoewel men voor het zogenaamde "sign effect" in de metingen van schending van pariteit in atoomkernen heeft gezocht naar fysische oorzaken, kan niet worden uitgesloten dat het effect op statistische gronden berust.
   C. M. Frankle et. al. *Phys. Rev. Lett.* **67**(5) (1991) 564

3. Bij experimenten voor schending van pariteit door meting van de voorwaarts-achterwaarts asymmetrie na neutronvangst dient rekening gehouden te worden met de door terugstoot veroorzaakte anisotropie in de hoekverdeling.

4. De moeilijkheid om de invloed van wolken in klimaatmodellen te betrekken lijkt gerelateerd aan de problemen om het weer te voorspellen.
   J. T. Kiehl, *Physics Today*, (nov. 1994) 36

5. Het is mogelijk dat een vrij, niet-relativistisch elektron zich met uniforme snelheid voortbeweegt en daarbij elektromagnetische straling uitzendt.
   J. M. Vigoureux, *Pure Appl. Opt.* **2** (1993) 189

6. De kennis van de resonante werkzame doorsnede van de ^{8}Be + α reactie is van levensbelang aangezien die het hoge stellaire voorkomen van ^{12}C verklaart.
   C. Rolfs and W. Rodney, *Cauldrons in the Cosmos*, University of Chicago Press (1988)
   H. Oberhummer et. al., Proc. 7th Workshop on Nuclear Astrophysics, Ringberg Castle, Germany (1993) 119

7. De mate van alignering van begintoestanden van secondaire gammastraling na neutronvangst in een kern met een spin ongelijk aan nul, is te berekenen binnen het kader van het statistische model en vormt een methode om *p*-golf resonantiespins te bepalen.
   dit proefschrift

8. Men zou verwachten dat de bestuurbaarheid van een land omgekeerd evenredig is met het aantal regeringen dat het heeft. De Belgische staatshervorming, die dat aantal op zes heeft gebracht, lijkt echter goed te functioneren.

9. Bij de ontwikkeling van de elektronische snelweg moet niet over het hoofd worden gezien het publiek over een auto en een rijbewijs te laten beschikken.

10. Transmutatie van langlevend kernafval is een variatie op het principe van de Steen der Wijzen die echter grondig onderzocht moet worden alvorens ze met scepsis van de hand te wijzen.

11. De meest interessante delen van opnamen van een muziekgezelschap zijn vaak de opmerkingen tussen de nummers door.

The spins of resonances in reactions of neutrons with ^{238}U and ^{113}Cd

Frank Gunsing

Dit proefschrift is goedgekeurd door de promotor:
Prof. dr. H. Postma.

This thesis is based on research performed under the daily direction of dr. F. Corvi.

This investigation is part of the research programme of the Joint Research Centre of the European Union and has been carried out at the Institute of Reference Materials and Measurements (IRMM) in Geel, Belgium.

CIP-GEGEVENS KONINKLIJKE BIBLIOTHEEK, DEN HAAG

Gunsing, Frank

The spins of resonances in reactions of neutrons with ^{238}U and ^{113}Cd
Frank Gunsing. - [S.l. : s.n.]. - Ill., fig., tab.
Proefschrift Technische Universiteit Delft. -
Met lit. opg. - Met samenvatting in het Nederlands.
ISBN 90-9007923-8
NUGI 812
Trefw.: kernfysica / neutronen.

The spins of resonances in reactions of neutrons with ^{238}U and ^{113}Cd

De spins van resonanties in reacties van neutronen met ^{238}U en ^{113}Cd

PROEFSCHRIFT

ter verkrijging van de graad van doctor
aan de Technische Universiteit Delft,
op gezag van de Rector Magnificus Prof. ir. K. F. Wakker,
in het openbaar te verdedigen ten overstaan van een commissie,
door het College van Dekanen aangewezen,
op maandag 20 februari 1995 te 10.30 uur

door

Franciscus Albertus GUNSING

natuurkundig ingenieur,
geboren te Amsterdam.

Table of contents

List of symbols

symbol	description	unit
A	nuclear mass number	–
C	detector counts	–
D	nuclear level spacing	eV
E_γ	gamma-ray energy	keV
E_G	giant resonance energy	MeV
E_p	p-wave resonance energy	eV
E_s	s-wave resonance energy	eV
f_n	neutron polarization	–
g	statistical spin factor	–
I	target nucleus spin	units $\hbar$
J	compound nucleus spin	units $\hbar$
j	total neutron spin	units $\hbar$
k_{XL}	reduced photon strength function for XL radiation	$\mathrm{MeV}^{-(2L+1)}$
$\boldsymbol{k}$	neutron wave vector	–
ℓ	angular momentum	units $\hbar$
M	root mean squared PNC matrix element	meV
n	number of neutrons in the beam	
N	neutron number	–
N	number of nuclei in target	atoms / barn
P	longitudinal asymmetry	–
s	neutron spin	units $\hbar$
S_{XL}	photon strength function for XL radiation	$\mathrm{MeV}^{-(2L+1)}$

T	nuclear temperature	MeV
V_{sp}	weak interaction matrix element	eV
Z	proton number	–
Γ	total resonance width	eV
Γ_G	giant resonance width	MeV
Γ_n	neutron width	eV
Γ_n^p	neutron p-wave resonance width	eV
Γ_n^s	neutron s-wave resonance width	eV
Γ_γ	gamma radiation width	eV
Γ^{PNC}	parity nonconserving spreading width	eV
ϑ	angle between the normal of sample and neutron beam	degrees
λ	neutron wave length	m
ν	gamma-ray multiplicity	–
σ_G	giant dipole resonance cross section	barn
σ_p	p-wave resonance cross section	barn

BSF	backshifted Fermi gas level density
CRLB	Cramér-Rao lower bound
CTF	constant temperature level density
PNC	parity nonconservation
RV	random variable

Summary

In this thesis experiments are described that have lead to the assignments of spins to a large number of resonances in reactions of epithermal neutrons with the nuclei ^{238}U and ^{113}Cd. When a neutron is captured by an atomic nucleus, a compound nucleus is formed which is in a highly excited state with an energy of the order of the neutron binding energy. If the kinetic neutron energy is varied around a state of the compound nucleus, one observes a peak in the cross section. This is called a resonance in the reaction. Dependent on the amount of orbital momentum ℓ that the neutron adds to the system, the resonances are indicated with spectroscopic notations as *s*- and *p*-waves for $\ell = 0$ and 1 respectively. The purpose of this thesis is to determine the spins of such resonances.

It appears that the population of certain states by gamma radiation from the decaying compound nucleus is dependent on the spin of the resonance. The resonance spin can be determined by measuring the relative intensity of specific gamma rays. The spin dependence can be enlarged by taking the ratio of two gamma transitions having opposite spin effects. Therefore it is no more necessary to normalize the intensities. Also by means of the detection of primary gamma transitions information about the resonance spins can be obtained.

Since the decay of compound nuclear resonances to the groundstate by gamma radiation is a statistical process for heavy nuclei, it is possible with the help of numerical simulations to calculate the populations of low-lying states assuming that the low-energy level scheme is known well enough. This provides a means to predict the size of the spin effect and to select the gamma-ray transitions that are most sensitive to the resonance spin. Simulations have been carried out for the above mentioned nuclei. The results are in agreement with measured values of ratios of gamma-ray intensities.

The experiments have been performed at the pulsed neutron source GELINA in Geel (Belgium). Use was made of gamma spectroscopy in combination with measurements of neutron time-of-flight. As the *p*-wave resonances in the epithermal energy range are relatively weak, it is necessary to make long-lasting measurements in the order of 1000 hours. The spins of 19 *p*-wave resonances of ^{238}U and of 23 *s*-wave and 21 *p*-wave resonances of ^{113}Cd have been assigned.

The knowledge of the resonance spins is important for a correct interpretation of recent measurements of parity nonconservation in neutron *p*-wave resonances. Determination of the spins of *s*- and *p*-wave resonances has made it possible to make a more accurate estimate of the strength of parity nonconservation in the mentioned nuclei which has given a more precise value of the weak interaction in nuclear matter. Resonance spin assignments are also of importance for possible measurements of time reversal nonconservation in neutron resonances.

Samenvatting

In dit proefschrift worden experimenten beschreven die geleid hebben tot het toekennen van spins aan een groot aantal resonanties in reacties van epithermische neutronen met de kernen ^{238}U en ^{113}Cd. Wanneer een neutron wordt ingevangen in een atoomkern wordt een samengestelde kern gevormd die zich in een hoog aangeslagen toestand bevindt met een energie in de orde van de bindingsenergie van het neutron. Indien de kinetische neutronenergie wordt gevarieerd rond een toestand van de samengestelde kern, dan ziet men in de werkzame doorsnede een piek. Men spreekt dan van een resonantie in de reactie. Afhankelijk van de hoeveelheid baanimpulsmoment ℓ dat het neutron toevoegt aan het systeem worden de resonanties aangeduid met spectroscopische notaties als *s*- en *p*-golven voor $\ell = 0$ respectievelijk 1. Het is de bedoeling van dit proefschrift de spins van de resonanties vast te stellen.

Het blijkt dat de bezetting van bepaalde niveautoestanden door gammastraling van de vervallende samengestelde kern afhankelijk is van de spin van de resonantie. Door nu de relatieve intensiteit van specifieke gammastralen te meten, kan de resonantiespin worden vastgesteld. De spinafhankelijkheid kan nog vergroot worden door de verhouding te bepalen van twee gamma-overgangen die een tegengesteld spineffect hebben. Hierdoor is het ook niet meer nodig de intensiteiten te normaliseren. Ook door middel van de detectie van de primaire gamma-overgangen kan informatie over resonantiespins verkregen worden.

Doordat het verval van samengestelde kern-resonanties naar de grondtoestand door gammastraling een statistisch proces is voor zware kernen, is het mogelijk met behulp van numerieke simulaties de bezetting van laagliggende niveautoestanden te berekenen, aangenomen dat het niveauschema voldoende bekend is. Dit verschaft een middel om de mate van het spineffect te voorspellen en om de meest spingevoelige gamma-overgangen te selecteren. Simulaties zijn uitgevoerd voor de hiervoor genoemde kernen. De resultaten zijn in overeenstemming met gemeten waarden van verhoudingen van gamma-intensiteiten.

De experimenten zijn uitgevoerd bij de gepulseerde neutronenbron GELINA te Geel (België). Hierbij werd gebruik gemaakt van een combinatie van gammaspectroscopie en de meting van de neutronenvluchttijd. Doordat de *p*-golf resonanties in het epithermische energiegebied relatief zwak zijn, is het noodzakelijk om langdurige metingen uit te voeren, in de orde van 1000 uur. Uiteindelijk zijn de spins van 19 *p*-golf resonanties van ^{238}U en van 23 *s*- en 21 *p*-golf resonanties van ^{113}Cd bepaald.

De kennis van resonantiespins is belangrijk voor een juiste interpretatie van recente metingen van de schending van pariteit in neutron *p*-golf resonanties. Bepaling van de spins van de *s*- en *p*-golf resonanties heeft het mogelijk gemaakt een meer precieze schatting te maken van de sterkte van de schending van pariteit in bovengenoemde kernen

hetgeen een nauwkeuriger waarde van de zwakke wisselwerking in kernmaterie heeft gegeven. Ook voor de interpretatie van mogelijke metingen van schending van tijdsomkeerbaarheid invariantie in neutronenresonanties is de bepaling van resonantie-spins van belang.

Introduction

After the discovery in the late 1950s that parity is not conserved in β-decay, which is due to the weak interaction in nuclei, searches were made for parity nonconservation in all kinds of nuclear and atomic processes. Three of the four fundamental forces, the gravitational, electromagnetic and the strong force, are believed to conserve parity whilst the weak interaction does not. The weak interaction has been studied extensively through the past decades in leptonic processes but also the interaction between hadrons possesses a weak component. The ratio of the strength of the weak to that of the strong interaction is about 10^{-7} in the nucleon-nucleon interaction. It was therefore a surprise in 1963 when parity nonconservation (PNC) was discovered in the neutron-nucleus interaction with an effect of 10^3 times larger than expected. Later on, PNC effects were measured in neutron *p*-wave resonances with even an enhancement factor of 10^6.

Although the nucleus seems to be a system completely governed by the strong and the electromagnetic force, it favours under suitable conditions a large enhancement of the weak interaction in the highly excited compound nucleus region, giving rise to the above mentioned parity nonconservation effects in neutron *p*-wave resonances. This phenomenon has been explained by the admixing of nearby *s*-wave resonances and by the large difference of their neutron entrance channel widths. In the epithermal neutron energy range the widths of *p*-wave resonances are typically a factor 10^3 smaller than the widths of *s*-wave resonances. Consequently, PNC effects are particularly prominent in neutron *p*-wave resonances of heavy and medium mass nuclei. Often PNC is measured as the relative difference of the total cross section of longitudinally polarized neutrons with positive and negative helicity through an unpolarized target. This parity nonconserving asymmetry can have values ranging up to several percents, which is quite large compared to the usually obtained asymmetries in the order of 10^{-4} in other PNC measurements.

In the past, hadronic parity nonconservation was usually found in only a single resonance per nucleus until recently PNC has been observed in several neutron resonances of the zero spin target nuclei ^{238}U and ^{232}Th in the very successful TRIPLE experiments at Los Alamos. This made it possible for the first time to estimate the root mean squared parity nonconserving matrix element in nuclear matter. This quantity is a general nuclear property that reveals the overall strength of the weak interaction in the nucleus. After the success for these heavy mass nuclei, a number of nonzero spin nuclei of lower mass have been investigated, among which ^{113}Cd. This is near a maximum in the neutron *p*-wave strength function.

It is supposed that the PNC matrix elements form a random variable with a Gaussian distribution within the ensemble of the p-wave resonances. To extract the width of this distribution from the measured PNC asymmetries, it is important to know which p-wave resonances can be admixed by which s-wave resonances. In a zero spin target nucleus, the s-wave resonances have a spin 1/2 while the p-wave resonances can have spin 1/2 or spin 3/2. Only the spin 1/2 p-wave resonances can show PNC effects while the asymmetry measured for spin 3/2 p-wave resonances should be consistent with zero. Therefore the knowledge of the spins of the resonances is of great importance for a proper analysis of the measured PNC asymmetries and for a check of the TRIPLE experiments. For a target nucleus with spin larger than zero, there are more possible values of the spin for both s- and p-wave resonances and the parity nonconserving mixing is somewhat more involved.

It is believed that the same amplification mechanisms that enhance parity violation in compound nuclei hold also for the possible violation of time reversal invariance. This symmetry violation has not yet been detected directly but until now it has been observed only indirectly in the decay of neutral kaons. The compound nucleus may provide a means for direct observation of the violation of time reversal invariance. Experiments that are able to reveal this asymmetry require a thorough knowledge of especially the neutron resonance parameters and therefore resonance spin assignments are also important in this context.

This thesis describes the experiments at the GELINA pulsed neutron facility in Geel, Belgium, that have lead to the determination of resonance spins in ^{238}U and ^{113}Cd. This was achieved by using the low-level population method, based on the gamma decay of the compound nucleus formed after neutron capture. This method takes advantage of the fact that the intensity of specific low-energy gamma-ray transitions of the decaying compound nucleus resonance depends significantly on its spin. The method has already successfully been applied to assign the spins of s-wave resonances in several nuclei but prior to this work, not for p-waves. In the case of p-wave resonances, of which the strength in the epithermal neutron energy range is smaller than that of s-waves by a factor of 10^3, the application of the method is less apparent. Measurements at the GELINA neutron source need typically 1000 hours for data acquisition in order to collect sufficient statistically significant data for unambiguous spin assignment. In addition to the low-level population method, the observation of the occurrence of high energy primary gamma rays, emitted directly from the capturing state, to specific low-lying levels with known spins and parities has given information about resonance spins.

In chapter 1 the background of the parity nonconservation measurements is discussed, notably PNC in neutron resonances, and the spin determinations for the analysis of PNC data is demonstrated to be necessary in order to extract the PNC strength correctly. Several methods of spin assignment are treated and the low-level population method is dealt with in some more detail. Additionally, some basic notions concerning neutron resonance theory and neutron capture in particular are considered.

In order to cover a large range of neutron energies, the time-of-flight method has been applied at the GELINA pulsed neutron facility. This approach makes it possible to collect gamma-ray spectra, measured with germanium detectors, of many neutron resonances simultaneously using a multiparameter data acquisition system. Chapter 2 describes the experimental techniques concerning the time-of-flight method and gamma-ray spectroscopy in detail. Essential parts of the experimental setup, notably the target-detector arrangement, the radiation shielding and the electronic signal and data flow handling, are also considered in this chapter. In addition, the experimental environment related to neutron measurements at GELINA is portrayed giving the nominal accelerator characteristics and a typical neutron flux.

In chapter 3, Monte Carlo simulations of the statistical gamma decay of the excited compound nuclei ^{239}U and ^{114}Cd, supporting the spin assignment method, are described. Experimental and calculated data are in good agreement, qualitatively for ^{239}U and also quantitatively for ^{114}Cd. Numerical simulations are in this case a useful tool to evaluate the feasibility of a time consuming spin assignment experiment beforehand and their results can be helpful in the analysis of experimental data.

Chapters 4 and 5 of this thesis describe the results obtained from the spin assignment experiments for ^{238}U and ^{113}Cd respectively. The spins of 19 *p*-wave resonances in the spin zero nucleus ^{238}U and of 23 *s*-wave and 21 *p*-wave resonances in the spin 1/2 nucleus ^{113}Cd have been unambiguously assigned. In both cases it was also possible to deduce as a by-product the absolute intensities of several primary gamma-ray transitions in neutron resonances using a normalization to thermal capture gamma rays.

Moreover, an attempt has been made to assign the spins of neutron resonances of ^{232}Th. Because of the high natural activity of the decay chain of thorium, it was not possible to use the low-level population method. It was decided to measure the angular distribution of the high-energy primary gamma rays. However, from this measurement no satisfactory results could be deduced so far. In addition, the few high-energy primary transitions to low-lying levels with suitable spins did not form conclusive evidence for the value of the spins of the ^{232}Th neutron *p*-wave resonances. Therefore the results of this experiment have not been included in this thesis.

Finally in chapter 6 the estimation procedure for the root mean squared (rms) PNC matrix element is elucidated. It is demonstrated that a specific maximum likelihood estimation procedure for this quantity can be derived under some general assumptions. This estimate is based on the PNC asymmetries of those resonances that can show PNC, thus assuming the knowledge of the spins. If the spins of the resonances are not known, it may still be possible to derive an estimate but then several procedures can be applied but the resulting root mean squared PNC matrix element will be less precise. Two of these methods have been used in the case of ^{238}U. The difference between them arises from the treatment of the unknown resonance spins. When the spins are known, both methods converge to each

other. There is a perfect match of the PNC measurements of ^{238}U in Los Alamos and the spin assignments in Geel. The results for the spin assignments of ^{238}U are incorporated in a more accurate estimate for the rms PNC matrix element. In the case of ^{113}Cd the overlap is somewhat less complete. No analysis of PNC effects observed for ^{113}Cd has been given in this thesis since the PNC data were not yet fully analysed by the TRIPLE team.

Chapter 1
Theoretical considerations

1.1. Parity nonconservation

1.1.1 introduction

Symmetry plays an important role in physics. It has been believed for a long time that all physical laws are invariant under the parity operation. The parity operation or space inversion **P** reverses the sign of all the spatial coordinates: $\boldsymbol{r} \rightarrow -\boldsymbol{r}$. If the mirror system gives again a situation that obeys the same physical laws as the original system, then it is said to be invariant under parity. In fact, the gravitational, the electromagnetic and the strong interactions are all believed to be invariant under parity. The principle of parity invariance was thought to be a general symmetry in nature, until Lee and Yang showed in 1956 that for the weak interaction no evidence for parity conservation existed and that there were reasons to believe that parity may not be conserved in the weak nuclear interaction because of the so-called ϑ-τ puzzle [1]. Indeed, Wu and her co-workers found in their famous experiment on the spatial asymmetry of the β^--decay of polarized ^{60}Co nuclei that parity was not conserved in the weak interaction [2]. Many other experiments since then have confirmed the nonconservation of parity in leptonic weak interactions (see also ref. [3]). A recent review considers the theoretical and experimental aspects of parity nonconserving scattering from nucleons and nuclei [4]. Moreover, also a hadronic weak interaction exists in nuclear matter.

There are two more basic symmetry operations, namely charge conjugation **C** and time reversal **T**. The operation **C** consists of replacing each particle by its antiparticle and the operation **T** reverses the time $t \rightarrow -t$ and replaces in quantum mechanics the wave function by its complex conjugate: $\psi \rightarrow \psi^*$. On the basis of very fundamental arguments nature is assumed to be invariant under the combined operations of **P**, **C** and **T**, which is known as the CPT-theorem. A test for CPT-invariance is the equality of the masses and lifetimes of a particle and its antiparticle. So far, no indications for the violation of CPT-invariance have been found [5,6]. The CPT-theorem implies that if one of the operators is violated, at least one of the other operators must also be not conserved. In the case of the weak process of ordinary nuclear β-decay, where parity is not conserved, also charge conjugation is not conserved. In the case of β^+-decay, the asymmetry of β-emission of polarized nuclei is opposite to that of β^--decay as was shown for ^{58}Co and ^{52}Mn [7-9]. The combined operation **CP** preserves here the symmetry.

However, not in all weak processes **CP** is conserved. A small (0.3%) CP-violating part in the decay of neutral kaons has been observed [10,11] and has been confirmed several times and is still subject to investigation [12]. One of these experiments is carried out by the CPLEAR-collaboration [13]. Until now, the kaon decay is the only known process violating **CP**. The consequence of the theorem is that if **CP** is violated, also **T** should be violated. Thus far T-violation has not been observed directly.

Due to the weakness of the parity nonconserving interaction with respect to the strong nuclear parity conserving force, one expects under normal conditions only very small parity admixtures in nuclear levels. The Hamiltonian of the nuclear system is composed of a strong and electromagnetic parity conserving (PC) part and a weak parity nonconserving (PNC) part

$$H_{\text{nucleus}} = H_{\text{strong, PC}} + H_{\text{e.m., PC}} + H_{\text{weak, PNC}}. \tag{1}$$

In several spectroscopy and reaction experiments it was found that parity nonconservation occurs up to about 10^{-3}. Examples in spectroscopy are the 8^- level of ^{180}Hf [14] and the $17/2^+$ level of ^{93}Tc [15,16]. In reactions, parity nonconservation may occur also in compound nucleus formation. It has been shown that parity nonconservation occurs extensively in compound nucleus formation by neutron capture due to specific enhancement factors, notably in epithermal neutron *p*-wave resonances. Since it is believed that the same amplification mechanisms may also hold for the violation of time reversal invariance, a thorough study of parity nonconservation in neutron *p*-wave resonances is, apart from its specific interest for the investigation of the weak interaction, essential for the possible direct observation of the violation of time reversal invariance.

A programme has been started at the GELINA pulsed neutron source facility in Geel (Belgium) for studying neutron *p*-wave resonances that have recently been investigated in parity nonconservation experiments in Los Alamos (USA). The present thesis describes the results of our measurements which strengthen the conclusions of parity nonconserving experiments in epithermal neutron reactions.

1.1.2 parity nonconservation in nuclei

Immediately after parity nonconservation was discovered in β-decay, searches were made for parity nonconserving (PNC) processes in the nucleon-nucleon interaction. Feynman and Gell-Mann [17] predicted that there should be a first order weak, and therefore parity violating, interaction between two nucleons. This nonleptonic parity violating weak interaction between hadrons has a small strength relative to the strong interaction. This small amount is experimentally difficult to observe. The weak hadronic PNC interaction acts as to add to the nuclear wave function a small fraction F of a wave function with opposite parity

$$\psi = \psi^{(\pi)} + F\psi^{(-\pi)} \tag{2}$$

where F is of the order 10^{-7}. Adelberger and Haxton [18] review the field of parity non-conservation in the nucleon-nucleon interaction. Low-energy PNC experiments concerning strongly interacting systems can be divided into the following three classes.

The first type of observations involves processes that would vanish completely if F were zero. These processes are only known in alpha decay. An example is the decay of a 2^- excited state of ^{16}O. The PNC process $^{16}O(2^-) \rightarrow {}^{12}C(0^+) + \alpha$, strictly forbidden if parity were conserved, competes with the normal parity conserving gamma decay to the ground state $^{16}O(2^-) \rightarrow {}^{16}O(0^+) + \gamma$. The selection rules for alpha decay forbid a $2^- \rightarrow 0^+$ transition but when the 2^- state includes a small part of 2^+, the decay is permitted with a small intensity proportional to F^2. Neubeck *et al.* [19] found evidence for this weak branch with intensity of order 10^{-14}. This kind of experiments involving alpha decay have been applied to several light nuclei (see also [18]).

A second class of experiments involves the interference of parity conserving and nonconserving interactions leading to a pseudoscalar (the scalar product of an axial vector and polar vector, for example $\boldsymbol{s} \cdot \boldsymbol{k}$ or $\boldsymbol{I} \cdot \boldsymbol{k}$) in the total cross section, measured in transmission and capture experiments with polarized neutrons. This may also give rise to a $\cos\vartheta$ term in the angular distribution of the reaction products if either the incoming particle or target nucleus are polarized. Without parity mixing only even powers of $\cos\vartheta$ exist, the odd ones vanish. For example Gönnenwein *et al.* [20] have found a parity nonconserving $\cos\vartheta$ dependence in the angular correlation between the incoming neutron spin $\boldsymbol{s}$ and the momenta $\boldsymbol{k}$ of binary and ternary fragments in the fission process following polarized thermal neutron capture.

The third category of experiments concerns the determination of polarization observables in the outgoing channel. Examples are the circular polarization of gamma rays emitted by an unpolarized nucleus, the spin rotation caused by the PNC interaction of the spin of a particle oriented perpendicularly to its motion and the longitudinal analysing power. These experiments need special analysing equipment for the detection of the polarization of the emitted radiation or of the neutron spin rotation.

The work of Abov *et al.* [21] demonstrated for the first time parity nonconservation in the neutron-nucleus system by detecting the asymmetry in the gamma-ray yield from an unpolarized ^{113}Cd sample using polarized thermal neutrons. These experiments have been confirmed several times [22-25]. Alberi *et al.* [26] measured the circular polarization of gamma rays from unpolarized neutron capture in ^{113}Cd. In the experiment of Forte *et al.* [27], a PNC effect was measured in ^{117}Sn by the spin rotation of transversely polarized neutrons. Hereafter, spin rotation was observed in a number of nuclei [28]. Kolomensky *et al.* [29] used the helicity dependence of the total cross section for longitudinally polarized thermal neutrons in ^{117}Sn and in ^{139}La. These experiments pointed out that the PNC effects are associated to the compound nuclear levels. New investigations started looking for parity nonconservation in individual compound nucleus levels in the resonance region.

At the JINR in Dubna Alfimenkov *et al.* [30] performed pioneering experiments and detected PNC asymmetries for p-wave resonances in ^{81}Br, ^{111}Cd, ^{117}Sn and ^{139}La measuring the dependence of the total cross section on the neutron helicity. Very large effects were found, up to several percent, which is about 10^3 times more than in the earlier experiments with thermal neutrons and demonstrating an enhancement of the order 10^5 for the weak component compared to that of the nucleon-nucleon interaction. In these experiments at Dubna parity nonconservation could be observed for at most one resonance per nucleus.

More recently, a breakthrough was obtained by the TRIPLE collaboration in similar experiments at Los Alamos in which parity nonconservation was observed in a considerable number of p-wave neutron resonances of nuclei like ^{238}U, ^{232}Th, ^{113}Cd, ^{107}Ag, ^{109}Ag, ^{113}In and ^{115}In [31]. Parity nonconservation effects in low-energy neutron resonances of heavy nuclei exhibit a large enhancement and have been observed using experiments with polarized neutrons and unpolarized target nuclei.

1.1.3 parity nonconservation observables

The part of the total cross section in neutron transmission experiments that is sensitive to symmetry violation involves three orientations of angular momenta: the spin of the neutron $\boldsymbol{s}$, the spin of the target nucleus $\boldsymbol{I}$, and the direction of the neutron beam, the neutron momentum $\boldsymbol{k}$. Several combinations of these three vectors can reveal one of the asymmetry components P-odd/T-even, P-even/T-odd or P-odd/T-odd in the total cross section. These three components can be observed depending on the type of experiment. Complete expressions for the symmetry violating cross section of the several possible experiments are given by Vanhoy *et al.* [32] and by Gould *et al.* [33]. They contain some basic observables whose properties under the parity and time reversal operation are given in table 1.

Table 1: The effect of the P- and T-operation on several observables.

Observable	P-operation	T-operation
$\boldsymbol{k}$	$-\boldsymbol{k}$	$-\boldsymbol{k}$
$\boldsymbol{I}$	$\boldsymbol{I}$	$-\boldsymbol{I}$
$\boldsymbol{s}$	$\boldsymbol{s}$	$-\boldsymbol{s}$
$\boldsymbol{s}\cdot\boldsymbol{k}$	$-\boldsymbol{s}\cdot\boldsymbol{k}$	$\boldsymbol{s}\cdot\boldsymbol{k}$
$\boldsymbol{I}\cdot\boldsymbol{k}$	$-\boldsymbol{I}\cdot\boldsymbol{k}$	$\boldsymbol{I}\cdot\boldsymbol{k}$
$(\boldsymbol{s}\cdot\boldsymbol{I})\ (\boldsymbol{I}\cdot\boldsymbol{k})$	$-(\boldsymbol{s}\cdot\boldsymbol{I})\ (\boldsymbol{I}\cdot\boldsymbol{k})$	$(\boldsymbol{s}\cdot\boldsymbol{I})\ (\boldsymbol{I}\cdot\boldsymbol{k})$
$\boldsymbol{s}\cdot(\boldsymbol{I}\times\boldsymbol{k})$	$-\boldsymbol{s}\cdot(\boldsymbol{I}\times\boldsymbol{k})$	$-\boldsymbol{s}\cdot(\boldsymbol{I}\times\boldsymbol{k})$
$\boldsymbol{s}\cdot(\boldsymbol{I}\times\boldsymbol{k})\ (\boldsymbol{I}\cdot\boldsymbol{k})$	$\boldsymbol{s}\cdot(\boldsymbol{I}\times\boldsymbol{k})\ (\boldsymbol{I}\cdot\boldsymbol{k})$	$-\boldsymbol{s}\cdot(\boldsymbol{I}\times\boldsymbol{k})\ (\boldsymbol{I}\cdot\boldsymbol{k})$

For parity nonconservation (P-odd/T-even) in the mixing of s- and p-waves the parity violating cross section σ_{PNC} is composed of three terms [33]

$$\sigma_{PNC} = \sigma_{10} + \sigma_{01} + \sigma_{12}. \tag{3}$$

The term σ_{10} corresponds to experiments with a polarized neutron beam and an unpolarized target and depends on the factor $\boldsymbol{s} \cdot \boldsymbol{k}$. The term σ_{01} corresponds to a situation with an unpolarized beam but a polarized target and is related to the factor $\boldsymbol{I} \cdot \boldsymbol{k}$. Finally, the term σ_{12} corresponds to a polarized beam and an aligned target and is dependent on $(\boldsymbol{s} \cdot \boldsymbol{I})\ (\boldsymbol{I} \cdot \boldsymbol{k})$. Until now, experimental results are available only for polarized beam, unpolarized target measurements, thus depending on the $\boldsymbol{s} \cdot \boldsymbol{k}$ factor.

Experiments on time reversal invariance are much more complicated because they involve an odd number of vectors and contain at least one vector product, for example the three-fold correlation $\boldsymbol{s} \cdot (\boldsymbol{I} \times \boldsymbol{k})$ or the five-fold correlation $\boldsymbol{s} \cdot (\boldsymbol{I} \times \boldsymbol{k})\ (\boldsymbol{I} \cdot \boldsymbol{k})$. These experiments require therefore both a polarized beam and an oriented target. Several approaches are possible to study time reversal invariance and various schemes have been developed to circumvent experimental problems, see for example refs. [34-36].

1.1.4 parity nonconservation in neutron *p*-wave resonances

Nuclear states of the same spin but opposite parity can mix and show PNC. In neutron transmission experiments, PNC is expressed as the relative difference of the reaction cross sections for a system and its P-mirror system. In the case of an experiment concerning the transmission of longitudinally polarized neutrons through an unpolarized target, the longitudinal asymmetry P is defined from

$$\sigma^{\pm} = \sigma_p (1 \pm |f_n| P) \tag{4}$$

where $\sigma_p = (\sigma^+ + \sigma^-)/2$ is the unpolarized resonance part of the p-wave cross section and where σ^+ and σ^- are the observed resonance cross sections for a neutron beam having a positive and negative polarization respectively. The neutron polarization f_n is defined as

$$f_n = \frac{\overrightarrow{n} - \overleftarrow{n}}{\overrightarrow{n} + \overleftarrow{n}} \tag{5}$$

with $\overrightarrow{n}$ and $\overleftarrow{n}$ denoting the number of neutrons with positive and negative helicity, i.e. with their spins parallel respectively antiparallel to the neutron direction. With eq. 4 the longitudinal asymmetry can be written as

$$P = \frac{1}{|f_n|} \cdot \frac{\sigma^+ - \sigma^-}{\sigma^+ + \sigma^-} \tag{6}$$

assuming that the degree of neutron polarization f_n has the same absolute value for the two neutron spin polarizations along the beam.

From the experimental data one can fit the cross sections $\sigma^{\pm}$, accounting for the various experimental influences. This is to be preferred compared to deriving P directly from the transmission asymmetry ε with

$$\varepsilon \equiv \frac{C^{+} - C^{-}}{C^{+} + C^{-}} = \tanh\left(-N\sigma_p |f_n| P\right) \cong -N\sigma_p |f_n| P . \tag{7}$$

Here $C^{\pm}$ are the detector counts for the neutron polarizations parallel, respectively antiparallel to the beam and N is the sample thickness in atoms per barn. The approximation of the hyperbolic tangent is allowed if its argument is small.

It can be shown (see for example refs. [30,37]) that an expression for P can be derived on the basis of first order pertubation theory. Considering only the two-level approximation, i.e. the mixing of one p-wave resonance of energy E_p with one s-wave resonance of energy E_s with the same spin and opposite parity, the longitudinal asymmetry P is then given by

$$P = \frac{2V_{sp}}{E_s - E_p}\left(\frac{\Gamma_n^s}{\Gamma_n^p}\right)^{1/2} x_j \tag{8}$$

where $V_{sp} \equiv \langle s|H_{PNC}|p\rangle$ is the matrix element of the weak interaction between the s- and p-wave resonances. Γ_n^s and Γ_n^p are the neutron widths of the s- and the p-wave resonances. The factor x_j, the fraction with total neutron spin $j = 1/2$ at the entrance channel, will be explained in the next section. Penetration factors for entering the nucleus are much larger for s-wave than for p-wave resonances, i.e. $\Gamma_n^s \gg \Gamma_n^p$ in the epithermal resolved resonance region. Of course there is also a mixing of p-waves into s-wave resonances but as the difference in neutron widths is large, this has a negligible effect. The factor $(\Gamma_n^s/\Gamma_n^p)^{1/2}$ is usually called kinematic enhancement.

The ratio $V_{sp}/(E_s - E_p)$ in eq. 8 is usually referred to as dynamic enhancement and has been discussed by several authors [37-40]. In the complicated compound nuclear system this enhancement is a factor $N^{1/2}$ compared to the nucleon-nucleon system, where N is the number of components in the compound nuclear wave function. Together, the dynamic and kinematic enhancement form an amplification of the PNC effect in the compound nucleus compared to the nucleon-nucleon interaction that can be in the order of 10^4–10^6. Indeed, PNC effects have been found in p-wave resonances of several nuclei with effects of percents and in two nuclei as large as 10 percent.

1.1.5 spin coupling and total neutron angular momentum

Like normal discrete bound states, also the neutron resonances have a definite spin and parity J^{π}. The possible values of J^{π} depend on the spin I and parity π_I of the target nucleus and the angular momentum ℓ with which the neutron has been captured. The res-

onance spin is the vector addition of the three angular momenta involved, and the parity is the product of the parities of the neutron, the nucleus and the orbital momentum. The neutron has the intrinsic spin $s = 1/2$ and parity $\pi_n = +1$, the resonance spin and parity are

$$\boldsymbol{J} = \boldsymbol{I} + \boldsymbol{\ell} + \boldsymbol{s} \tag{9}$$

$$\pi = \pi_n \cdot \pi_I \cdot (-1)^{\ell}. \tag{10}$$

Parity nonconservation can occur in p-wave resonances by admixing of an s-wave resonance with the same spin. However, in the recent transmission experiments with polarized beams and unpolarized targets, only the part of the p-wave resonance having at the entrance channel a total neutron angular momentum $\boldsymbol{j} = \boldsymbol{\ell} + \boldsymbol{s}$ equal to 1/2 is contributing [30,41]. The amplitude fraction of the entrance channel with $j = 1/2$ is accounted for in eq. 8 by the factor x_j defined as

$$x_j^2 = \Gamma_n^{p,\, j=1/2} / \Gamma_n^p. \tag{11}$$

In most cases, the spin J of the p-wave resonance is not known and the fraction of the neutron width Γ_n with $j = 1/2$ even less.

However, this is not always a problem. Let us consider the easiest situation, when the target spin I is zero as in the case of the even-even nucleus ^{238}U. In that case there is only one way to combine the involved angular momenta to form an s-wave resonance which must have spin $I = 1/2$. For the p-waves there are two possibilities, as can be seen in table 2, a spin $I = 1/2$ and a spin $I = 3/2$. Because the target spin $I = 0$, the total neutron angular momentum equals the resonance spin: $j = J$. So in this case, parity nonconservation can occur by mixing of the $J = 1/2$ s-wave into the $J = 1/2$ p-wave resonance. The $J = 3/2$ p-wave cannot show a PNC effect. The several possible combinations for this $I = 0$ case are shown in table 2. In addition the channel spin S is defined by $\boldsymbol{S} = \boldsymbol{I} + \boldsymbol{s}$.

Table 2: The possible combinations to form the resonance spin J with the neutron spin $s = 1/2$, the target spin $I = 0$ and the angular momentum together with the intermediate neutron entrance spin j and channel spin S.

s	I	ℓ	j	S	J
1/2	0	0	1/2	1/2	1/2
1/2	0	1	1/2	1/2	1/2
1/2	0	1	3/2	1/2	3/2

The situation is different when we have a target spin $I = 1/2$, as in the case of ^{113}Cd. Now there are two ways to form an s-wave resonance, one having spin $J = 0$ and one having $J = 1$. The p-wave resonances can have spins $J = 0$, 1 or 2. From the different combinations, listed in table 3, one may notice that for the $J = 0$ p-wave resonances the total neu-

tron angular momentum at the entrance channel is $j = 1/2$, therefore these resonances can fully contribute to PNC effects by mixing with $J = 0$ s-wave resonances. Different is the situation for the $J = 1$ p-wave resonances since both $j = 1/2$ and $3/2$ are possible. In this case only the usually unknown amplitude fraction x_j corresponding to $j = 1/2$ contributes to the mixing with s-wave resonances.

Table 3: The possible combinations to form the resonance spin J with the neutron spin $s = 1/2$, the target spin $I = 1/2$ and the angular momentum together with the intermediate neutron entrance spin j and channel spin S.

s	I	ℓ	j	S	J
1/2	1/2	0	1/2	0	0
1/2	1/2	0	1/2	1	1
1/2	1/2	1	1/2	1	0
1/2	1/2	1	1/2	0,1	1
1/2	1/2	1	3/2	0,1	1
1/2	1/2	1	3/2	1	2

1.1.6 information contained in PNC data

Before 1988, experiments on parity nonconservation in neutron resonances have been performed with the observation of PNC effects in at most a single resonance in various nuclei like ^{81}Br [30], ^{111}Cd [30], ^{113}Cd [30], ^{117}Sn [30,44] and ^{139}La [30,44] in which the last case showed the largest effect close to 10%. These PNC effects have recently been confirmed and extended in ^{81}Br [42,43], ^{111}Cd [42], ^{113}Cd [31] and ^{117}Sn [45]. The 0.73 eV resonance of ^{139}La became a calibration standard for PNC experiments [46,47,48]. After 1988, the TRIPLE collaboration, making use of the intense pulsed neutron source LANSCE in Los Alamos, started to study PNC in a large number of resonances in a single nucleus, notably for the zero spin nuclei ^{238}U [49,50] and ^{232}Th [51] but also for nonzero spin nuclei like ^{113}Cd [31] and more recently for ^{107}Ag, ^{109}Ag, ^{113}In and ^{115}In [52]. PNC effects have been found in several resonances per nucleus.

For the analysis of the PNC data, the two-level approximation of eq. 8 must be generalized. The longitudinal analysing power P_i in a p-wave resonance labelled i can be expressed in terms of not only one but several admixing s-waves labelled j as

$$P_i = \sum_j \frac{2V_{ij}}{E_{s,j} - E_{p,i}} \left(\frac{\Gamma_n^{s,j}}{\Gamma_n^{p,i}} \right)^{1/2} \tag{12}$$

which is valid for spin zero nuclei. In this expression V_{ij} is the PNC matrix element between the state i and j, which is considered to have a Gaussian distribution with mean zero and variance M^2. When the spins of the concerned resonances are not known, one ignores which values have to be included in the estimation procedure. Obviously, for a 0^+

target nucleus the resonances that show a large longitudinal asymmetry with a small error, indicating a clear PNC effect, must have a spin 1/2. The contrary is not true however.

Because of the random distribution, there should be many resonances present with a small PNC effect. The measurements are rather complicated and the relative errors, especially for small P_i values, can be considerable. In these cases, it is not clear whether the observed asymmetry is due to a PNC effect in a $J = 1/2$ p-wave resonance, or due to measurement fluctuations around zero asymmetry for a $J = 3/2$ p-wave resonance. Therefore, spin assignment of the resonances is necessary for a correct interpretation of the PNC data and a reliable estimate of the rms PNC matrix element $\sqrt{M^2}$. More about this estimation procedure can be found in chapter 6.

It is expected that M^2 is proportional to the level spacing D and therefore it is convenient to introduce the parity nonconserving spreading width [53]

$$\Gamma^{PNC} = \frac{2\pi M^2}{D} \tag{13}$$

a quantity that is presumably roughly independent of the mass number within the statistical nuclear model. Many considerations about modelling the parity nonconservation effects exist (see e.g. [53-61]). More PNC data of nuclei in other mass ranges are necessary to find a possible mass dependence of M. The concern is to connect the compound nuclear property M to the nucleon-nucleon interaction for a better understanding of the weak interaction in nuclear matter.

On the analogy of the connection between symmetry breaking in the compound nucleus system and in the nucleon-nucleon system for time reversal invariance violation as explained by French *et al.* [62], one can define the parameter α_P which is the ratio of the parity nonconserving strength to the parity conserving strength in the effective nucleon-nucleon interaction. The relation between α_P and the parity nonconserving spreading width Γ^{PNC} is given by

$$\Gamma^{PNC} = 2\pi \times 10^5 \,[\text{eV}] \cdot \alpha_P^2 . \tag{14}$$

The value of the parameter α_P is expected to be in the order of $G_F m_\pi^2 / G_S \sim 10^{-7}$, with G_F the Fermi weak interaction constant, G_S the strong coupling constant and m_π the pion mass. Johnson *et al.* [54] deal in more detail with this matter.

1.2. Spin assignment methods

There are several methods to assign the spins of neutron resonances. Some of them can be applied only in special cases. We briefly discuss several methods and then describe in

more detail those used in the experiments presented in this thesis. Some of the spin assignment methods have been reviewed by Mughabghab [63]. Recently, Postma [41] proposed experiments to determine spins and neutron-channel spin mixing in p-wave resonances in relation to parity nonconservation measurements. We will discuss here several ways to get information about resonance spins from the characteristics of gamma-ray spectra following resonance neutron capture. Also some other spin assignment methods, not based on gamma rays, will be mentioned.

1.2.1 primary gamma rays

A first indicator for the resonance spin are the primary transitions feeding well known levels of the excitation spectrum. Because the observed transitions have usually a dipole character, knowing the final spin I_f limits the resonance spin to be I_f or $I_f \pm 1$. This has been used in the determination of the spins of resonances in ^{238}U and ^{113}Cd, as will be discussed in chapter 4 and chapter 5. To use this method, low-lying states with known spin must be available. Moreover, due to Porter-Thomas fluctuations the intensities of individual primary transitions can largely differ from the average strength expected for a given multipolarity. Another limitation is that such transitions are an indicator for only one specific resonance spin state.

1.2.2 gamma-ray multiplicity

One can also exploit the spin dependence of the average number of gamma decay steps after neutron capture necessary to reach the ground state, the gamma multiplicity. This method has been applied for spin determination by Coceva *et al.* [66] for about 150 s-wave resonances in several $I = 5/2$ and $I = 7/2$ nuclei. Georgiev *et al.* assigned s-wave resonance spins of ^{179}Hf [67]. However, the difference in multiplicity can sometimes be quite small and the related errors can be large for resonances with adjacent spin values. It was found that this method is applicable only to even-even compound nuclei and that the spin effect is much smaller than that of the low-level population method (section 1.2.4). This is partially compensated by the much larger efficiency of the used scintillator detectors instead of germanium detectors.

1.2.3 angular distribution of gamma rays

In s-wave resonances an anisotropic angular distribution of gamma radiation can only occur if the capturing nuclei are aligned or if the capturing nuclei and the neutrons are both polarized [68]. In p-wave resonances the gamma radiation may have an anisotropic angular distribution due to the orbital momentum $\ell \neq 0$, producing a preferred direction of the spins of the compound nucleus. In the case of $\ell \geq 1$ resonances the angular distribution $W(\vartheta)$ of primary gamma-ray transitions can be written as follows

$$W(\vartheta) = \sum_{k=0}^{K} a_{2k} \cdot P_{2k}(\cos\vartheta) \qquad (15)$$

where ϑ is the angle of emission with respect to the neutron beam and where P_{2k} denotes the Legendre polynomial of order $2k$. The maximum order K of the angular distribution coefficients a_{2k} is restricted by the minimum value of the compound state spin J, ℓ and L, where L is the multipolarity of the gamma transition. With p-wave resonances only the second order can occur, that is $a_2 \neq 0$ if $J > 1/2$.

Also secondary gamma-ray transitions may show an angular distribution [41], which for p-wave resonances can be written as

$$W(\vartheta) = 1 + G_2 a_2 P_2(\cos\vartheta) \tag{16}$$

where G_2 is related to the preceding gamma transitions. The nuclear alignment in capture due to the orbital momentum perpendicular to the neutron beam is lost only partially during the gamma-ray cascade. This factor can be estimated by statistical modelling of the gamma cascade [69]. A thorough treatment of angular correlation methods in gamma-ray spectroscopy together with tabulated values related to the coefficients a_{2k} can be found in Ferguson [70].

For $I = 0$ target nuclei, the s-wave resonances ($\ell = 0$), have an isotropic gamma-ray distribution. This is also the case for the $J = 1/2$ p-wave resonances, in contrast to the $J = 3/2$ p-wave resonances. So if anisotropy is found in the angular distribution of primary gamma-rays from a p-wave resonance, this indicates a state $J = 3/2$. In this specific case the angular distribution is proportional to the angle ϑ as follows

$$W_{1/2 \to J}(\vartheta) = 1 \tag{17}$$

$$W_{3/2 \to 1/2}(\vartheta) = \frac{1}{16\pi}(2 + 3\sin^2\vartheta) \tag{18}$$

$$W_{3/2 \to 3/2}(\vartheta) = \frac{1}{20\pi}(7 - 3\sin^2\vartheta) \tag{19}$$

$$W_{3/2 \to 5/2}(\vartheta) = \frac{3}{80\pi}(6 + \sin^2\vartheta)\,. \tag{20}$$

The largest difference in radiation intensity is found for the angles at $\vartheta = 0°$ and $\vartheta = 90°$. In general it is not a problem to detect gamma radiation at $90°$, but the angle at $0°$ implies that a gamma-ray detector has to be placed in the neutron beam, which is experimentally not feasible. Therefore, an optimum angle should be chosen considering the reduced anisotropy for $\vartheta > 0°$ and the counting efficiency. The largest effect can be found in transitions from a $J = 3/2$ to a $J = 1/2$ state given by eq. 18. In figure 1 the ratio $W_{3/2 \to 1/2}(\vartheta_1)/W_{3/2 \to 1/2}(\vartheta_2)$ of the effect is shown as a function of the two angles ϑ_1 and ϑ_2 for both detectors. One can detect single gamma-ray transitions (with germanium detectors) for which the distribution is exactly known, or an average over several primary

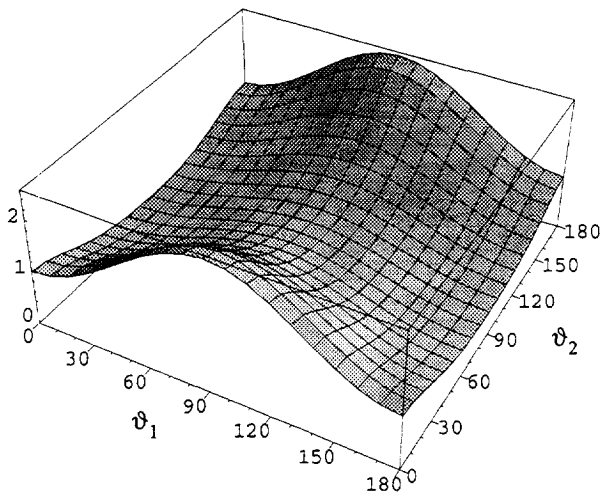

Figure 1: The ratio of the gamma-ray intensities of a transition from a $J = 3/2$ to a $J = 1/2$ state observed at two angles ϑ_1 and ϑ_2.

gamma-ray transitions (with scintillator detectors) which shows a gross distribution effect. We have applied this method to the case of ^{232}Th in a preliminary experiment, of which the limited results will not be discussed in this thesis.

1.2.4 population of low-lying states

The compound nucleus decays after neutron capture to its groundstate by emitting one or several gamma rays in cascade. For nuclei of medium and heavy weight there are many possible ways for cascading gamma rays to the groundstate since the level density is high. For this reason, the decay of the nucleus can be treated within the statistical model. During the decay, the nucleus passes through several intermediate states and the gamma-ray cascade is different when the resonance spin is different. Therefore, the population of nuclear states close to the ground state, may depend significantly on the spin of the capture state. In the past years the method has been applied to a number of nuclei to determine the resonance spins of *s*-waves [71-75]. The extension to the case of *p*-wave resonances is straightforward though experimentally much more difficult because of the very weak strength of most *p*-wave compared to *s*-wave resonances at epithermal neutron energies.

The method can be illustrated with a simple example. We consider the decay of a capture state with spin and take into account only gamma rays with or multipolarity, so that each step has a spin change $= -1$, 0 or +1. In fact, the statistical gamma decay after neutron capture has mainly a dipole character [76]. From figure 2, showing the several possible cascades with three steps, it is clear that the number of ways to reach states with spin or is much smaller than for states where the difference in spin between the capture state and the final state is smaller. The cascade in figure 2 can be mod-

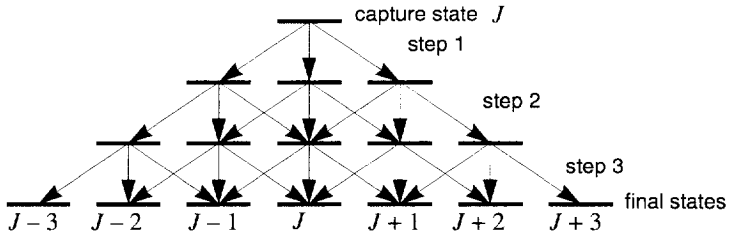

Figure 2: The number of possible spin changes and states reached from the initial capture state after three steps.

elled by using only the spin information to obtain a first idea of the difference in population of final levels. For each step the branching ratio $B_{J \to J_{\text{next}}}$ to a state with given spin J_{next}, being one of the spins $J-1$, J or $J+1$, is taken proportional to their density and is expressed as

$$B_{J \to J_{\text{next}}} = \frac{f(J_{\text{next}})}{f(J-1) + f(J) + f(J+1)} \tag{21}$$

where $f(J)$ is the spin dependent part of the level density function, given by eq. 62 on page 52 which is for low spin values about $f(J) \approx (2J+1)$. A simple straightforward calculation gives the population of spin states after a certain number of steps. In figure 3 the population of final spin states is shown for the decay in four steps of two resonance states having a spin $J_i = 1$ and $J_i = 2$. Of course, this way of proceeding is only a very crude approximation but it illustrates clearly the possibility of different populations starting from different capture spins. More realistic and detailed calculations, involving the simulated decay of a specific excited nucleus, are described in chapter 3.

We see that the difference in population for the different initial spin states is large and that the effect increases with the difference between the initial and final state spin $|J_i - J_f|$. For a small value of $|J_i - J_f|$, the final population is large. Obviously, one has to select to select levels with spins J_f differing from the initial spin J_i, but the difference should not be too large because of the population intensity. The spin effect can be increased by calculating the ratio of the populations of two final states with a spin respectively larger and smaller than the initial spins.

An additional advantage of this ratio is that it does not need any normalization to the total capture rate. The value of the ratio is only dependent on the resonance spin and should, for a set of resonances, split up in different groups for the various possible resonance spins. In an experiment, the populations of the levels are measured by investigating the intensities of the gamma rays deexciting them.

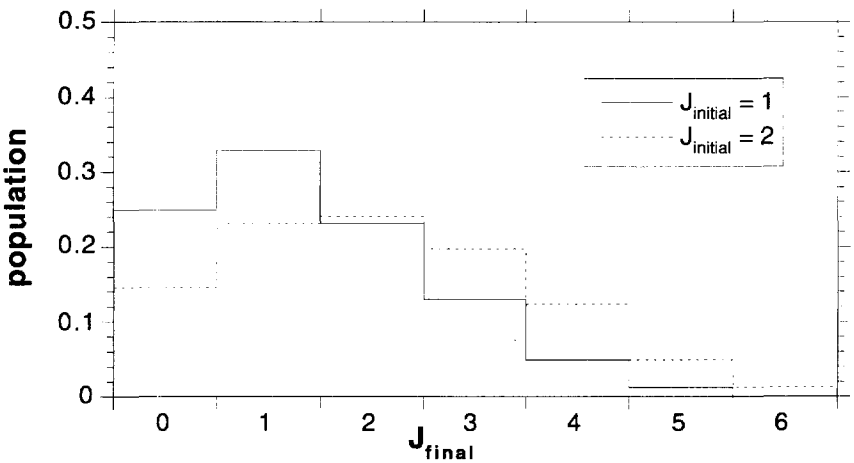

Figure 3: The population of final spin states after the decay of a spin 1 and a spin 2 state in four steps, using branching ratios based on the spin level density.

1.2.5 other spin determination methods

polarization measurements

The cross section of the transmission of polarized neutrons through a polarized target is dependent on the fact whether the spins are parallel or antiparallel with respect to each other. From the difference in the cross section, the spin of the resonances can be determined. Of course, this method cannot be applied to nuclei with spin $I = 0$. This method has been successfully applied for s-wave resonances in, for example, the case of ^{235}U [64,65]. It has been demonstrated that this should work also in the case of p-waves and that both the spin and the channel spin mixing can be determined [41]. For the application of parity nonconservation measurements this is an attractive method. Unfortunately, this type of experiments is technically very difficult to achieve because of the complicated cryogenic setup. Also the nuclear moments of the targets should be fairly large to achieve a sufficient degree of nuclear polarization.

determination of the spin statistical factor

In the mass range $A < 60$ where the s-wave resonance width is dominated by the neutron width, $\Gamma_n \gg \Gamma_\gamma$, the peak cross section at the resonance energy is directly proportional to the statistical factor g. This can be used to determine the spins of resonances of light nuclei. For heavy nuclei, the neutron width becomes smaller than the radiation width and this method cannot be applied. One could then determine $g\Gamma_n$ and Γ from a transmission experiment and $g\Gamma_n^2/\Gamma$ from a scattering measurement. In that case g, and therefore the resonance spin, can be derived by combining these results. This works well for s-wave

resonances with small I, but low-energy p-wave resonances in the heavy mass region have such small neutron widths, that it becomes practically impossible to derive spins in this way.

angular distribution of scattered neutrons

For $\ell \geq 1$ resonances one could observe the angular distribution of elastically scattered neutrons and determine the spins from the distribution parameters [41]. However, this is also very difficult for p-wave resonances for intensity reasons.

1.3. The radiative neutron capture process

1.3.1 the reaction mechanism

As the neutron is not, unlike the proton, affected by the Coulomb barrier, it can penetrate the nucleus with low kinetic energies and initiate nuclear reactions. In a first stage of the reaction, the system of the incident neutron and the target nucleus with mass number A may form a so-called compound nucleus with mass $A + 1$. Due to the separation energy of the neutron, ranging roughly from 4 to 9 MeV, this compound nucleus is in a highly excited state and has several modes of decay, or channels, available to it. In general at low neutron energies for non-fissile nuclei, two decay modes are energetically allowed. First there is the re-emission of the incident neutron. This is elastic scattering if the nucleus returns to its ground state, while the scattering is inelastic when the nucleus returns to an excited state. The second possibility is that the compound system decays through one or several gamma-ray cascades to its ground state. The latter process is called radiative neutron capture and the reaction can be written as

$$n + {}^{A}_{Z}\mathrm{X} \rightarrow {}^{A+1}_{Z}\mathrm{X}^{*} \rightarrow {}^{A+1}_{Z}\mathrm{X} + \gamma\,(+\gamma + \ldots)\,. \tag{22}$$

Although the compound system has an energy above the neutron threshold, and since therefore no bound states exist, there are quasibound states with a relatively long lifetime, called resonances. These are the discrete levels in the compound nucleus region. The structure of resonances is characteristic for a many-body system and corresponds to a very complicated wave function. In figure 4 the schematic process of neutron capture is shown. From the compound nucleus, the neutron may be re-emitted without passing energy to the target, which is indicated in the figure as the elastic scattering channels. If the energy in the center-of-mass system exceeds the energy of the first excited state in the target nucleus, also inelastic scattering becomes possible. In reality, the level density at the neutron threshold, the statistical region, may be about a factor of 10^5 larger than the level density near the groundstate. The relative level distribution in the figure does not correspond with a realistic situation. The cross section in the region of the capturing state is also shown in figure 4 starting in the thermal region at the neutron threshold.

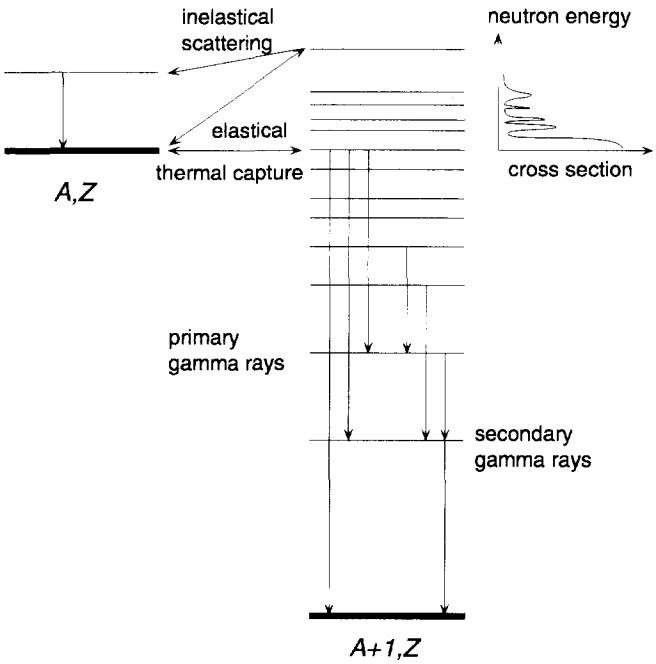

Figure 4: Schematic view of the neutron capture process and the scattering channels.

The high energy gamma rays following immediately the capturing state are called primary gamma rays, while the gamma rays of the further decay are called secondary. In medium and heavy weight nuclei there are usually many primary gamma transitions due to the many available levels.

The neutron incident to the nucleus is described by a plane wave which can be decomposed into a sum of spherical waves, the partial wave expansion, where the sum is running over the orbital momentum ℓ. The neutron of momentum $p = \hbar/\lambda\!\!\!^{-}$ is related to an impact parameter b such that $\ell\hbar = pb$. Here the momentum of the neutron is expressed in the reduced de Broglie wavelength $\lambda\!\!\!^{-} = \lambda/2\pi$. Because the orbital momentum is quantized, the plane of interaction can be divided into zones with a large interaction probability for a specific orbital momentum. The area of a zone (cross section) for a value of ℓ equals $\pi((\ell+1)\lambda\!\!\!^{-})^2 - \pi(\ell\lambda\!\!\!^{-})^2 = (2\ell+1)\pi\lambda\!\!\!^{-2}$. This is the maximum possible cross section if $\lambda\!\!\!^{-} \gg R$, the radius of the nucleus. This is the case for slow neutrons.

We can now derive the cross section for potential scattering, the process where the incident neutron scatters from the potential of the whole nucleus without forming a compound nucleus. The maximum impact parameter is about the sum of the radii of the target

nucleus and the incident neutron, so the maximum ℓ is about $R/\lambda\!\!\!^{-}$. The potential scattering cross section is then

$$\sigma_{pot} = \sum_{\ell}^{R/\lambda\!\!\!^{-}} (2\ell + 1)\,\pi\lambda\!\!\!^{-2} \equiv \pi\,(R + \lambda\!\!\!^{-})^{2}. \tag{23}$$

In the case of resonant neutron capture, this approach is not sufficient. The energy dependence of the capture cross section of a resonance at energy E_R with width Γ has the general Breit-Wigner form for a decaying quantum mechanical state with lifetime $\tau = \hbar/\Gamma$ and can be expressed as [63]

$$\sigma_{\gamma}(E) = \pi\lambda\!\!\!^{-2}\left(\frac{E_R}{E}\right)^{1/2} \frac{g\Gamma_n\Gamma_{\gamma}}{(E - E_R)^2 + \Gamma^2/4}. \tag{24}$$

The total width Γ is the sum of all the partial widths corresponding to the entrance and exit channels. For radiative neutron capture, these channels are the neutron channel corresponding to Γ_n and the gamma decay channel corresponding to Γ_{γ}. The contribution of the different angular momenta channels, dependent on the neutron spin s, the target spin I and ℓ, coupled to form the compound spin J, is taken into account by the statistical factor g, defined as

$$g = \frac{2J + 1}{(2s + 1)\,(2I + 1)}. \tag{25}$$

In particular nuclei the neutron might be captured directly into a specific shell configuration without perturbing the core, which is called valence capture. It is also possible that the

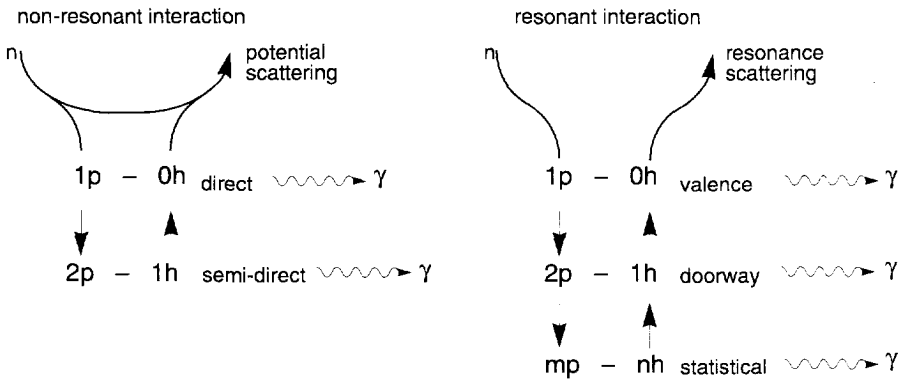

Figure 5: Schematic view of the several resonant and non-resonant neutron scattering and capture mechanisms, after ref. [77].

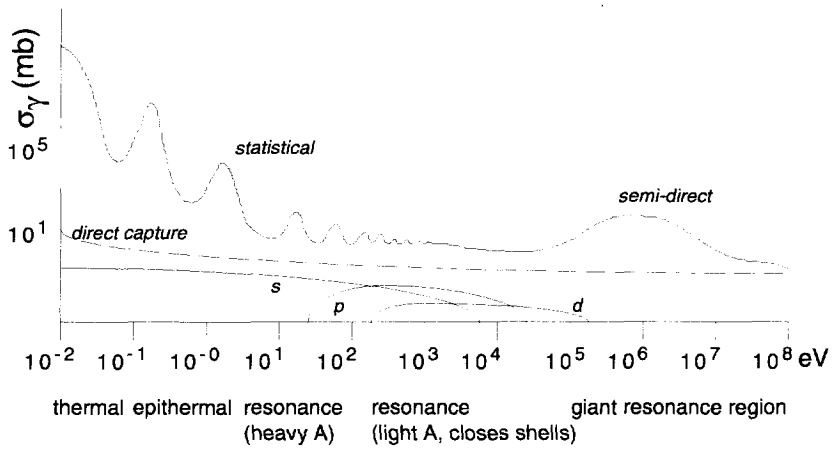

Figure 6: Various neutron capture processes over ten decades of energy, after ref. [77]. Statistical capture relative to direct capture is shown in the upper curves together with the relative strengths of *s*-, *p*- and *d*-wave capture.

directly captured neutron gives rise to a doorway state, a somewhat more complicated particle-hole configuration. These two processes are called channel capture.

At neutron energies higher than about 5 MeV, non-resonant interactions become dominant. In direct capture, the neutron undergoes a single particle transition to a low-lying excited state. In semi-direct capture, the giant dipole resonance, a collective vibrational motion of all neutrons and protons, of the compound nucleus is excited.

In figure 5 the several capture processes are represented and divided into resonant and non-resonant contributions. Also potential scattering is shown as an incoming neutron that is deflected from the potential well of the nucleus without exchanging energy. The statistical decay, which is important in this context, can in fact be considered as a complex excitation of a many-particle many-hole state (mp-nh). All the capture processes, if not followed by elastic scattering of the neutron, decay by gamma-ray emission.

A view of the different capture mechanisms for a broad neutron energy range is given in figure 6. The main curve shows the total cross section in the statistical region and at higher energies a collective semi-direct capture mechanism in the giant resonance region is visible. The resolved resonance region for heavy mass nuclei with unpaired neutrons is generally in the eV neutron energy range, while for lighter nuclei and nuclei with closed or nearly closed shells the resonances start only in the keV region. The dashed curve in figure 6 shows the direct capture as a slowly decreasing cross section which is not important at lower energies. The vertical scale gives an indication of the expected values of the

cross section. Also in figure 6 the relative strengths of *s*-, *p*- and *d*-wave capture are represented. Due to the orbital momentum barrier, the larger ℓ-values become important only at higher energies.

1.3.2 statistical behaviour

According to the Bohr assumption the decay of the compound nucleus is independent of the way it has been formed. The essential idea of the compound nucleus is that the energy of the incident particle is shared amongst the nucleons in a time which is short compared to the lifetime of the compound state. In this way the decay depends only on the energy, spin and parity of the compound state. The compound nucleus is a highly excited system with a large number of degrees of freedom. The wave function is extremely complex and may contain 10^4-10^6 components in heavy nuclei [78]. The density of levels in this region is consequently very high, a factor of 10^5 higher than the region just above the ground state. Due to extreme configuration mixing, the nuclear system at the neutron threshold has a statistical behaviour. This is expressed by the fact that the matrix elements relating two nuclear states have a random character, governed by a Gaussian distribution with zero mean.

Porter-Thomas and Wigner distributions

The observed distribution of the resonance neutron decay width has been explained by Porter and Thomas [79]. The reduced amplitudes of the several channels have a Gaussian distribution in the statistical model. The neutron width, being the square of the amplitude has therefore the so-called Porter-Thomas distribution

$$P(x) = \frac{1}{\sqrt{2\pi x}} \exp(-\frac{x}{2}) \tag{26}$$

with the parameter x representing the neutron width divided by the average neutron width $x = \Gamma_n / \langle \Gamma_n \rangle$. This distribution is valid for the widths of any compound reaction with a single exit channel, i.e. for the neutron widths Γ_n as well as for the partial radiative widths $\Gamma_{\gamma if}$ from an initial state i to a final state f in which case we have $x = \Gamma_{\gamma if} / \langle \Gamma_{\gamma if} \rangle$. The Porter-Thomas distribution is a special case of the chi-square distribution

$$P(\chi^2, \nu) = \frac{1}{2^{\nu/2}\Gamma(\nu/2)} (\chi^2)^{\nu/2-1} \exp(-\frac{\chi^2}{2}) \tag{27}$$

with one degree of freedom $\nu = 1$. In this expression Γ represents the gamma function.

Because of the Porter-Thomas fluctuations to which all statistical gamma rays are subject, the high-energy primary gamma-ray spectrum in radiative neutron capture varies from resonance to resonance. Fits of measurements of partial gamma widths to the chi-square distribution have sometimes led to values of ν differing from one, but this is generally ascribed to a lack of sufficient resonance data or to nonstatistical effects.

The distribution of the spacing D of compound levels of the same spin and parity has been explained by Wigner, who treated the problem using random matrices and derived the so-called Wigner frequency function of level spacings

$$P(D) = \frac{\pi}{2}\frac{D}{\langle D\rangle^2}\exp(-\pi\left(\frac{D}{2\langle D\rangle}\right)^2). \tag{28}$$

The Wigner distribution describes the observed effect of level repulsion, the fact that small spacings are unlikely to occur. Of course, also large spacings have a small probability.

neutron strength functions

For the systematic study of the neutron reactions, the reduced neutron width has been introduced as a quantity from which the energy and ℓ-dependence have been removed. The reduced width Γ_n^ℓ is defined as

$$\Gamma_n^\ell = \sqrt{\frac{1\text{ eV}}{E_R}}\cdot\frac{\Gamma_n}{V_\ell} \tag{29}$$

where the penetrability V_ℓ accounts for the angular momentum barrier. Factors V_ℓ have been derived for a square well potential. These quantities are for s- and p-waves resonances:

$$\begin{aligned} V_0 &= 1 \\ V_1 &= k^2R^2/(1+k^2R^2) \end{aligned} \tag{30}$$

where $k = 1/\lambda\!\!\!^{-}$ is the neutron wave number, and R the interaction radius, usually taken as $R = 1.35A^{1/3}$ fm.

In the extreme application of the statistical model, the neutron strength function is constant for all nuclei. The neutron strength function S_ℓ is a dimensionless quantity related to the reduced average neutron width and is defined for a partial wave with orbital momentum ℓ as:

$$S_\ell = \frac{\langle g\Gamma_n^\ell\rangle}{(2\ell+1)\,D_\ell} \tag{31}$$

where D_ℓ is the average level spacing of resonances with orbital momentum ℓ. Although the statistical model provides a good description for a given nucleus, the overall behaviour of the strength function is not constant with mass A. Nuclear shell structure effects become apparent in the overall view of the strength function as a function of A. Calculations within the optical model do agree well with the experimental data [80].

1.3.3 Doppler broadening

The natural shape of a resonance does not correspond with the cross section that is observed in an experiment. Apart from the various experimental influences on the measurements of cross sections, introduced among others by the specific way of production of the neutrons (see e.g. [81]) and detector resolution, one more basic component is added to the width. The thermal motion of the atoms in the target bulk matter at an effective temperature T, gives rise to a Doppler broadening. The Lorentzian or Breit-Wigner form of the resonance is supplementarily broadened with a Gaussian distribution having a width Δ_D. For a resonance at energy E_R this width is given by:

$$\Delta_D = \sqrt{\frac{4k_B T}{A}} \cdot \sqrt{E_R} \tag{32}$$

where k_B is the Boltzmann constant and A the mass number of the target nucleus [82,83]. To arrive at this expression the nuclear motion in the bulk matter is represented by the Maxwell distribution of motion in a gas. The Doppler broadening is often more important than the natural width of a resonance but in many cases it is largely overshadowed by the experimental loss of resolution. For high precision cross section measurements it can therefore be advantageous to cool the target sample.

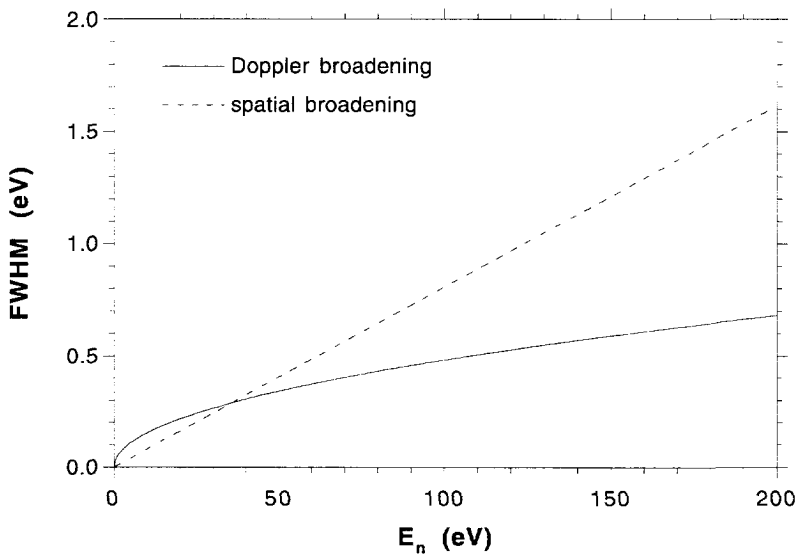

Figure 7: The energy uncertainties that can be expected for ^{238}U resonances at the 12.85 m flight path with the sample under an angle of 30°. At lower energies the Doppler broadening becomes important.

In figure 7 the contributions of the spatial width as explained in section 2.2. on page 33 and the Doppler broadening are shown for the case of the measurement of ^{238}U at the 12.85 m flight path with the sample under an angle of 30°. The observed width at a certain energy is the convolution of these components with the natural width. At low energies the Doppler broadening forms a large contribution while at higher energies the experimental broadening becomes more important.

Chapter 2
Experimental techniques

2.1. Pulsed neutron sources

2.1.1 introduction

For high-resolution neutron spectroscopy and for measurements of nuclear reactions involving neutrons of various energies, a neutron source covering a large energy range must be available. Accelerator-based pulsed white neutron sources are for this purpose very suitable. If a moderator is used, such machines can provide a neutron energy spectrum ranging from thermal energies (25 meV) up to several tens or hundreds of MeV. It is necessary that the source is pulsed because the selection of the neutron energy is determined by the time-of-flight (TOF) method. Such pulsed neutron sources are realized using electron- and proton-based accelerators.

The proton-based machines produce neutrons as secondary particles in reactions in the MeV region up to about 100 MeV. At higher energies the spallation process becomes important with a very high yield of neutrons per proton striking a target of heavy nuclei. The electron-based sources produce neutrons via Bremsstrahlung. The cross section for this process is approximately proportional to Z^2, thus advantageous for heavy mass nuclei. The photons induce photonuclear reactions (γ,n) and, if the target is fissionable, photofission reactions (γ,f). Around about 10-20 MeV the cross section for photodisintegration reactions increases considerably due to the giant resonance and is approximately proportional to NZ/A, thus again favouring targets of heavy mass nuclei. The neutron yield is for electrons above 30 MeV nearly proportional to the electron energy. The energy distribution of the source neutrons constitute an evaporation spectrum, centred around several MeV. A moderator of a material rich in hydrogen is usually applied in order to obtain low-energy neutrons.

A review covering the topic of neutron sources can be found in refs. [84,85]. We will discuss here the neutron source GELINA, based on the linear electron accelerator located in Geel, Belgium. Apart from GELINA, several other pulsed neutron sources are presently in operation and used for nuclear physics experiments. Other important pulsed-neutron facilities are given in the following list.

- the LANSCE facility at Los Alamos, based on LAMPF, a 800 MeV proton linear accelerator with storage ring,
- the ORELA facility at Oak Ridge, based on a 178 MeV L-band electron linac,
- the electron linac at RPI, Troy (USA),
- the spallation source at the synchrocyclotron at KEK, Tokyo,
- the IBR-30 in Dubna, consisting of a 32 MeV electron linac, coupled with a U-Pu booster.
- the 46 MeV electron linac at KURRI, Kyoto.

2.1.2 GELINA pulsed neutron source

The Geel Linear Accelerator pulsed neutron facility is based on an S-band linear electron accelerator built in 1965 and successively upgraded in 1976, 1984 and 1994. It produces an electron beam with a maximum energy of 140 MeV. The maximum beam power is 12 kW at an average energy of about 100 MeV. A detailed description of the machine can be found in refs. [86,87].

The pulse duration of the electron beam can be optionally reduced to less than one nanosecond due to the unique compressing magnet system [88]. The 10 ns pulse of the linac consists after acceleration of a series of 30 microbunches spaced 0.33 ns, each bunch having a sequentially decreasing average energy ranging from 140 to 70 MeV. The microbunches pass through a 360° bending magnet of special design, so that electrons with higher energies have a longer trajectory than the less energetic ones, in this way reducing the space between the microbunches and compressing the total pulse into about 1 ns, as illustrated in figure 8. The outer trajectory through the bending magnet corresponds to the track of the electrons with 140 MeV while the smallest circular path corresponds to the 70 MeV electrons.

The electron beam hits a rotating uranium target, cooled by a flow of mercury. The induced Bremsstrahlung produces neutrons by (γ,n) and (γ,f) reactions. The energy

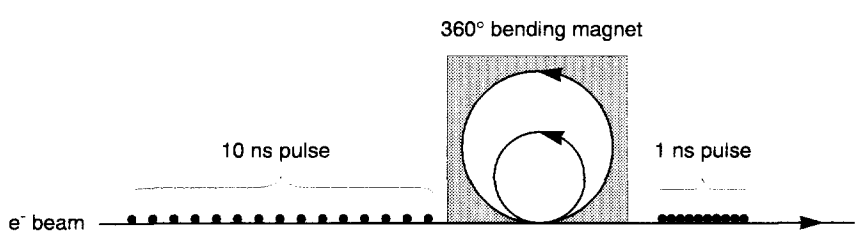

Figure 8: The principle of the compression magnet. The 30 microbunches of the 10 ns pulse are tightened up in time by means of the 360° compression magnet, after ref. [88].

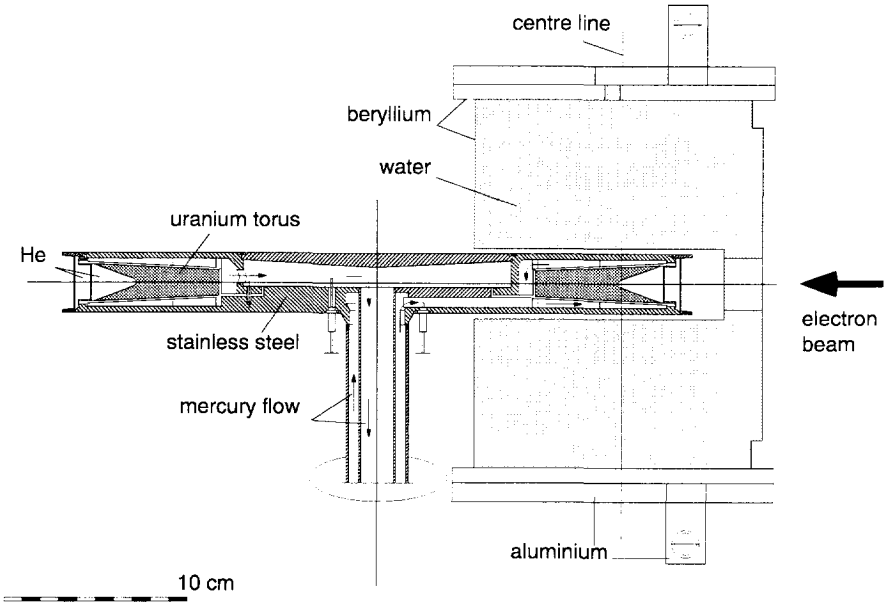

Figure 9: Cross view of the mercury cooled rotating uranium target with the water moderator. The neutron flight paths are positioned perpendicular to the centre line.

distribution of the neutrons emitted by this target is peaked at 1-2 MeV with a small intensity of low-energy neutrons.

In order to have a significant number of neutrons in the energy range below 100 keV, a moderator consisting of material with a very high proportion of hydrogen atoms has to be used. Under and above the target, two slabs of 4 cm thick water canned in beryllium are placed. Neutrons emitted from the target loose their kinetic energy by scattering at the hydrogen nuclei. The partially moderated neutrons have an approximate $1/E$ energy dependence plus a Maxwellian peak at thermal energy (see also figure 12 on page 33).

In figure 9 a cross view of the rotating uranium target with the water moderator is shown. A large number of flight paths are oriented to the neutron centre line and the ones at 90° with respect to the electron beam view the smallest amount of moderator material. The scattered neutrons are collimated into the flight paths leading to the experimental areas. Each flight path can be individually shielded against gamma rays and neutrons coming directly from the production target with a lead plus copper shadow bar of 30 cm total thickness, screening the target and placed at about 1 m from it.

In the case of very short electron bursts (1 ns wide), the moderation process provides the largest contribution to the resolution of the time-of-flight spectrometer. This is due to the fact that one ignores the position of the last scattering of a given slow neutron inside the moderator. The contribution to the timing uncertainty is expressed in the form of an average moderation distance $\langle d \rangle = vt$ that a neutron with velocity v will travel through the moderator in a time t. This uncertainty should not exceed the thickness of the water slab, in this case 4 cm, or the corresponding thickness when the moderator is seen under an angle. The average moderation distance $\langle d \rangle$ is a function of the neutron energy and is a specific parameter for each flight path in several energy ranges for different types of moderators. These parameters are documented and regularly experimentally verified [89]. The final characteristics of the neutron beams are accounted for by the resolution function, relating the observed neutron flight time to the spread in neutron energy. Extensive modelling with numerical simulations have been performed to obtain resolution functions [90].

The undermoderated neutron flux as coming from the moderator has in the thermal energy region an approximate Maxwellian distribution related to the temperature of the moderator. For measurements at thermal and subthermal energies the water moderator can be replaced by a cryogenic moderator of liquid methane cooled with liquid nitrogen in order to increase the subthermal neutron flux.

In figure 10 an overview of the target hall is given. It shows the path of the accelerated electron beam going through a 12 m long beam line, provided with quadrupole magnets and steering coils. In view of future experiments, the electron beam may continue into the 0° direction (through beam pipe number 9), with removal of the uranium target, for the need of radiation physics experiments, concerning especially optical transition [91] and Smith-Purcell radiation [92]. For neutron experiments, the electron beam passes through the compression magnet and strikes the neutron producing target. A 3.5 m thick concrete wall provides a biological shielding. The flight path identification number is also given in the figure. In fact, not all the beamlines are in use (see also figure 11).

After scattering through the moderators the neutrons enter the flight paths, which are evacuated aluminium pipes of 50 cm diameter with collimators consisting either of borated wax or of copper, placed at appropriate distances in order to confine the beam inside the pipe. The lengths of the flight paths range up to 400 m. At specific points each flight path passes through a station where experiments can be installed. The long flight paths can provide an extremely high energy resolution but of course the neutron flux at large distances is rather low.

In figure 11 the neutron flight paths in use are shown together with the linac building containing the target hall as sketched in figure 10. The angles of the several neutron beam lines differ mutually by 9° or 18° and are oriented around the 90° line with respect to the electron beam of the accelerator.

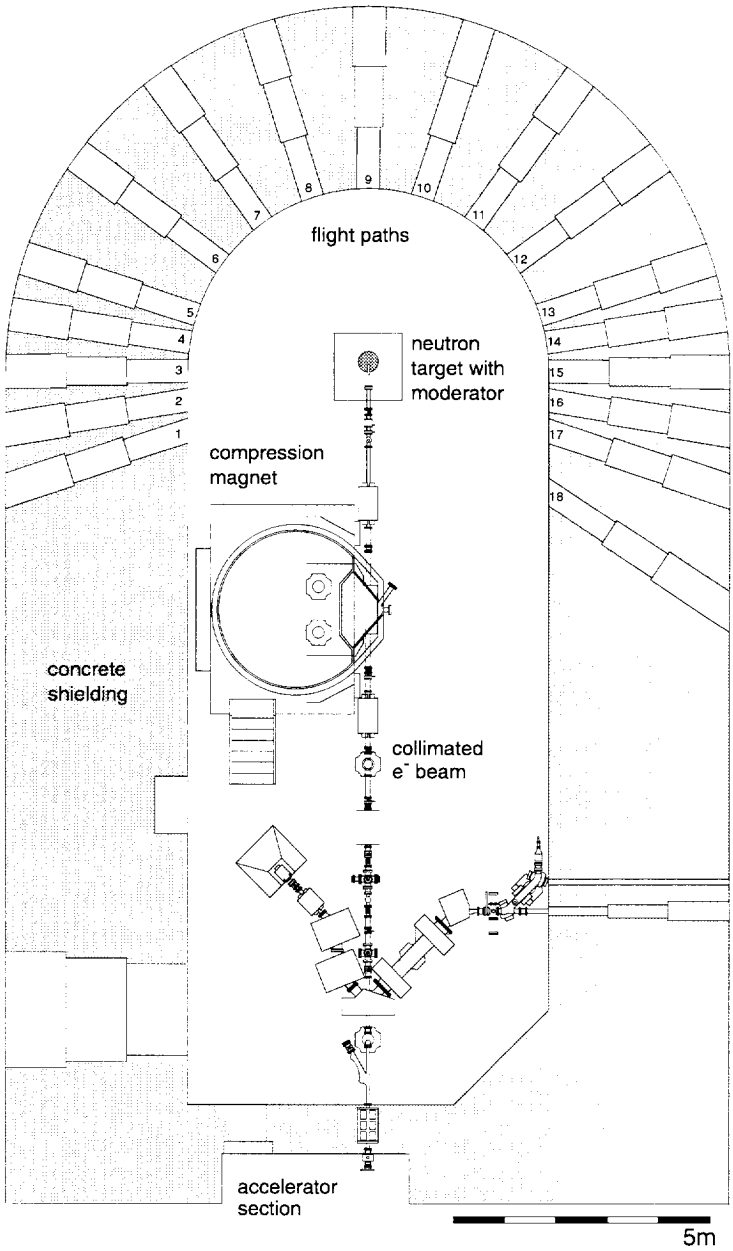

Figure 10: The linac target hall of the GELINA pulsed neutron facility.

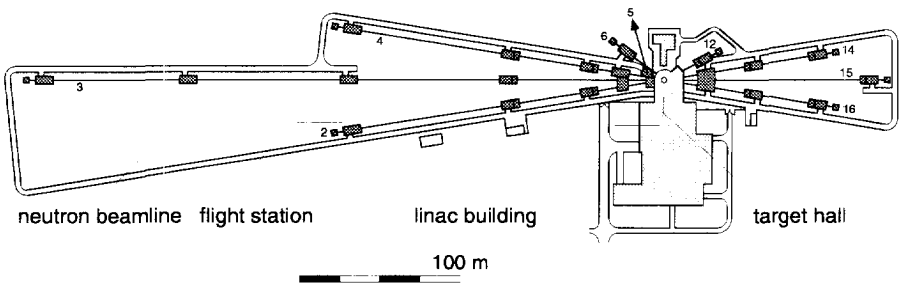

Figure 11: An overview of the neutron flight paths and stations located around the linac building.

Linac parameters and neutron flux

The linac can be operated with various parameters set according to the request of the users. Some of the most common operation parameters for neutron production are summarized in table 4. Although the maximum neutron flux produced in the compressed mode is about 70% of the uncompressed mode, a great improvement is obtained in time resolution. Therefore, for neutron physics experiments nowadays the machine is nearly always operated using the electron pulse compression. The GELINA neutron facility is one of the best pulsed white neutron sources available in the world for neutron spectroscopy measurements due to the combination of long flight paths, short neutron pulse duration and flexible operation of the linac machine.

Table 4: Nominal operation parameters of GELINA

pulse length (ns)	frequency (Hz)	peak current (A)	mean current (μA)	mean power (kW)	neutron burst (n/s)	av. neutron rate (n/s)
			without pulse compression			
5	800	12	48	5.3	$6.4\ 10^{18}$	$2.50\ 10^{13}$
10	800	12	96	9.6	$5.6\ 10^{18}$	$4.40\ 10^{13}$
10	200	12	24	2.4	$5.6\ 10^{18}$	$1.10\ 10^{13}$
10	100	12	12	1.2	$5.6\ 10^{18}$	$0.55\ 10^{13}$
2000	50	0.22	22	2.2	$0.1\ 10^{18}$	$1.00\ 10^{13}$
			with pulse compression			
0.6	800	>100	75	7.5	$4.6\ 10^{19}$	$3.40\ 10^{13}$

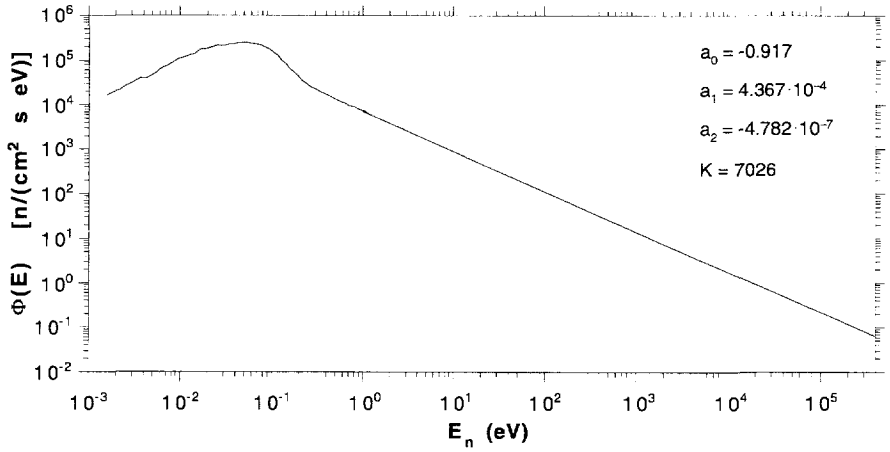

Figure 12: The absolute neutron flux at 12.85 m on beamline no. 5 with the linac operating at a power of 7 kW.

High precision neutron flux measurements performed at GELINA have shown that the flux $\Phi(E)$ as a function of the energy in the region above thermal energies can be described by the general form

$$\Phi(E) = KE^{\alpha(E)} \tag{33}$$

the exponent $\alpha(E)$ being a function of the energy expressed as

$$\alpha(E) = a_0 + a_1 E^{1/2} + a_2 E. \tag{34}$$

The constant K depends on the operating power of the linac and the flight distance. The absolute neutron flux at a flight distance of 12.85 m with the linac functioning at 7 kW is plotted as a function of the energy in figure 12. The flux in flight path no. 5 for this large neutron energy range is obtained from measurements in the thermal region [93] and above thermal [94] and converted to the mentioned flight distance and operating power by applying the appropriate factor K.

2.2. The time-of-flight method

To perform measurements involving neutrons in a broad energy range, the time-of-flight method is very suitable. The principle is that the time that the neutron takes to travel along a known distance, is measured. From the flight time the velocity is deduced and therefore the kinetic energy of the neutron. For the work reported in this thesis we are dealing with

non-relativistic neutrons with energies below 1 keV and therefore the relation between the neutron energy, the flight time T and the flight distance L is just the expression for kinetic energy

$$E_n = \frac{1}{2} m_n \left(\frac{L}{T} \right)^2 \tag{35}$$

where m_n is the neutron mass. When we give the length in meters and the time in micro-seconds, the expression becomes in numerical form

$$E_n [\text{eV}] = 5227.039 \left(\frac{L [\text{m}]}{T [\mu\text{s}]} \right)^2 . \tag{36}$$

The very precise value of the proportionality constant is related to the recommended accurate value of the neutron mass from ref. [95].

neutron energy resolution

The experimental uncertainty in the measurement of the neutron energy comes from several factors, accounted for as uncertainties in the flight distance and flight time from which the spread in the energy follows

$$\frac{\delta E_n}{E_n} = 2 \sqrt{\left(\frac{\delta L}{L} \right)^2 + \left(\frac{\delta T}{T} \right)^2} . \tag{37}$$

There are several factors that affect the energy resolution, related to the uncertainty in time or in flight length. The flight time T is measured as the difference between the moment of production of the neutron, marked by a start signal T_0, supplied by the accelerator, and the arrival of the neutron at the target, marked by the detection of a reaction product, giving a stop signal T_n. The reaction product may be a neutron in scattering and transmission experiments, or a photon in the case of (n,γ) reactions. The time scale of the reactions is extremely small compared to the neutron flight time and does not contribute perceptibly to the uncertainty in flight time. The detector responses, however, can be in the order of nanoseconds for germanium detectors and can affect the time resolution, notably for short flight times.

Also the neutron burst is not instantaneous but it has a finite duration and thus it contributes to the timing error. Another factor is the effect of the neutron moderator near the neutron production target. As already mentioned before, the moderator causes the major uncertainty in the flight time. It is customary to express this rather in the form of an uncertainty in the flight length $\langle d_{mod}^2 \rangle$. For flight path number 5 where the experiments described in this thesis were performed, this quantity is in the energy range from thermal to 400 eV on the average [89]

$$\langle d^2_{mod} \rangle = 2.95 \quad \text{cm}^2. \tag{38}$$

A further contribution is the flight length and timing uncertainty due to the sample which has a finite thickness. Moreover, a thick sample causes multiple scattering: the neutron arriving at the target nucleus is not captured immediately, but may first scatter at another nucleus losing energy before it is captured. Neutrons at the high-energy side of a resonance may in this way fall into the peak region of the cross section. Therefore multiple scattering is visible in the cross section as a protuberance on the high-energy side of a resonance.

In the case of a heavy target of finite thickness a substantial part of the low energy gamma rays are absorbed due to the self-absorption in the sample if the detector views the sample at 90°. This might be resolved by using a thinner sample, which increases the measuring time, or by inclining the sample angle, and so decreasing the spatial resolution. To get an optimal efficiency for the gamma rays without losing too much time-of-flight resolution, a compromise must be found. For a sample of zero thickness in the form of a disc with radius R, with the normal of the disc making an angle ϑ with respect to the neutron beam, the mean squared distance to the centre of the sample is given by

$$\langle d^2_{angle} \rangle = \frac{\int_0^R (x \sin\vartheta)^2 (R^2 - x^2)\, dx}{\int_0^R (R^2 - x^2)\, dx} = \frac{1}{4} R^2 \sin^2\vartheta \tag{39}$$

which should be added to the uncertainty in flight length. For an angle $\vartheta = 30°$ and a sample diameter of 11.1 cm (^{238}U experiment) this gives $\langle d^2_{angle} \rangle = 1.93$ cm^2. The combination of this uncertainty and that due to the moderator forms the spatial uncertainty. Its contribution relative to the Doppler broadening is shown in figure 7 on page 25. At the used flight path of 12.85 m the spatial resolution corresponds to about 0.3% in the energy resolution.

2.3. Experimental setup

2.3.1 geometrical setup

The neutron beam coming from the moderator and travelling through an evacuated aluminium pipe is collimated to a diameter of 10 cm by a series of borated wax collimators, placed at appropriate distances. At the end of the flight path a 10 cm thick lead wall collimates the neutron beam once more before it enters into the experimental area where the target to be studied is placed in the beam. A schematic overview of the experimental setup together with the neutron beamline used in the ^{238}U measurement is shown in figure 13. The sample is viewed by one high purity intrinsic p-type germanium detector in the case

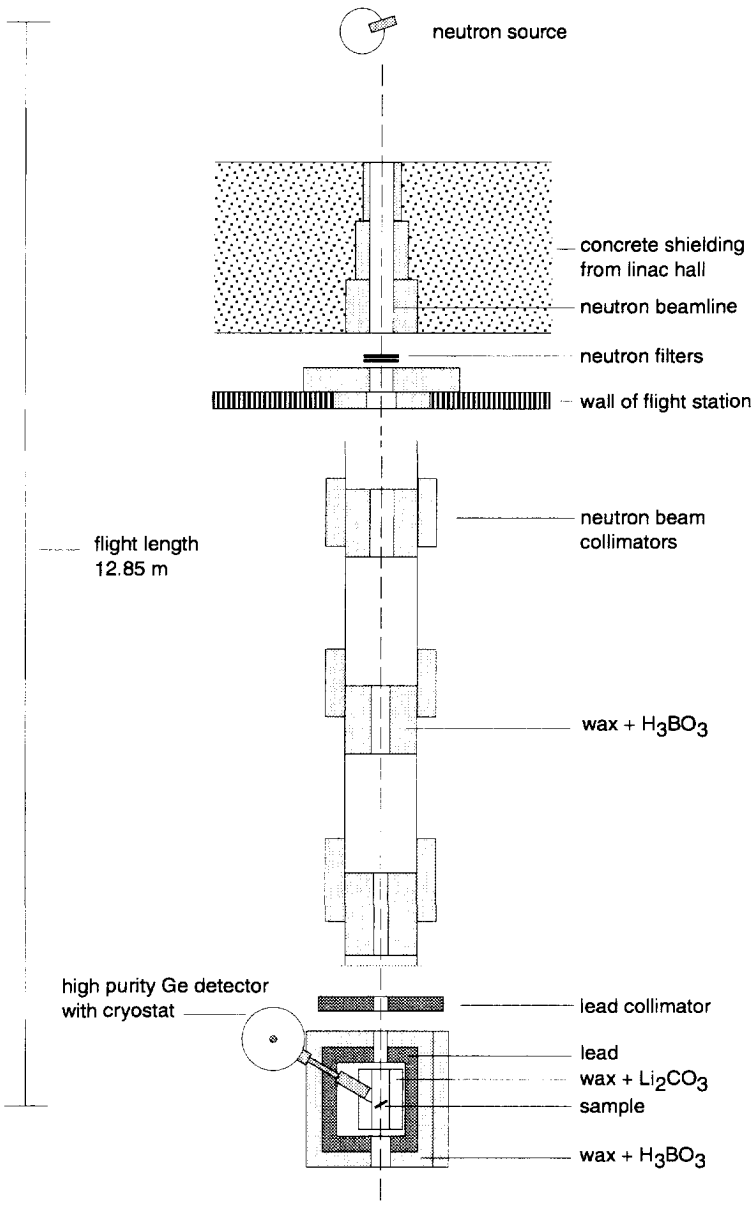

Figure 13: Schematic view of the neutron beamline with the measurement setup.

of the ^{238}U measurement and by two detectors in the case of the ^{113}Cd (see also page 75 and page 89).

The sample and the germanium detectors are surrounded by a considerable amount of shielding, consisting of a mixture of Li_2CO_3 and wax lined with a sleeve of ^{6}Li in an aluminium canning, in order to moderate and absorb the neutrons scattered from the sample. The detectors are shielded against scattered neutrons by an aluminium protection cover filled with ^{6}Li and an additional 3.5 cm of Li_2CO_3 on top. The whole assembly is placed inside a large shielding with walls made out of lead and a mixture of boric acid and wax, each 10 cm thick, to protect against outside radiation.

2.3.2 electronics

The pulses from the preamplifier of the detector are lead to two different chains of electronics: one determines the pulse height according to the energy absorbed in the detector and the second consists of fast electronics to determine the time of arrival of the pulse relative to the start time of the neutrons T_0. These two signals originating from the detection event are complementary and have to be related to each other in the data acquisition system.

One signal of the preamplifier of the detector is fed into a special spectroscopic amplifier and then led to an analog to digital converter (ADC), converting the pulse height into a channel number. The ADC is connected to a digital stabilizer that corrects the gain and zero offset by means of two very stable pulses. These pulses have to be set at the high and the low sides of the energy range of interest. The pulse at the high side is usually obtained from a very stable pulse generator, which is sent to the input of the preamplifier of the detector. Also the zero offset correction pulse can be obtained from a pulse generator but sometimes it is also possible to use a pronounced low-energy gamma ray of the capture spectrum. The pulse generators are triggered by the linac T_0 signal after an appropriate delay so that the stabilizing pulses fall outside the neutron time-of-flight region of interest.

The second output of the preamplifier is fed into a timing filter and shaper and then to a constant fraction discriminator to create a fast logic signal T_n, which is then sent to a 25-bit multiple shot fast time digitizer (FTD) with a minimum channel width of 0.5 ns. The FTD has as inputs the T_0 signal from the linac and the T_n signal coming from the detector. The FTD is initialized each cycle by the signal P_t, supplied by the accelerator and preceding the T_0 signal. The time difference between the T_0 and the T_n signals is then converted into a channel number and sent to the data acquisition system. The FTD provides also a logic signal to gate the ADC in order to ensure a coincidence. Whenever the time coder converts a T_n pulse, this signal, after being delayed to match the ADC pulse, enables the ADC so that there is a coincidence between the ADC pulse and the T_n pulse. The data acquisition system can now take both ADC and FTD values and store them as an event. This way of storing each event is called listmode. Together with the listmode data, other circumstantial data is taken amongst which the values of counters, proportional

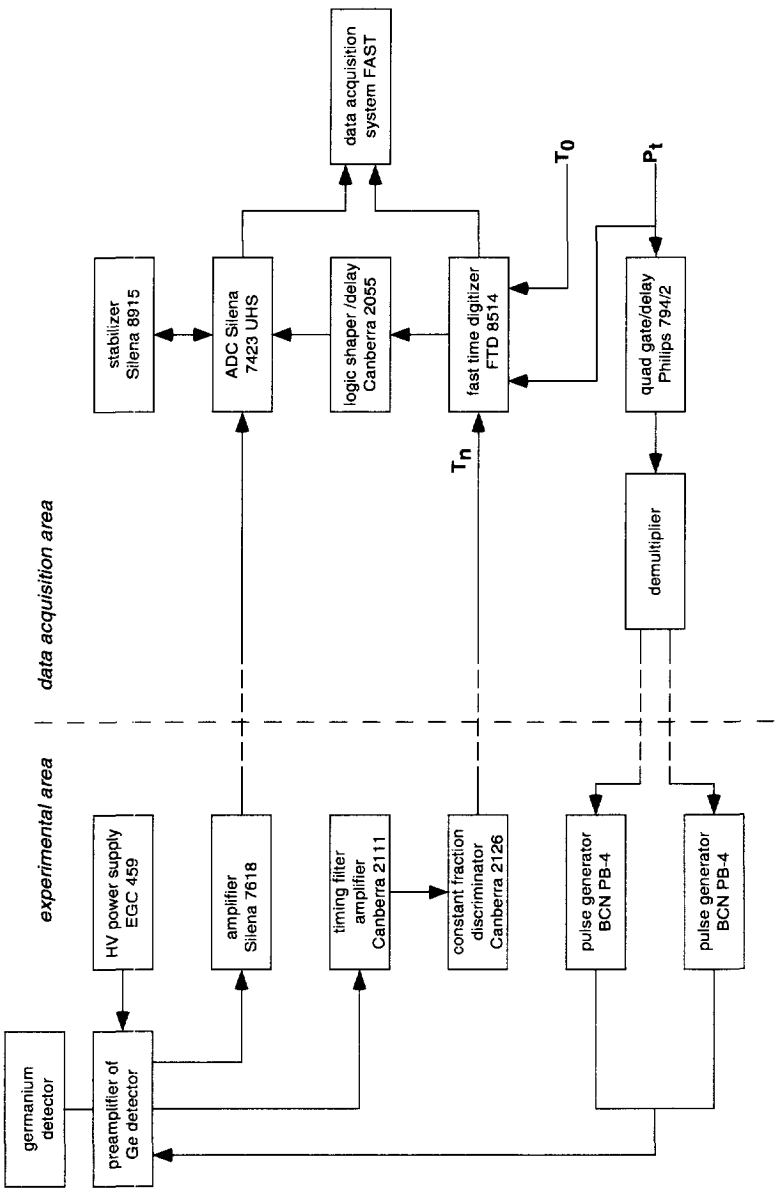

Figure 14: The essential units of the electronic setup of the capture gamma experiment for one detector.

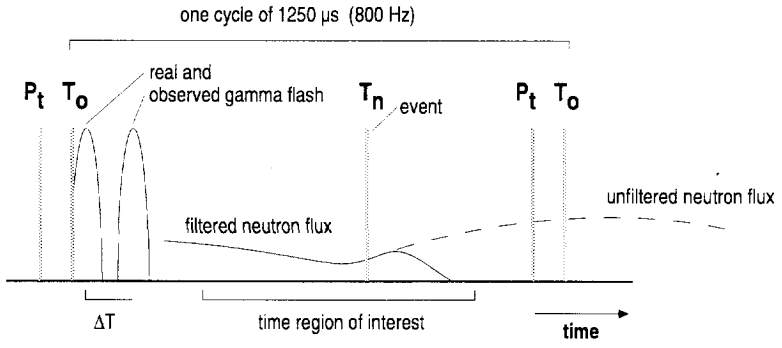

Figure 15: The several timing signals in one machine cycle of 1250 µs, the real and observed gamma flash and the filtered and unfiltered neutron flux.

to the neutron flux for normalization purposes. The electronic setup for one detector is drawn schematically in figure 14, showing the distinction between the part of the electronics that is at the experimental site where the sample is located and the part that is situated off site in the data acquisition area. Only the basic items are given in the figure, omitting the various counters and control signals.

The several timing signals in one cycle of the linac are shown in figure 15. The logic signal T_0 is preceded by the signal P_t to reset the time coder which is able to convert several signals in one cycle. The intense gamma radiation from the neutron producing target at time T_0, the gamma flash, is observed with a time delay ΔT in the detector. In order to know the precise time-of-flight of the observed neutron resonances, and therefore their energies, one needs to know the zero time. This is determined by observing the position of the gamma-flash peak in the TOF spectrum after correction for the delay $\Delta T = L/c$ introduced by the finite speed of light.

In the 800 Hz operation, one needs to eliminate the neutrons that have a flight time larger than the cycle time. In order to avoid the overlapping of slow neutrons from previous cycles a ^{10}B filter of suitable thickness is introduced. Also in figure 15 two neutron fluxes are shown. One shows the unfiltered neutron flux as it comes from the moderator. The Maxwellian peak of the spectrum at 0.025 eV is situated outside the 1250 µs region and overlaps with the next cycle. A boron filter absorbs the thermal neutrons, modifying the neutron energy spectrum so that approximately the whole spectrum fits within one cycle. It should be noted that the curves are just for illustration purposes and do not correspond to realistic fluxes.

The time region of interest must cover the neutron energy range to be measured. To cover the region from 3 to 1000 eV at L = 12.85 m, event signals T_n between 25 and 470 µs

must be included. This falls comfortably within the 1250 μs cycle time corresponding to the linac pulse repetition frequency of 800 Hz. For measurements at thermal energies (0.025 eV) the linac cycle should last longer and a frequency of 50 Hz is used.

2.4. Data acquisition system

The maximum time resolution of the FTD is 0.5 ns, much smaller than the width of neutron resonances at low energy. The coding into 25 bits provides about 30×10^6 channels, which is too much for practical purposes. The number of channels is compressed into a 32k channels TOF spectrum by means of a so-called "accordion". This is a part of the acquisition software that allows to specify several time regions in which the time part of the events will be binned into channels of a specific time width. After the compression, the TOF channels have a, not everywhere equal, width that is sufficiently large to map the TOF spectrum with acceptable resolution.

The events, consisting of an ADC and an uncompressed FTD value are taken in by the buffer derandomizer of the data acquisition system from the trademark FAST [96]. The buffer acts as to average large instantaneous counting rates so that the deadtime of this part of the system stays rather constant. The buffer is connected to a personal computer, storing the data, taking scaler values, keeping administration and making it possible to view the total TOF and ADC spectra on line. The ADC values and the compressed FTD values are stored together as an event on the 1 Gb hard disk of the computer in listmode. After having collected a certain amount of listmode events, the data are transferred to an Exabyte tape unit, for off-line analysis on another computer system. This system allows to handle the large amounts of incoming data which was for example about 600 Mb a day during 10 weeks in the case of the ^{113}Cd experiment. In figure 16 we show the schematic view of the flow of data in the data acquisition and analysis system. The advantage of storing list-

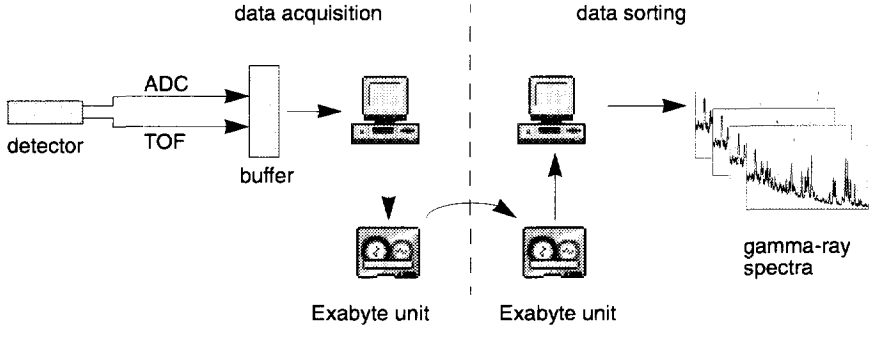

Figure 16: Schematic view of the flow of data for handling large data amounts.

mode data is that a re-analysis of the original data is always possible. This is often of interest because some structures may become visible only after a long period of measuring.

2.5. Data analysis

2.5.1 data reduction

The listmode data from the data acquisition system consist of a large number of events, each built up of four bytes. The first two bytes represent the ADC value while the second two bytes represent the corresponding TOF value. In a typical situation with 8192 ADC channels and 4096 TOF channels this means that each event can be placed in one of the 32 million bins on the two dimensional ADCxTOF grid.

The listmode data have to be sorted out in order to study the gamma-ray spectra corresponding to TOF intervals of interest, the neutron resonance- and background regions. This means that all the events in such an interval have to be taken together to form characteristic gamma-ray spectra as illustrated in figure 17. A computer program, taking care of the reading and sorting of the large amount of listmode data from an Exabyte tape unit into spectra has been developed [97]. Typically, a maximum of 200 gamma-ray spectra corresponding to as many TOF intervals can be built up in one pass.

A gamma ray spectrum S_r corresponding to a resonance interval, contains also the background gamma rays due to capture not related to this resonance. A pure spectrum S_p can

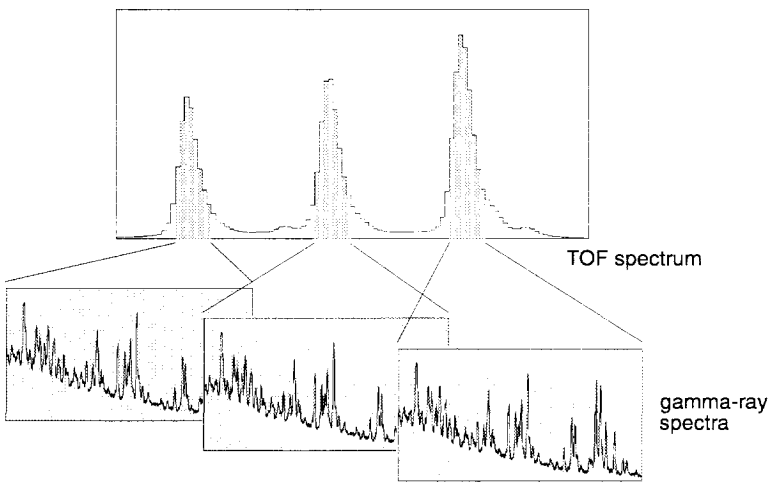

Figure 17: Gamma spectra corresponding to different TOF regions.

be obtained by subtracting the gamma ray spectrum S_b from a nearby background region. A scaling factor k has to be included to account for the different time widths of both intervals where k is the ratio of the time width of the background interval and the time width of the resonance interval. So the spectrum S_p, corresponding only to the resonant part can be constructed by

$$S_p = S_r - k \cdot S_b \tag{40}$$

and the variance of each channel in S_p is, using Poisson statistics

$$\mathrm{Var}(S_p) = S_r + k^2 \cdot S_b. \tag{41}$$

This applies to a single, well isolated resonance. For resonances that are overlapping with nearby ones, the procedure to extract the correct spectra is somewhat more involved. In that case, advanced computer codes for the parametrization of neutron spectra, like the multilevel program REFIT [81], have to be used. This has been the case for the measurements of ^{238}U, described in more detail in section 4.4. on page 75.

2.5.2 gamma spectrum analysis

Next the corrected gamma ray spectra corresponding to individual resonance capture regions have to be analysed in order to determine the positions and the areas of the gamma-ray peaks of interest. The response of semiconductor detectors allows that the shape of the detected gamma peaks can be adequately fitted by a Gaussian function combined with some function describing the low-energy tail. Effects of pile-up and properties of the electronics may also cause a tail at the high-energy side, but this can often be avoided with careful experimental design. Tailing effects on the low-energy side arise from a variety of causes like imperfect charge collection in the detector due to radiation damage.

The most appropriate mathematical form for the peak shape has to be determined for each individual detector. Several mathematical forms of low- and high-energy tails are given in refs. [98,99]. Good results for spectra with only a minor low-energy tail can be obtained by modelling the tail by a fifth order term [100]. The function $f(x)$ describing the peak as a function of the channel x is then split into two parts $f(x) = f_L(x) + f_H(x)$, at the low- and high-energy side of the peak position μ. The high-energy part is a standard Gaussian function while the low-energy part is a Gaussian modified by a tail governed by the asymmetry parameter κ

$$\begin{aligned} f_L(x) &= u(\mu - x) \cdot (1 - \kappa (x-\mu)^5) \cdot \frac{A}{\sqrt{2\pi\sigma^2}} \exp\left(-\frac{(x-\mu)^2}{2\sigma^2}\right) \\ f_H(x) &= u(x - \mu) \cdot \frac{A}{\sqrt{2\pi\sigma^2}} \exp\left(-\frac{(x-\mu)^2}{2\sigma^2}\right) \end{aligned} \tag{42}$$

where $u(x)$ is the unit step function. The parameters σ and A are respectively the width and the area of the ordinary Gaussian. In figure 18 the asymmetric Gaussian for two nonzero values of the asymmetry parameter κ is given. The area of the modified Gaussian equals no longer A but is given by

$$\int_{-\infty}^{\infty} f(x)dx = A\left(1 + 4\kappa\sigma^2\sqrt{\frac{2}{\pi}}\right). \tag{43}$$

Algorithms for least-squares minimization of nonlinear functions are still further developed [101,102]. In our case the obtained gamma-ray spectra were in most cases well fitted by an unmodified Gaussian using the Levenberg-Marquardt nonlinear least squares fitting algorithm [103]. However, in some cases the spectra showed a low-energy tail presumably due to radiation damage of the detector. In these cases the asymmetric peak shape of eq. 42 was adopted.

A well known phenomenon is that the full width at half maximum (FWHM) of the Gaussian peaks, related to σ as FWHM $= \sigma\sqrt{8\ln 2}$, is increasing with the gamma-ray energy. In a short energy range however, this may be considered as a constant and one can use well isolated peaks in order to derive σ and keep this as a fixed parameter in the fitting for neighbouring overlapping peaks.

The FWHM of a peak is also related to the neutron energy of the resonance to which it belongs (see also figure 34 on page 77). For a gamma ray with a specific energy, the FWHM increases with neutron energy. This is due to the increase of the instantaneous counting rate at short flight times and to the influence of the tail of the saturated peak corresponding to the gamma flash. If one wants to fix σ or the peak position in a gamma-ray spectrum of a weak p-wave resonance, one should find these parameters in spectra of a nearby s-wave resonance having good statistics.

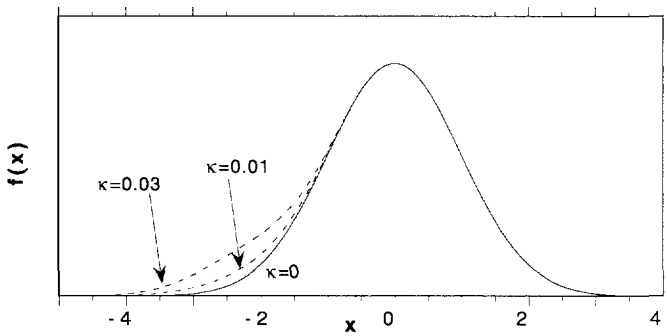

Figure 18: The asymmetric Gaussian shape for several values of the asymmetry parameter κ with $\sigma = 1$, used in the fitting of gamma-ray peaks.

2.5.3 estimate of the count rate

The count rate C in the detector, expressed in gamma rays per second, for a specific gamma-ray energy E_γ of a resonance at neutron energy E_R is the product of the number of captured neutrons per second and the number of photons per capture I_γ, multiplied by the detection efficiency ε_T

$$C(E_\gamma, E_R) = \varepsilon_T(E_\gamma) \cdot I_\gamma \cdot \int S\Phi(E_n) Y(E_n) dE_n \tag{44}$$

where S is the area of the sample and Φ the neutron flux. The radiative capture yield $Y(E_n)$ is the probability for an incident neutron of energy E_n to be captured in a sample of thickness N in atoms per barn, giving a gamma ray

$$Y(E_n) = (1 - e^{-N\sigma_T}) \frac{\sigma_\gamma(E_n)}{\sigma_T(E_n)} \cong N\sigma_\gamma(E_n) \tag{45}$$

where σ_T is the total cross section and σ_γ the radiative capture cross section. The approximation holds for thin samples, i.e. $N\sigma_T \ll 1$, which is certainly the case for the weak p-wave resonances. With a considerable background cross section underneath a p-wave resonance, the flux decreases over target thickness. If the flux is considered to be constant over the resonance, the count rate can be written as

$$C(E_\gamma, E_R) = \varepsilon_T(E_\gamma) \cdot I_\gamma \cdot S \cdot \Phi(E_R) \cdot N \cdot A_\gamma \tag{46}$$

where A_γ is the capture area given by

$$A_\gamma = 2\pi^2 \lambda\!\!\!^{-2} \frac{g\Gamma_n \Gamma_\gamma}{\Gamma} \cong 2\pi^2 \lambda\!\!\!^{-2} g\Gamma_n \tag{47}$$

if $\Gamma = \Gamma_n + \Gamma_\gamma \cong \Gamma_\gamma$, as is the case for p-wave resonances in the heavy mass nuclei ^{238}U and ^{113}Cd. We can put in some typical numbers for the ^{238}U experiment: $S = 100$ cm^2, $N = 6\times10^{-3}$ atoms / barn and assuming $I_\gamma = 0.1$ photons / capture. The total efficiency ε_T is the product of the reduction due to the self-absorption of gamma rays in the sample, about 0.6 for 600 keV gamma rays, and the measured photopeak efficiency $\varepsilon = 1.2\times10^{-3}$ for a 662 keV gamma ray of a calibrated ^{137}Cs point source with the detector placed at 15 cm as in the actual experimental conditions. The neutron flux of eq. 33 should be modified by the transmissions $T = 0.58$ of the U-filter and $T_{10.2\ \mathrm{eV}} = 0.57$ of the B-filter placed in the neutron beam. The capture area is $A_\gamma = 4.1\times10^6 E_n^{-1} g\Gamma_n$ barn·eV, giving

$$C = 4.2\times10^5 \cdot E_n^{-1.9} \cdot g\Gamma_n \quad \text{counts / s}. \tag{48}$$

For example for the resonance at 10.2 eV in ^{238}U with $g\Gamma_n = 1.65$ μeV, this gives an expected count rate of about 30 counts / hour for 600 keV gamma rays.

Chapter 3

Simulations of the gamma-ray spectra of radiative capture

3.1. Introduction

When a neutron is captured by a target nucleus, it forms a compound nucleus and decays through gamma-ray emission to its ground state (or any metastable state). The low-level resonance spin assignment method is based on the fact that the intensity ratio for specific gamma rays in the decay of a compound state depends on its spin. Within the statistical model, the probability of decay to a particular state is dependent on several parameters like the density of levels and the energy and multipolarity of the emitted radiation. Besides that, the probability of each transition is also subject to random fluctuations following a Porter-Thomas distribution.

Because the low-level population method is based on the statistical principles of the gamma decay of the compound nucleus, this process is suitable to be modelled in a numerical way using a Monte Carlo algorithm. For that purpose the compound nucleus has to be parametrized using the information about, among others, the spin and parity of the resonance state, the level density, the photon strength functions and the spectral data in the low-level region. We have used the FORTRAN computer code DICEBOX, which has been developed by Becvar and Ulbig [104], in order to simulate the gamma-ray spectra of the reactions $^{238}U(n,\gamma)^{239}U$ and $^{113}Cd(n,\gamma)^{114}Cd$.

Numerical simulations support the spin assignment experiments in the way that they can select the gamma rays that are most sensitive to the resonance spin and reproduce the splitting of the ratio of the intensities of two specific gamma rays according to the resonance spin groups when compared to experimental data. Our purpose was to study the population of the low lying discrete levels. We have customized the program on a few points to meet our needs. In this chapter the program DICEBOX is described and also some models for the photon strength and level density functions. Subsequently, the decay of the statistically populated levels to the ground state, which is not a statistical process but is based on known branching ratios in the low-level region, is discussed. Finally, the results of the simulations for the decay of the compound nuclei ^{239}U and ^{114}Cd, formed by neutron capture, are described and compared to experimental results.

3.2. The program DICEBOX

The computer code DICEBOX simulates the process of statistical gamma cascade deexcitation of medium and heavy nuclei in a highly excited state, using a Monte Carlo algorithm. The program can be used in a variety of applications. The statistical model is believed to be valid in the excitation region several MeV above the ground state where the compound nuclear states are present. The lower levels just above the ground state do not behave statistically but transitions among these states are often known from measurements. Therefore, the excitation spectrum is divided into two parts: a low-lying part containing the discrete levels with known energies, spins and parities and a quasi-continuum part where the individual levels are not known any more. The levels in the quasi-continuum are very closely spaced and their energies and decay properties are assumed to obey the extreme statistical model of the nucleus. The program sets up a what we will call "nuclear realization" for the quasi-continuum part of the excitation spectrum. A nuclear realization is obtained by

- a process of random discretization of a chosen level density formula of which the result is a large set of levels forming the quasi-continuum, each level being represented by its excitation energy, spin and parity
- and a random generation of a full set of partial radiative widths that are responsible for the gamma decays of individual levels to all possible final levels.

The total number of levels is in the order of 10^6, so the number of partial widths for each level to all the lower levels is in the order of 10^{12}, making it impossible to store these quantities in the computer memory with current means. This problem has been solved by the introduction of so-called "precursors". These precursors are represented by randomly chosen seeds for a random generator function of the type RAN(I), generating values distributed uniformly on the interval (0,1). Each individual level has its own ascribed precursor. The random generator is a constituent part of a subroutine that provides random selections from the chi-square distribution with one degree of freedom. Whenever the need for generating partial radiation widths of a given level occurs, the random generator is initialized with the precursor of the level after which generating the partial radiation widths may start. The ascribed precursor is thus used to set the computer random generator into a specific, *a priori* adjusted status to initiate the process of generating widths, each level having its own fixed status within a given nuclear realization. So the partial widths of not all the levels are calculated, but only those of the accessed levels during the decay. This ensures that the decay of a level will proceed in exactly the same way any time the level is encountered in a cascade within a fixed realization. In this way the full set of strongly fluctuating partial radiation widths involved in a nuclear realization is kept constant, like the set of widths of a real nucleus. In a new realization, a different set of widths is calculated.

As the partial radiation widths for statistical transitions between two nuclear levels can be calculated, also the intensity branching ratios for each level can be calculated. Having this

possibility, the process of statistical gamma-decay cascade can be simulated by the Monte Carlo technique. In such a simulation the cascade decay stops at the first discrete level that is reached, obtaining the populations of the low lying states. Also the number of gamma decay steps needed to reach the first level is recorded for the calculation of the gamma-ray multiplicity. To obtain a measure of the spread in the populations, several nuclear realizations, each one with a large number of events, are calculated as well as the mean and standard deviation for the population of each level. The whole calculation results in a set of fractions of the number of events terminating at each discrete level together with the associated errors. As a by-product, for each discrete level a multiplicity spectrum of the statistical part of the cascade decay is obtained.

With an infinite number of events within one nuclear realization the population of a specific discrete level will tend to its particular expectation value. For another nuclear realization, with another set of levels and radiation widths, this asymptotic value is different. By taking many nuclear realizations, the mean value of the populations should represent the expectation value for the nucleus. The spread in the populations is merely a result of approaching the structure of the real nucleus by the different calculated realizations and has therefore no physical meaning. In practice, one uses a finite number of events for one realization and the expectation value for one nuclear realization is not reached. In this case the errors in the populations reflect also this fact.

The gamma-ray transitions are subject to Porter-Thomas fluctuations which means that the radiation intensities follow a chi-square distribution with one degree of freedom. As these fluctuations are responsible for a large part of the spread in the calculated populations, it is important that they are properly taken into account in the above-mentioned procedure for generating partial radiation widths. However, It should be noted that the inclusion of Porter-Thomas fluctuations drastically increases the necessary computation time. Nevertheless, the calculations have shown that for this specific application, deriving the population of the discrete levels, the use of Porter-Thomas fluctuations affects the final value only a little.

The initial state, observed as a resonance in the neutron capture reaction, is characterized by the spin, parity and the energy excitation above the ground state. In the simulations, the excitation of the initial state is taken equal to the neutron separation energy since the energies of the neutron resonances, which are in the eV range, can be neglected. Because of the assumed parity independent high level density in the quasi-continuum and the generally large average gamma multiplicity, the resonance parity should not appreciably affect the low-level populations. Indeed the simulations for resonances with the same spin but opposite parity give values that overlap within their errors.

In fact, up to this point a population of any discrete level was understood to be the result of the cascade decay of the quasi-continuum to that particular discrete level without any other intermediate level belonging to the discrete region involved. However, in order to

compare the simulated results with those from experiment it is necessary to take into account also the successive decay of the discrete levels. For this reason in our calculations the resulting populations of the individual discrete levels include as well additional contributions originating from cascades that proceed via discrete levels. The transition probabilities between low lying states are not governed by statistical transitions as their corresponding matrix elements often result from a combined overlapping of a multipole projection of the initial state wave function with single-particle and collective components of the final state wave function. However, these transitions have mostly been measured for thermal capture gamma rays and information about the branching ratios is generally available, for example in Nuclear Data Sheets. We take these branching ratios, which are a property of the nucleus and not unique to thermal capture and use them for the resonance capture gamma rays. The fraction, corresponding to the branching ratios, of the statistical populations and their errors are carried over to the lower states in the decay calculation where the appropriate error propagation has been used in adding the intensities.

The output of our version of DICEBOX consists of a text file, containing some general information, the input parameters, general calculated data and a list of the discrete levels with their mean population and standard deviation resulting from several nuclear realizations.

random numbers

An essential aspect in Monte Carlo simulations is the random number generator. This is the algorithm to produce a sequence of numbers which are pseudo-stochastic, usually uniformly distributed. Because of the method of its production, a numerical algorithm, such a sequence can never be fully random. There are always correlations in the sequence and the distribution is not exactly uniform. It depends on the type of simulation to what extend the random numbers should be uncorrelated.

The program DICEBOX uses a random number function of the form RAN(I). This type returns a random number from a uniform distribution by supplying a seed number I, and uses the random number as the new seed. Many types of random generator algorithms exits and new ones are still developed [105-107]. For a review see for example refs. [108-110]. Instead of using the random number function supplied by the computer system, we have implemented a machine independent portable multiplicative linear congruential generator (MLCG) with recommended parameters from ref. [108]. The parameters of this type of random number generators influence the length of the repetition period of the generator. However, the drawback of this type of generators is that there exists a correlation between consecutive values. As a matter of fact, also most computer systems use MLCG generators but the parameters may vary from one system to another and therewith the repetition period and degree of correlation. Once a uniform deviate is obtained, various algorithms can transform it into samples of other distributions [103].

3.3. Photon strength functions

The radiative transition strength of the nucleus between two states can be accounted for by the multipole operators. This enables us to derive expressions for the transition probabilities of multipole radiation [78,111]. Rather than the decay rate per second λ, the radiative width $\Gamma_W = \hbar\lambda$ is used. These widths have been calculated and are known as the Weisskopf estimates. For electric and magnetic dipole and quadrupole radiation the widths (in eV) as a function of the gamma ray of energy E_γ (in MeV) and the mass number A can be expressed as [112]

$$\Gamma_{W,E1} = 6.8\times10^{-2}A^{2/3}E_\gamma^3 \tag{49}$$

$$\Gamma_{W,E2} = 4.9\times10^{-8}A^{4/3}E_\gamma^5 \tag{50}$$

$$\Gamma_{W,M1} = 2.1\times10^{-2}E_\gamma^3 \tag{51}$$

$$\Gamma_{W,M2} = 1.5\times10^{-8}A^{2/3}E_\gamma^5 \tag{52}$$

where the numerical constants are based on the nuclear radius parameter R_0, here taken as 1.20 fm. Although these estimates are not meant to be realistic predictions, they provide a good relative comparison. The lower multipoles are stronger than the higher ones and for a given multipole, the electric one is stronger than the magnetic one. Blatt and Weisskopf [113] have first modelled the average partial widths for electromagnetic radiation in compound nuclear states within the frame of the single-particle model. The expressions for the radiative widths in eV are related to the Weisskopf estimates as

$$\Gamma_{XL} = \Gamma_{W,XL}\cdot\frac{D}{D_0}\cdot10^{-6} \tag{53}$$

where $D = 1/\rho(J_i^\pi)$ (in eV) is the spacing of the initial levels with the same spin and parity and D_0, expressed in MeV and therefore introducing the factor 10^{-6}, is the spacing of the single particle states, originally taken as 0.5 MeV but mostly taken as an adjustable parameter.

The average partial radiative width $\langle\Gamma_{XL}\rangle$ for a transition of the type X (E for electric, M for magnetic transitions) and multipolarity L, from an initial state i, has the general form

$$\langle\Gamma_{XL}\rangle = \frac{S_{XL}\cdot E_\gamma^{2L+1}}{\rho(J_i^\pi, E_i)} \tag{54}$$

where $\rho(J_i^\pi, E_i)$ is the density of levels having spin and parity J^π and where S_{XL} is the photon strength which is a constant in the single particle model. Usually, $\langle \Gamma_{XL} \rangle$ and $1/\rho$ have the same units and are expressed in eV, while E_γ is expressed in MeV. The unit of S_{XL} is then $\text{MeV}^{-(2L+1)}$. The strength S_{XL} is often expressed in terms of Weisskopf units (W.u.) per MeV to reveal the deviation from the single particle strength. While doing so, one should specify the used value of D_0.

Unlike the neutron strength function, which has a unique definition, a lot of photon strength functions exist in the literature. To analyse and compare experimental data, the reduced photon strength functions k_{XL}, as defined by Bartholomew [116] for dipole radiation, are often used

$$k_{E1} = \frac{\langle \Gamma_{\gamma E1} \rangle \rho\,(J_i^\pi, E_i)}{E_\gamma^3 A^{2/3}} \tag{55}$$

$$k_{M1} = \frac{\langle \Gamma_{\gamma M1} \rangle \rho\,(J_i^\pi, E_i)}{E_\gamma^3} \tag{56}$$

where the units are as before so that k_{X1} is expressed in MeV^{-3}. In the same way, one can define k_{E2} etcetera. In the single particle model, the quantities k_{XL} are constants.

Experimental data on photon strength functions have been obtained by neutron-capture spectroscopy, mostly by considering primary transitions. A method to gather information on strength functions is the use of sum-coincidence measurements of two-step cascades [114,115]. This method is not only sensitive to primary, but also to secondary transitions.

The single particle model agrees quite well with experimental data for $M1$ transitions (see for example also ref. [117]). But in particular for $E1$ radiation other models, more adequately describing the experimental data on gamma-ray transitions, have been developed. In this respect we have used the Lorentzian shape of the giant dipole resonance and also the Kadmenskii model. For $M1$ and $E2$ radiation we have used the single particle strengths.

$E1$ radiation: Lorentzian shape of the Giant Dipole Resonance

Cross sections of photonuclear reactions showed the existence of $E1$ giant dipole resonances (GDR), explained as collective dipole vibrations of the protons and neutrons in the nucleus. These excitations are for heavy and medium mass nuclei far above the neutron threshold energy. The assumption is that this collective motion is independent from the internal nuclear motion and that a GDR is built not only on the ground state, but also on any excited state. This makes it possible to express the average partial radiation width $\Gamma_{\gamma E1}$ in terms of the experimental photoabsorption cross section σ_G. The strength function S_{E1} as defined in eq. 54 is now no longer a constant, but depends on the energy.

Assuming the standard Lorentzian shape for photoabsorption (see for example ref. [77]), the strength function is

$$S_{E1}(E_\gamma) = \frac{\sigma_G}{3(\pi\hbar c)^2} \frac{E_\gamma \cdot \Gamma_G^2}{(E_\gamma^2 - E_G^2)^2 + E_\gamma^2 \cdot E_G^2} \tag{57}$$

expressed in MeV^{-3}, where σ_G is the giant dipole peak cross section, E_G the resonance energy and Γ_G the GDR damping width. For deformed nuclei, like for example ^{239}U, the strength function is well described by two Lorentzians, each one associated with one of the two independent collective vibrational electric dipole modes of the ellipsoid. Some modifications of the expression of the Lorentzian exist, see for example Kopecky and Uhl [118], introducing a temperature dependent damping width as in the Kadmenskii model. In the present simulations we have used the standard Lorentzian with parameters taken from Berman *et al.* [119]. For ^{114}Cd these are $E_G = 15.8$ MeV, $\Gamma_G = 6.3$ MeV and $\sigma_G = 0.226$ barn, while for ^{239}U the parameters of the two Lorentzians are respectively $E_G = 10.92$ and 13.98 MeV, $\Gamma_G = 2.6$ and 4.72 MeV and $\sigma_G = 0.291$ and 0.383 barn.

$E1$ radiation: Kadmenskii model

Kadmenskii *et al.* [120] developed a model based on an approximation from the Fermi theory of liquids valid for $E_\gamma \ll E_G$

$$S(E_\gamma, T) = \frac{0.7\sigma_0}{3(\pi\hbar c)^2} \frac{E_G \Gamma_G \Gamma(E_\gamma, T)}{(E_\gamma^2 - E_G^2)^2} \tag{58}$$

where the damping width is given by

$$\Gamma(E_\gamma, T) = \frac{\Gamma_G}{E_G^2}(E_\gamma^2 + 4\pi^2 T^2) \tag{59}$$

T being the nuclear temperature. This model gives generally good agreement with experimental results for spherical nuclei, like ^{114}Cd.

$M1$ radiation

The single particle model for the $M1$ photon strength assumes a constant, mass independent value for the magnetic strengths S_{ML}. In the collection of photon strength functions derived from neutron resonance data of McCullagh *et al.* [117], this value has a global average of 3×10^{-8} MeV^{-3}, or 1.4 W.u. MeV^{-1} assuming a single particle level spacing $D_0 = 1$ MeV. This is just an average value and for specific nuclei this value might differ, but it is always in this order of magnitude, see for example results of Coceva [121] who found a strength of 0.6×10^{-8} MeV^{-3} in ^{53}Cr, also found in ^{106}Pd by Kopecky *et al.* [122] and used by Cejnar *et al.* [123] in other calculations. In the model calculations we use the single particle model for $M1$ radiation with parameter $S_{M1} = 0.6\times10^{-8}$ MeV^{-3}.

***E2* radiation**

In the single particle model the $E2$ strength function depends on the mass A as

$$S_{E2} = k_{E2} \cdot A^{4/3} \tag{60}$$

where the constant k_{E2} is the reduced photon strength function. Due to its weak strength, not much experimental information is available for the $E2$ strength function. Data from Prestwich [124] and Kopecky [125] suggest a value around $S_{E2} = 5\times10^{-11}$ MeV^{-5}. Since the $E2$ strength is much weaker than for $E1$ and $M1$ radiation it has very little influence on the simulated data. We have used $k_{E2} = S_{E2}/A^{4/3} = 4.8\times10^{-14}$ MeV^{-5} in the simulations.

3.4. Level density functions

The density ρ of levels having spin and parity J^{π}, is a function of the energy E, the spin J and the parity π. The topic of level densities has been treated by many authors, see for example refs. [126-129]. The positive and negative parities are taken throughout this work to be equally distributed in the quasi-continuum, independently of energy and spin, although also models exists with a parity dependence [130]. We discuss here two models which have been parametrized for many nuclei: the constant temperature formula and the backshifted Fermi gas model.

constant temperature formula (CTF)

Experimental data show an exponential increase of the cumulative number of levels $N(E, J)$ with energy at low excitation energies. The density of levels $\rho = \partial N/\partial E$ can be described reasonably well by the constant temperature formula

$$\rho(E, J) = f(J) \cdot \frac{1}{T}\exp\left(\frac{E - E_0}{T}\right) \tag{61}$$

where T, the nuclear temperature, and the parameter E_0 have to be fitted from available data. At higher energies, this model does not correspond with the experimental level densities. We tested this model with the parameters E_0 = -0.94 MeV and T = 0.419 MeV for ^{239}U and E_0 = -0.40 MeV and T = 0.615 MeV for ^{114}Cd [131].

The level density contains the spin distribution factor $f(J)$ which is described by [127]

$$f(J) = \exp\left(\frac{-J^2}{2\sigma_c^2}\right) - \exp\left(\frac{-(J+1)^2}{2\sigma_c^2}\right) \tag{62}$$

often approximated by

$$f(J) \cong \frac{2J+1}{2\sigma_c^2} \exp\left(\frac{-J(J+1)}{2\sigma_c^2}\right) \tag{63}$$

or slightly more correct by

$$f(J) \cong \frac{2J+1}{2\sigma_c^2} \exp\left(\frac{-\left(J+\frac{1}{2}\right)^2}{2\sigma_c^2}\right). \tag{64}$$

Von Egidy *et al.* [131] have compiled experimental data on nuclear level densities and have given a mass dependent form for σ_c

$$\sigma_c = (0.98 \pm 0.23) A^{(0.29 \pm 0.06)}. \tag{65}$$

We used a constant value for the spin cutoff factor $\sigma_c = 4.80$ in our calculations for ^{239}U and $\sigma_c = 3.87$ in the case of ^{114}Cd.

backshifted Fermi gas model (BSF)

Bethe calculated the level density within the Fermi gas model where free nucleons are confined to the nuclear volume. This model is often used in a slightly modified form, the Bethe formula for the back shifted Fermi-gas model [132], introducing a backshift E_1

$$\rho(E, J) = f(J) \frac{1}{\sigma_c \sqrt{2\pi}} \cdot \frac{\sqrt{\pi} \exp(2\sqrt{a(E-E_1)})}{12 a^{1/4} (E-E_1)^{5/4}}. \tag{66}$$

This model takes into account all the levels: each state with spin J is $(2J+1)$ -fold degenerate, so the total number of levels is $\sum (2J+1) f(J) / \sum f(J) = \sigma_c \sqrt{2\pi}$ times larger than the observable level density. In eq. 66 this factor has been taken into account.

We have used here the compiled values of ref. [132] and took the values $E_1 = -0.14$ MeV and $a = 25.8$ MeV^{-1} as parameters for ^{239}U and $E_1 = 1.21$ MeV and $a = 14.48$ MeV^{-1} for ^{114}Cd.

3.5. Decay of low-lying states

The obtained populations of discrete levels are in fact the result of the statistical decay of the continuum part to the first discrete level reached. It is necessary to account also for the decay between the discrete levels to the ground state in order to compare the simulated results with experimental results. We have developed a separate program reading the output of DICEBOX and calculating all the transitions in the discrete level region. The transition probabilities between low lying states are not any more, like in the highly excited

states, governed by statistical transitions but by specific transition rates between the low-lying levels. We have taken the branching ratios from Nuclear Data Sheets for ^{239}U [133,134] and ^{114}Cd [135].

We have a set of N discrete levels labelled i that have a population S_i coming only from the statistical decay from the quasi-continuum region. What we observe in an experiment are gamma rays deexciting these states, so we have to calculate the intensities of these gamma rays. The population of a level i decays to all the lower levels according to the branching ratios $b_{i \to j}$, taken from the thermal neutron capture gamma ray spectra. When we count the N levels, the ground state is $i = 1$ and the highest discrete level has $i = N$. There are no metastable states present so the sum of the branching ratios from one level to all the lower levels equals 1

$$\sum_{k=1}^{i-1} b_{i \to k} = 1 . \tag{67}$$

The total population of a level P_i is composed of a part S_i from statistical feeding and a part originating from the decay of the higher discrete levels, so we can write for the population P_i of a level i

$$P_i = S_i + \sum_{k'=i+1}^{N} b_{k' \to i} P_{k'} . \tag{68}$$

It is clear that the highest discrete level in this way is fed only by statistical decay so $P_N = S_N$. The intensity of a gamma ray $I_{\gamma, i \to k}$ deexciting the state i to a state k is then simply

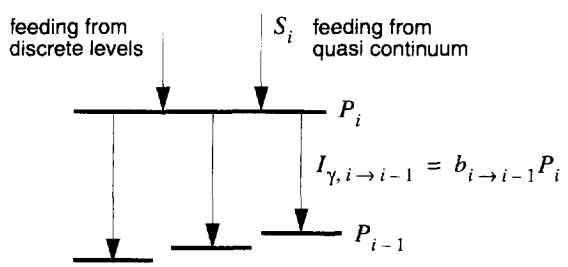

Figure 19: The modelling of the calculation of the transitions between low-lying discrete levels with the feeding and decay.

$$I_{\gamma, i \to k} = b_{i \to k} P_i \tag{69}$$

expressed in photons per captured neutron. The above mentioned quantities are illustrated in figure 19. In this way we can, starting at the highest level N, let the populations decay until the ground state is reached and in the meanwhile recording the intensity of the transitions $I_{i \to j}$. The fraction of the errors in the statistical populations S_i, corresponding to the branching ratio, is carried to the lower states in the decay calculation, using the appropriate error propagation in adding intensities.

gamma-ray multiplicity

The multiplicity of a decay process in the compound nucleus is the average number of gamma radiations emitted to reach the ground state. The program DICEBOX calculates for each event in how many steps it has reached the first discrete level, resulting in the fraction of the number of events for each step size. This can be considered as the distribution function $P_{stat}(\nu)$ of a partial multiplicity ν_{stat} associated with the statistical decay.

When calculating the decay of the discrete levels, track is taken of the number of steps needed for the decay of the fractions to the ground state. This can be considered as the distribution function $P_{low}(\nu)$ of a partial multiplicity ν_{low} connected to the decay of low-lying levels. A consequence is that this distribution has also a nonzero value for zero steps, because some events have already reached the ground state in the statistical decay. The real multiplicity is the sum of the two partial multiplicities

$$\nu = \nu_{stat} + \nu_{low} \tag{70}$$

and its distribution function $P(\nu)$ can be found, under the assumption that the two partial multiplicities are independent, by the convolution of the two previous distribution functions.

$$P(\nu) = P_{stat} * P_{low} = \sum_k P_{stat}(\nu - k) \cdot P_{low}(k). \tag{71}$$

The shape of $P(\nu)$ is different depending on the resonance spin. In a gamma-ray multiplicity experiment one can find the distribution and then compare experimental and simulated spectra to assign the spins [67]. One could also measure the average multiplicity

$$\langle \nu \rangle = \sum_\nu \nu P(\nu) / \sum_\nu P(\nu) \tag{72}$$

and make a distinction between the spin groups on such a basis. The present simulations for the cases ^{239}U and ^{114}Cd do indeed show different multiplicity spectra for different spins but the calculated average multiplicities are very similar and do not allow to make spin assignments. As an average value over all p-wave resonance spins and several employed models we obtained $\langle \nu \rangle = 4.8$ for ^{113}Cd and $\langle \nu \rangle = 4.7$ for ^{238}U. The differ-

ence in this value for the possible resonance spins within the same model of the nucleus is in the order of several percent.

3.6. Simulations of ^{238}U (n,γ) ^{239}U

The p-wave resonances of ^{238}U have spins J = 1/2 and 3/2. We have simulated the gamma decay of the excited ^{239}U nucleus from p-wave resonances at the neutron separation energy at 4.8 MeV to the ground state. The region between 1.265 and 4.8 MeV was taken as the statistical region and the program DICEBOX generated here levels according to the chosen level density function. In the region between the ground state and 1.265 MeV, 38 levels with known or assumed energies, spins and parities from the literature [134] were introduced into the program. Due to the very complicated structure of the spectrum of ^{239}U, it is not probable that these represent all levels. In figure 20 the spectrum is shown with the 25 positive and 13 negative parity (indicated with dots) states. Several levels with known energies but unknown spins or parities have been left out of the model. Levels with known energies, spin and parities but of which no transitions to lower-lying levels are known, have been included in the simulations. In total 64 transitions between levels in the

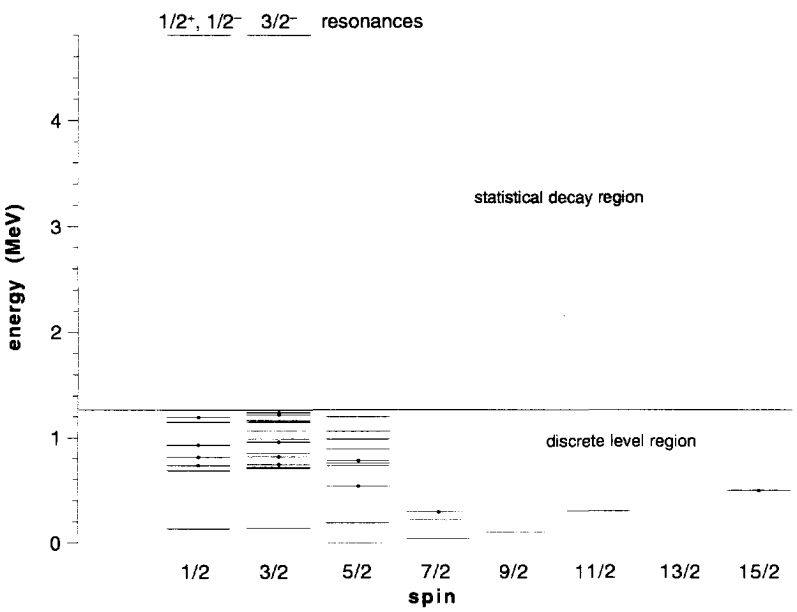

Figure 20: A schematic view of the nuclear realization of ^{239}U. The gray region between 1.3 and 4.8 MeV indicates the statistical region while below the discrete states are given for each spin. These levels have all positive parity except the 13 levels with dots.

low-energy region are known and have been used to obtain the gamma-ray spectrum in the low-energy part. As mentioned, of some levels no branching ratios to other levels were known, and therefore a small percentage, lower than 5%, of the events could not decay to the ground state in the simulations.

We have simulated several models of which a selection will be given here. A simulation consists of typically 100 nuclear realizations with each typically 100 000 events. We performed the simulations using two models for the level density and the $E1$ photon strength function. The results are presented in three steps. First the calculated populations of the discrete levels below 1.3 MeV are shown, then the intensities of the gamma-rays depopulating them, and finally the ratio of the intensity of specific gamma rays, in comparison with experimental data.

statistical populations of ^{239}U levels

In figure 21 the populations of the discrete levels due to the statistical feeding from the quasi-continuum are shown. In fact, the four plots give the statistical populations of the $1/2^+$, $1/2^-$, $3/2^-$ and $5/2^+$ levels using the standard Lorentzian shape and the Kadmenskii shape for the $E1$ photon strength. In both cases the BSF level density formula was employed while other models for the level density gave only slightly different results. The relative positions of the curves corresponding to a resonance spin 1/2 or 3/2 are denoted by the positions of the indications 1/2 and 3/2 in figure 21. From the figure it can be seen that the spin separation is present for the population of levels of all four spins and parities but the strongest effect occurs at the $1/2^+$ and $1/2^-$ levels. In the other cases the difference due to the two photon strengths is larger than due to the difference in resonance spin.

When the Kadmenskii model is used, the statistical populations are very similar for the $1/2^+$ s-waves and the $1/2^-$ p-waves. Only for the $1/2^+$ and $1/2^-$ discrete levels the difference is somewhat larger using the Lorentzian shape. The results given here come from initial states with negative parity. To compare these statistical intensities with the experimental values, the gamma transitions from the levels should be calculated.

gamma-ray intensities of ^{239}U

The transitions between the low-lying states involve 64 known gamma transitions. Only those were taken which show in thermal capture an intensity of more than 5% and those of interest for the experimental spin determination. The gamma ray of 537 keV is observed in the experiment but the spin and parity of its parent state are not known and therefore it has not been included in the simulations. We have also included two gamma transitions of 554 keV. The strongest of them is from a $1/2^+$ state at 688 keV while the other component of the doublet depopulates a $3/2^-$ state from the 1242 keV level. The latter (the second 554 line in figure 22) has an intensity of only 20% of the former in thermal capture.

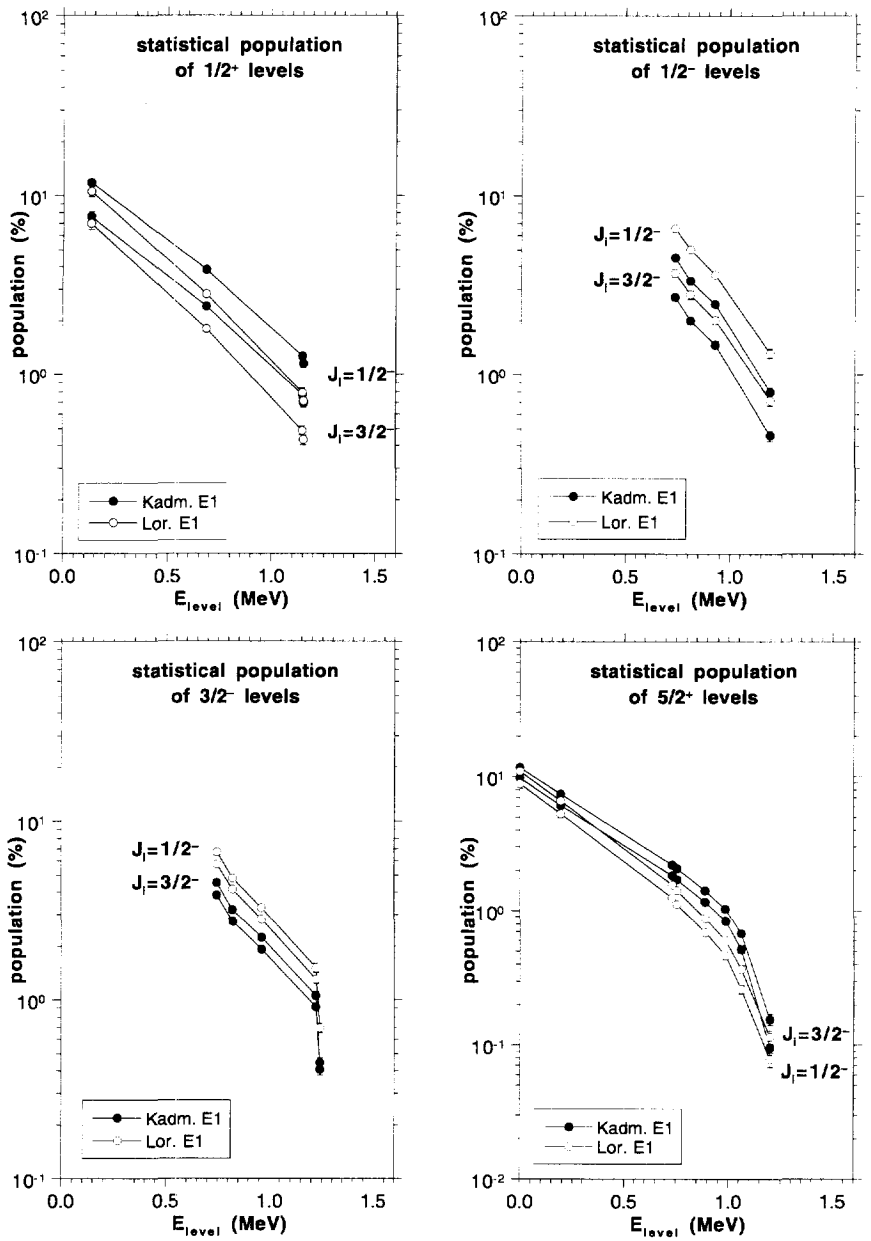

Figure 21: The statistical populations of low-lying levels of spin $1/2^+$, $1/2^-$, $3/2^-$ and $5/2^+$ in ^{239}U for the two resonance spins and for the Lorentzian and Kadmenskii photon strength functions.

In figure 22 the intensities of the 8 selected gamma rays are shown for the two p-wave resonance spins and for several models, using the Kadmenskii model and the simplest form of the Lorentzian model, both with the BSF level density. For the Lorentzian, also the results including Porter-Thomas fluctuations are given which do very much resemble the results without fluctuations.

For comparison also the intensities of the gamma rays for thermal neutron capture are given in figure 22. Especially for the 552 and the 612 keV lines the disagreement between the intensities coming from the thermal $1/2^+$ state and the $1/2^-$ state is remarkable. Both gamma rays deexcite a $3/2^-$ state which is strongly fed by the $1/2^+$ thermal capture state. This might also indicate the possible existence of a nonstatistical component in the decay, while in the simulations only the average primary gamma-ray strength was used.

The gamma rays deexciting levels with spin $J = 3/2$ show a small spin dependence while the gamma rays of $J = 1/2$ levels reveal a stronger effect. Also the gamma ray of 539 keV from a $5/2^-$ state exhibits a large effect which is opposite to the two previous cases. A ratio of gamma-ray intensities containing the two strongest lines at 539 and 554 keV has therefore an increased spin dependence. In the experiment described in the next chapter, these gamma lines were overlapping with neighbouring lines due to the resolution of the measured spectra.

comparison with experimental data of ^{239}U

In the experiment described in chapter 4 the spins of p-wave resonances are determined using the ratio of the gamma lines of 537, 539 keV and 552, 554 keV. However, the gamma transition of 537 keV deexcites a level at 1361 keV with unknown spin and parity. Therefore we could not include this level in the simulations, although it is important for the comparison with experimental data. But we still can compare the ratio of simulated intensities without the 537 keV line in the numerator of the ratio. Accordingly, the experimental ratio will be higher than the simulated one.

In figure 23 the simulated ratios are summarized for several employed models together with the values of the experiment. The numerical values are given in table 5 with an indication for the used models for the photon strength: the standard Lorentzian (L) and the Kadmenskii model (K). For the level density we used the constant temperature model (CTF) and the backshifted Fermi gas model (BSF). Also is specified whether Porter-Thomas fluctuations (PT) are included or not.

The correspondence between experimental and simulated values is quantitatively not completely in agreement which is due to the lack of knowledge of the detailed level scheme of ^{239}U. However, qualitatively the values show a clear spin dependence for all employed models and the difference in the ratios for the simulated values corresponds well with the experimental ones. The observed large difference in the ratios for the spin 1/2 s-wave resonances and p-wave resonances provides evidence that the $E1$ photon

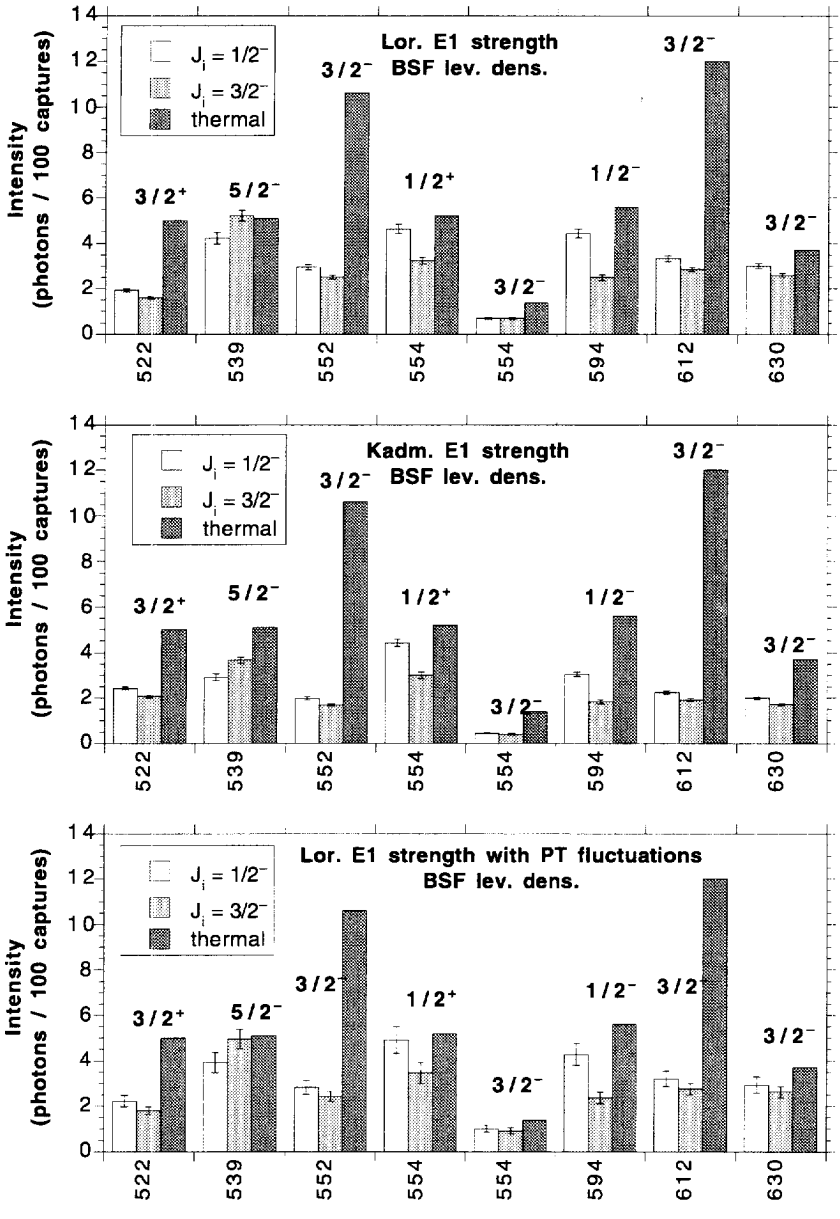

Figure 22: The intensities of selected gamma rays of ^{239}U with an intensity of more than 0.05 per thermally captured neutron for the two spin groups and for different $E1$ strength functions. The x-axis indicates the energy of the gamma-ray.

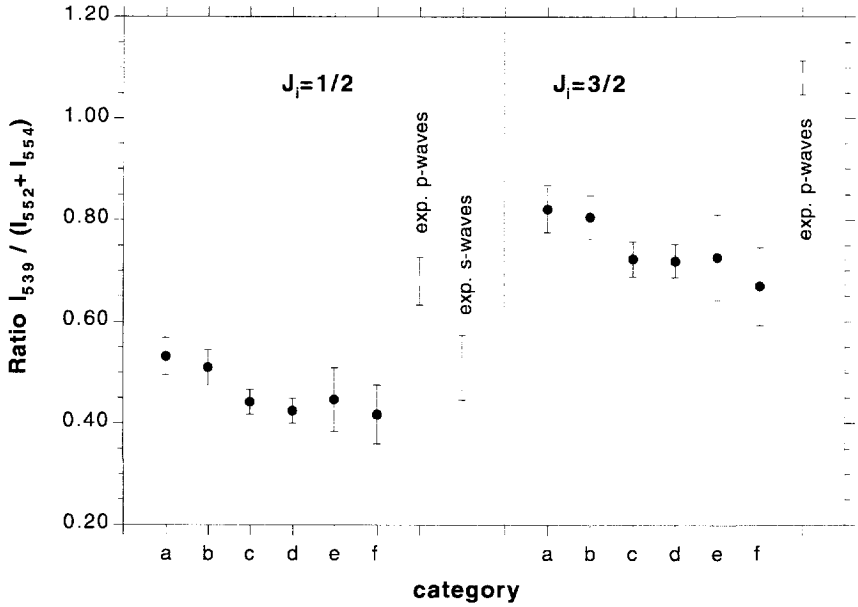

Figure 23: Comparison between experimental ratios and simulated values for ^{239}U. The employed models corresponding with each of the categories (a) through (f) are explained in the text and the numerical values are given in table 5.

strength function has a Lorentzian form since the results of the simulations also show a difference in the statistical populations when this strength function is used.

Table 5: The employed models and the numerical values for the simulations of the decay of ^{239}U.

category	**employed models**			**ratio J = 1/2**	**ratio J = 3/2**
	*E*1	ρ	PT		
a	L	CTF	no	0.532±0.036	0.822±0.046
b	L	BSF	no	0.510±0.035	0.806±0.043
c	K	CTF	no	0.442±0.024	0.724±0.035
d	K	BSF	no	0.425±0.024	0.720±0.033
e	L	BSF	yes	0.447±0.062	0.726±0.085
f	K	BSF	yes	0.418±0.058	0.670±0.077
exp. *p*-waves				0.680±0.047	1.080±0.033
exp. *s*-waves				0.510±0.064	

3.7. Simulations of ^{113}Cd (n,γ) ^{114}Cd

The ^{113}Cd neutron p-wave resonances have spins $J = 0$, 1 or 2. We have performed simulations for these three spins and both parities in order to calculate the dependence on the resonance spin of the gamma-ray transitions in the low energy region. The region from 2.8 MeV until the neutron threshold at 9.04 MeV was taken as the statistical region. This part has been filled with levels according to the chosen level density function and the statistical decay was governed by the photon strength functions. For the energy spectrum from the ground state up to 2.8 MeV we used 23 discrete levels with energy, spin and parity taken from the Nuclear Data Sheets [135]. These levels should represent quite completely the spectrum of the nucleus in this low excitation region. A schematic representation of the nuclear realization of ^{114}Cd is shown in figure 24. The decay of the discrete region to the ground state is well known from thermal neutron capture gamma rays. We have used the involved 99 gamma-ray transitions.

A simulation consists of typically 50 nuclear realizations, each one consisting of typically 50 000 histories. We performed the simulations using two models for the level density and two for the $E1$ photon strength function. The results are presented in three steps. First the

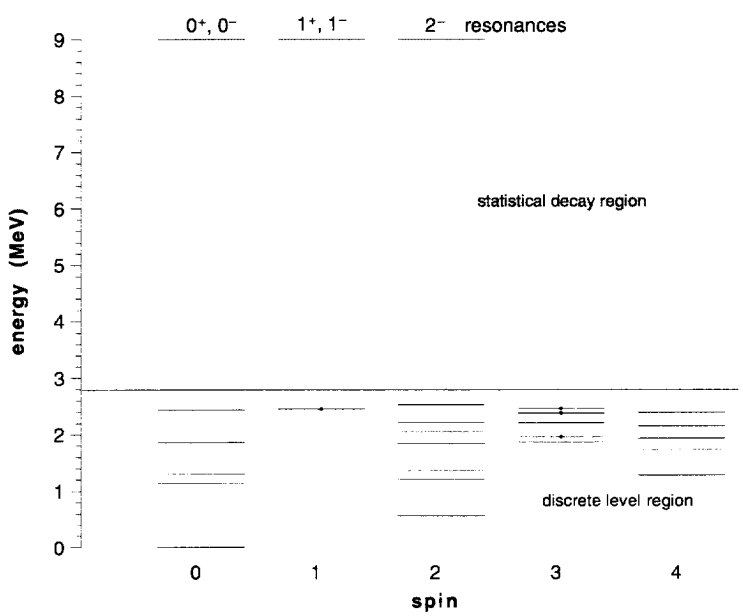

Figure 24: A schematic representation of the nuclear realization of ^{114}Cd. The gray region between 2.8 and 9.0 MeV indicates the statistical region while below the discrete states are given for each spin. These levels have all positive parity except the four levels with dots.

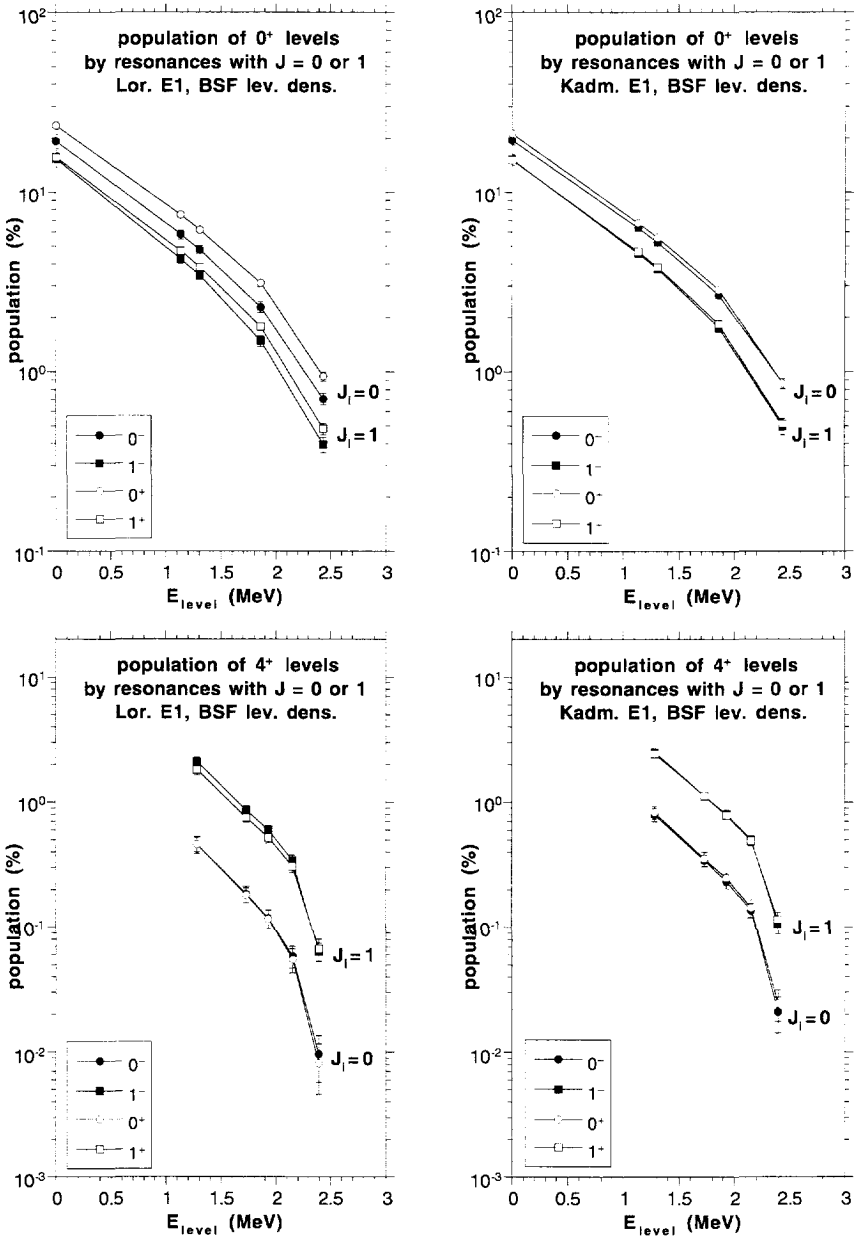

Figure 25: The populations of low-lying levels in ^{114}Cd of spin 0^+ and 4^+ for the resonance spins 0^+, 0^- and for 1^+ and 1^- using the Lorentzian and Kadmenskii $E1$ photon strength functions.

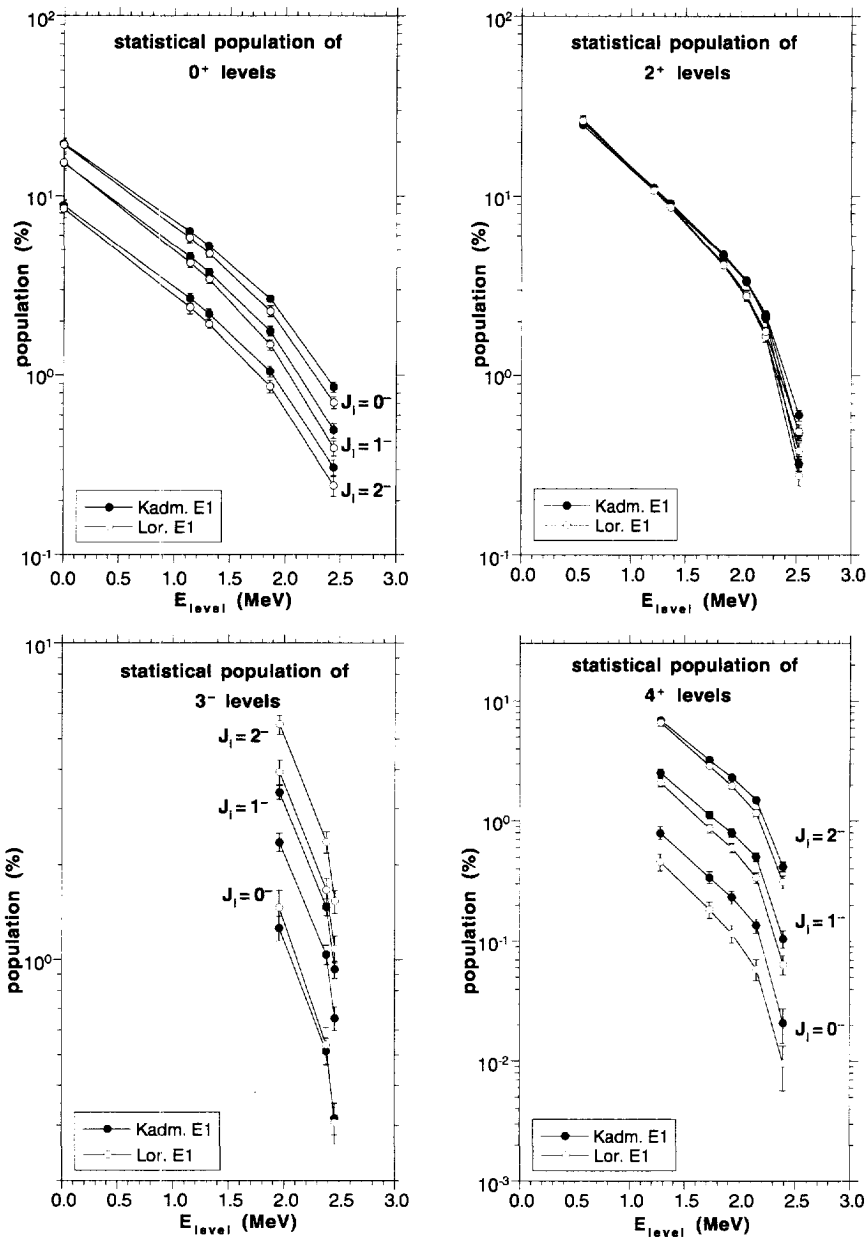

Figure 26: The populations of low-lying levels in ^{114}Cd of spin 0^+, 2^+, 3^- and 4^+ for the three resonance spins and for the Lorentzian and Kadmenskii photon strength functions.

calculated statistical populations of the discrete levels below 2.8 MeV are shown, then the intensities of the gamma-rays depopulating them, and finally the ratio of the intensities of specific gamma rays, in comparison with experimental data.

statistical populations of ^{114}Cd levels

The statistical populations of the discrete levels may depend on the parity of the resonance since a substantial part of it consists of feeding by one- and two-step cascades for which the parity dependence is still considerable. This is related to the difference in strength for various multipole radiations. A comparison of the simulated populations for resonances with the same spin but opposite parity showed that there is a noticeable parity dependence for the population of the $J = 0^+$ states only if the Lorentzian model for the $E1$ gamma strength function is used. When the Kadmenskii model is used, the parity dependence is negligible. The latter model favours $M1$ transitions and therefore the difference between $E1$ and $M1$ radiation strength is smaller which results in a decrease in the parity dependence of the statistical populations.

In figure 25 we show the simulated statistical populations of 0^+ and 4^+ states from s-wave resonances having spin and parity $J^\pi = 0^+$ and 1^+ and from p-wave resonances with $J^\pi = 0^-$ and 1^-. The backshifted Fermi gas model was employed for the level density and the Lorentzian and Kadmenskii models for the $E1$ strength. This figure illustrates the conclusion that the resonance parity does not substantially influence the statistical population except for the above mentioned case.

The populations due to the statistical decay to the low-lying levels are given for the three p-wave resonances as a function of the level energy in figure 26. We see a clear dependence on the resonance spin for the populations of the 0^+, 3^- and 4^+ states. The populations of these levels are split into three groups according to the spin of the initial resonance state. This is the case for both models used for the $E1$ photon strength function. This dependence on the resonance spin is expected because of the relatively large difference in spin between the initial and final state. In figure 26 the population of levels is shown for the two models of the photon strength function. For a given resonance spin group, a small difference between the two models is visible, except for the 3^- states, where the difference is large. However, for a given photon strength model, the splitting is apparent. This is also the case for the other combinations of models that we have used and for the two 3^+ states, not shown in the figure.

On the contrary, the 2^+ states are much less sensitive to the resonance spins, which is expected due to the smaller difference in spin. In fact, the first excited level at 558 keV is a 2^+ state, and its transition to the ground state is the most intense gamma ray (74% in thermal capture). The statistical population of this level is not dependent on the resonance spin but the feeding by other discrete levels makes the intensity of the gamma ray slightly spin dependent as can be seen in figure 27. Due to its large intensity, this gamma ray contributes very little to the error of a ratio in which it is present. To compare the simulated

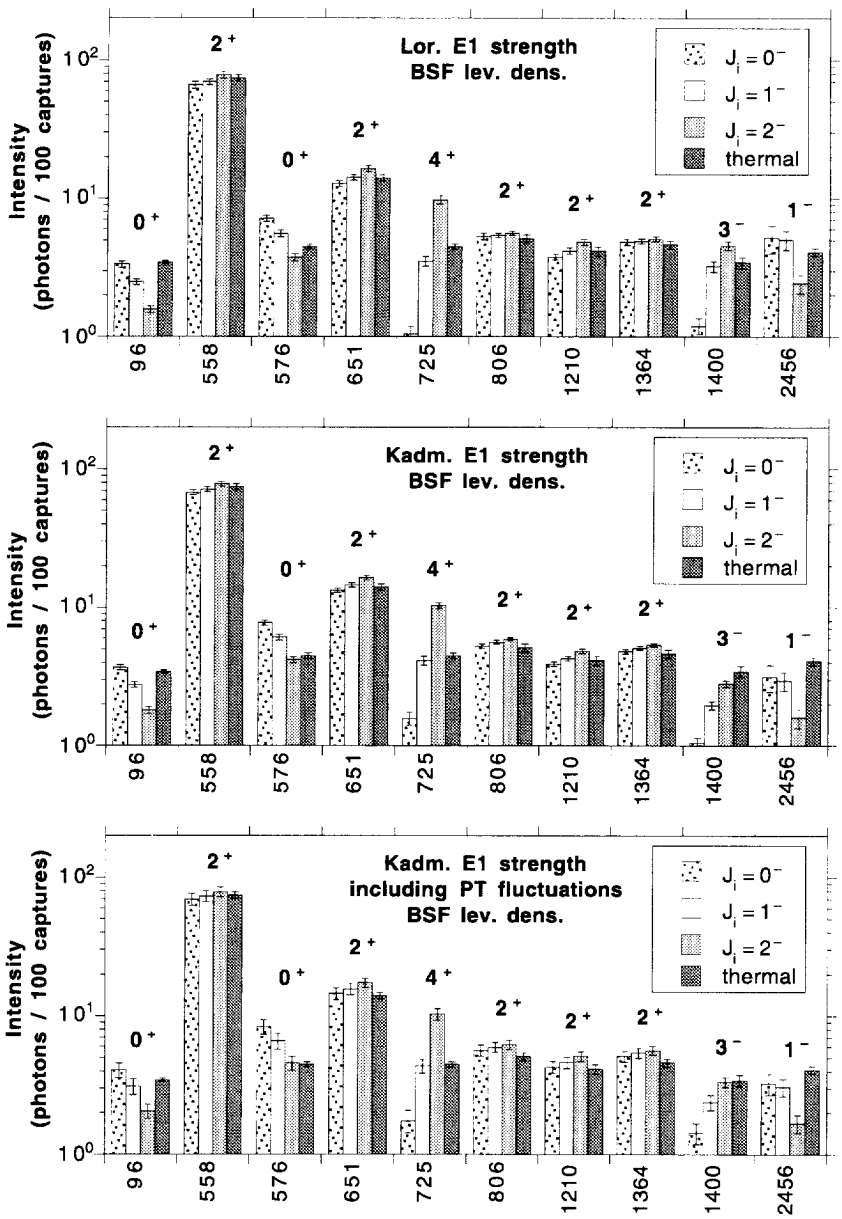

Figure 27: The intensities of selected gamma rays in ^{114}Cd with an intensity of more than 0.03 per captured neutron for the three spin groups for different models. The x-axis indicates the energy of the gamma rays.

populations with experimental capture gamma data, it is necessary to calculate the intensities of the gamma rays that depopulate the low-lying states.

gamma-ray intensities of ^{114}Cd

From the 99 gamma transitions coming from the decay between the low-lying states, only those showing a large enough intensity to be observed experimentally, are interesting. We consider therefore only the calculated gamma-ray transitions with an intensity of more than 0.03 photons per neutron capture. With this criterion we have selected 10 gamma rays, of which the calculated intensities are shown in figure 27 for several employed models. The gamma transitions that are most suited for a spin assignment experiment are those showing a large difference between the three spin groups and having a large enough intensity to be observed. But one should in fact also consider the absorption effects of the lower gamma rays and the decreasing detector efficiency for increasing gamma energy. For this reason, the large spin dependence of the gamma transitions of 96 keV, deexciting a 0^+ level and the gamma rays at 1400 and 2456 keV, deexciting a 3^- and a 1^- level respectively, are less suited for experimental spin determination. On the contrary, the gamma rays of 576 and 725 keV, coming from a 0^+ and a 4^+ level respectively, show a large effect and therefore seem to be very well suited. The intensity of the 96 keV gamma ray in thermal capture in figure 27 has been corrected for its internal conversion coefficient $\alpha = 1.76$ in order to make the value comparable with the simulated values.

Also, the employed models for level density and photon strength function affect the absolute intensities of the gamma rays while the relative intensity for a gamma ray originating from different resonance spins stays rather constant as illustrated by the three examples in figure 27.

comparison with experimental data of ^{114}Cd

In the spin assignment experiment it is more complicated to obtain absolute gamma-ray intensities expressed in photons per capture. To avoid this problem of normalization, the ratio of two gamma-ray intensities has been taken. It is shown that for the *p*-wave resonances the ratio between the gamma rays at 725 and at 558 keV split unambiguously into three groups, each one corresponding to a different spin. Also from the simulated data, the 725 keV line showed the largest spin effect. The 558 keV gamma ray, nearly not dependent on the resonance spin, can be considered proportional to the total capture rate and can be used as a normalization, making the ratio between the intensities of the 725 and the 558 keV line an indicator for the resonance spin.

As a consequence of the extreme statistical model, this ratio should, within a small variation due to Porter-Thomas fluctuations of the primary gamma-rays, be a constant for resonances with the same spin. The experimental ratio (see chapter 5) shows indeed three groups for the spins of the *p*-wave resonances 0^-, 1^- and 2^- and two groups for the *s*-wave resonances 0^+ and 1^+. Also, differences in the ratio have been observed for *s*- and *p*-wave resonances of the same spin. However, all these differences within a spin group are much

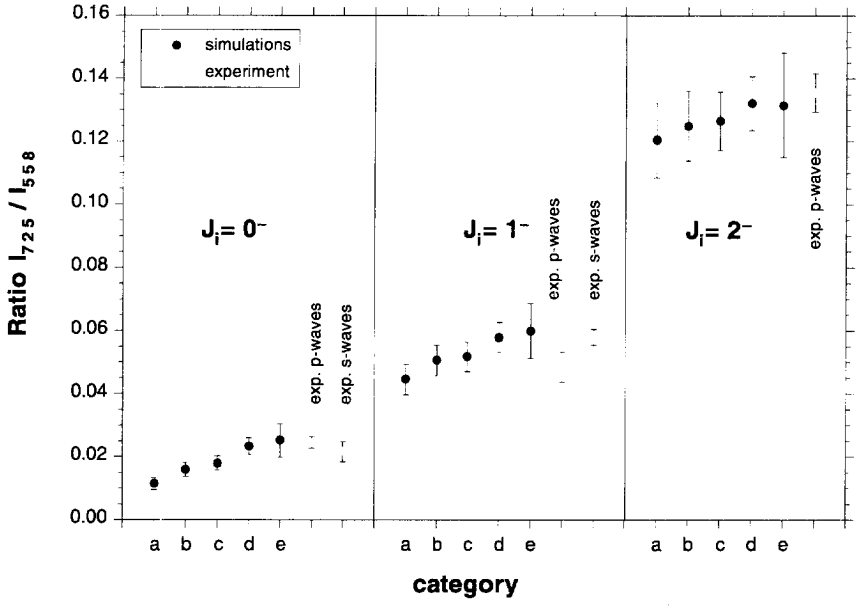

Figure 28: Comparison between experimental ratios and simulated values for ^{114}Cd. The employed models corresponding with each of the categories (a) through (e) are explained in the text and the numerical values are given in table 6.

smaller than the difference in the ratios between spin groups. In figure 28 these experimental values are compared with the simulated cases for several employed models. The numerical values for the various models are given in table 6. The used models for the photon strength are a Lorentzian with a fixed width (L) and the Kadmenskii model (K). For the level density we used the constant temperature model (CTF) and the backshifted Fermi

Table 6: The employed models and the numerical values for the simulations of the decay of ^{114}Cd.

category	employed models			Ratio $I_\gamma(725) / I_\gamma(558)$		
	*E*1	ρ	PT	$J_i^\pi = 0^-$	$J_i^\pi = 1^-$	$J_i^\pi = 2^-$
a	L	CTF	no	0.0114±0.0018	0.0446±0.0048	0.1205±0.0119
b	L	BSF	no	0.0159±0.0022	0.0507±0.0049	0.1249±0.0112
c	K	CTF	no	0.0180±0.0022	0.0518±0.0046	0.1265±0.0093
d	K	BSF	no	0.0233±0.0027	0.0580±0.0048	0.1321±0.0086
e	K	BSF	yes	0.0253±0.0053	0.0599±0.0087	0.1315±0.0166
exp. *p*-waves				0.0246±0.0018	0.0484±0.0048	0.1355±0.0062
exp. *s*-waves				0.0216±0.0055	0.0580±0.0025	

gas model (BSF). Also it is specified whether Porter-Thomas fluctuations (PT) are included or not. For the experimental values we have taken the weighted mean of the recently measured ratios [144], while the error bar indicates the spread among the resonances with the same spin and parity. In fact we have chosen only those well separated *p*-wave resonances that are not contaminated by nearby *s*-wave resonances. We see the excellent agreement between experiment and simulation. The error bars on the simulated ratios are due to the process of simulation using a finite number of events per nuclear realization. Therefore, the expectation values of the populations for a specific model are not achieved.

It is rather difficult to say which of the models are realistic approaches of the gamma decay in ^{114}Cd. The application of a normalization makes that differences in population, as seen in figure 26, become rather invisible in the ratio. On the other hand, this makes a prediction of experimental values independent on an exact knowledge of the models.

3.8. Concluding remarks

The intensities of the gamma rays, depopulating low-lying states that are fed by the decay of a highly excited nucleus after neutron capture in a resonance, are dependent on the spin of the resonance. Simulations of these gamma-ray intensities reproduce this resonance spin dependence and in addition give excellent qualitative agreement with experimental data, the several employed models giving slightly different results. For the ^{238}U(n,γ) simulations the spin splitting appears clearly but due to a lack of detailed knowledge of the discrete spectrum the calculated ratio of the specific gamma-ray intensities could not exactly be compared with the experimental results. In the case of ^{113}Cd(n,γ) simulations do not only reproduce this spin dependence but also the quantitative agreement with experiment is excellent.

Simulations of this type seem to be a powerful method to test the possibility of a spin assignment experiment with the low-level population method. Since such experiments are long-lasting, it is worthwhile to perform simulations beforehand in order to test the feasibility of the experiment. For the analysis of the gamma-ray spectra, the simulated gamma spectra can very well indicate those gamma transitions which are sensitive to the resonance spins.

The error in the statistical populations reflects the use of a finite number of events and the discretization of the statistical level region rather than that it has a physical meaning. Although the errors of the populations are not very large, due to the decay in the discrete level region and due to taking the ratio of two gamma-ray intensities, the error propagation causes quite considerable errors in the intensity ratio. One could decrease the error somewhat by calculating the decay of each event to the ground state instead of first calculating the statistical populations and then calculating their decay to the ground state, in this way

avoiding correlations due to the calculation in two steps. Hence also the spectra of the calculated gamma-ray multiplicity are calculated in a direct way.

It would also be interesting to calculate the spread in the intensities of specific gamma transitions within the ensemble of resonances with the same spin and parity. For this purpose one has to produce a "resonance realization", which is a set of nuclear realizations making an approach of a realistic nucleus. For each one of the nuclear realizations a sample of primary intensities, chosen from the Porter-Thomas distribution, should be kept fixed. For a new resonance realization, exactly the same set of nuclear realizations should be taken and only the primary gamma-ray intensities are replaced by another random sample.

Chapter 4

The spins of neutron *p*-wave resonances in ^{238}U(n,γ)

4.1. Introduction

The *p*-wave resonances of the 0^+ target nucleus ^{238}U can have $J^\pi = 1/2^-$ or $3/2^-$ while the *s*-wave resonances have $J^\pi = 1/2^+$. Only the $J = 1/2$ *p*-wave resonances can be admixed with *s*-wave resonances, while there is no admixing for the $J = 3/2$ *p*-wave resonances. By the time that PNC values for ^{238}U were measured, the spins of the *p*-wave resonances were not known and a maximum likelihood procedure with some additional assumptions has been applied to obtain the rms PNC matrix element M in which the data for *p*-wave resonances of both spins had to be used [49,50]. It is clear that if the spins were known, a more precise value could have been obtained. This will be discussed in chapter 6. To check the interpretation of the TRIPLE results [50] and to strengthen the conclusions of more precise measurements in the future, it is important to know the resonance spins.

The nucleus ^{238}U has been extensively studied and the energies and widths for the neutron *s*-wave and *p*-wave resonances in the energy region of interest, up to about 400 eV, are quite well known. In this chapter the experiment to determine the spins of the ^{238}U *p*-wave resonances is described. The results have been published [136-138].

4.2. Resonance spin assignment method

The method which we have applied to determine the *p*-wave resonance spins concerns the low-level population method. This technique has been described in section 1.2.4 on page 16 and has been proved to work very well with *s*-wave resonances. However, the strength of most *p*-waves in the low neutron energy range is very weak compared to that of *s*-waves, typically a factor 1000, so that the application of this method in the case of *p*-wave resonances is quite straightforward though experimentally much more difficult. An adventitious difficulty is the natural activity of ^{238}U apparent in the spectra together with the (n,γ) gamma rays.

The natural activity spectrum of ^{238}U is shown in figure 29 together with the spectrum of ^{232}Th. Both gamma-ray spectra were accumulated during 50 000 seconds with the sample

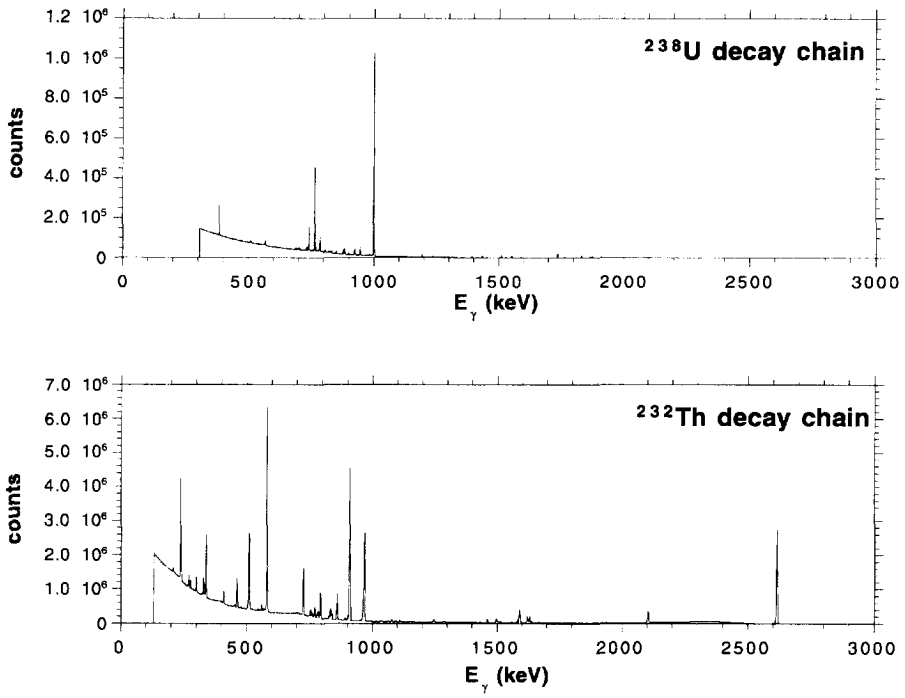

Figure 29: The natural activity spectrum of ^{238}U (upper) and ^{232}Th (lower) decay chain up to an energy of 3 MeV.

and detector in the same position as during the (n,γ) experiment. The uranium sample has a weight of 694 grams while the thorium sample weighs 443 grams. The figure shows that the gamma activity below 1 MeV of the decay chain of thorium, with an average count rate of 10 000 counts per second, is relatively large compared to that of uranium, with an average count rate of 1 500 counts per second. This natural activity appears as a background in the time-of-flight measurements. As also in thorium large PNC have been found, this is a candidate for resonance spin assignment. The large activity makes the application of the low-level population method to ^{232}Th very troublesome.

The level scheme of ^{239}U [133, 134] is very complicated; a simplified version, including all transitions with intensities larger than 5% in thermal neutron capture, is shown in figure 30. Several relatively strong gamma-ray transitions in the energy range of about 500 to 625 keV are available in the capture spectrum. This energy range is free from strong gamma transitions in the ^{238}U decay chain. These secondary gamma rays deexcite levels with spin 1/2, 3/2 and 5/2 and are suitable for determining resonance spins using the low-level population method. This has been verified by simulations described in chapter 3.

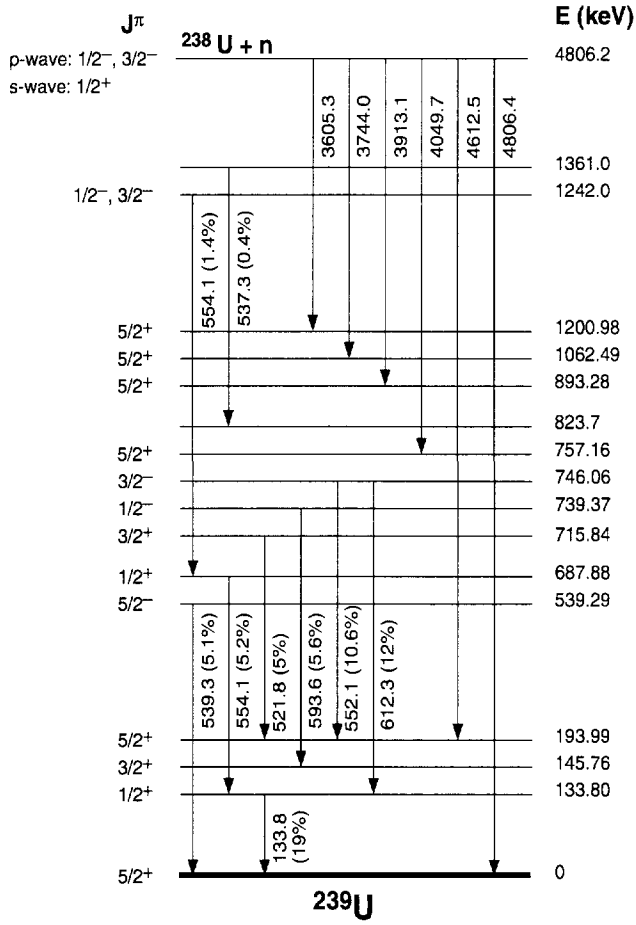

Figure 30: A simplified partial level scheme of ^{239}U showing the levels and transitions of interest for the spin assignment methods.

Additional information on the resonance spins was obtained by looking at primary transitions after neutron capture ending at $J^{\pi} = 5/2^{+}$ states. In fact, these transitions have $E1$ multipolarity for initial states with $J^{\pi} = 3/2^{-}$ and $M2$ multipolarity for a $J^{\pi} = 1/2^{-}$ resonance. In this second case the transitions are expected to be several orders of magnitude weaker and therefore not observable. In this way we can identify only $3/2^{-}$ states, because the absence of such transitions is not a guarantee for a $1/2^{-}$ state, due to the Porter-Thomas fluctuations of the gamma transitions.

In the low-energy part of the ^{239}U level scheme [133,134,139,140], many of the levels below 1 MeV have been assigned as Nilsson states, some of them combined with the β-vibration (0^+) or the γ-vibration (2^+) and all of them with several rotational excitations. As a consequence, many low-lying $5/2^+$ levels of ^{239}U are available. This improves the statistical probability to observe the $3/2^-$ resonances through primary transitions to $5/2^+$ states. The six low-lying states, including the ground state of ^{239}U, known as $J^\pi = 5/2^+$ levels from the literature, are also shown in figure 30.

4.3. Description of the experiment

The measurements were performed at the GELINA pulsed neutron facility using the time-of-flight technique. The Geel Linac and associated compressing magnet were operated to provide electron bursts of 100 MeV average energy and 1 ns width at a repetition frequency of 800 Hz and an average beam current of 60 μA. For the ^{238}U experiment the neutron beam was filtered by a natural B_4C sample of thickness 0.335 g/cm^2 to absorb slow neutrons. In addition, a 1 cm thick depleted uranium disc was placed in the neutron beam. Both filters were mounted between the concrete shielding of the linac and the wall of the flight station (see figure 13 on page 36). The latter filter served the double purpose of decreasing the intensity of the gamma flash as well as strongly reducing the count rate in *s*-wave resonances. Since the total cross section for the *s*-wave resonances in this energy region is much larger than that for the *p*-wave resonances, the transmission for neutrons with energies corresponding to *s*-waves is very much reduced. This technique of "self-indication" results in a dip in the observed peak of a strong resonance in the capture spectrum, as can be seen in the low-energy *s*-wave resonances in the TOF-spectrum in figure 32.

A 4 mm thick highly enriched ^{238}U metal disc (9 ppm ^{235}U) of 11.1 cm diameter and 694 g total weight, on loan from Oak Ridge National Laboratory, was used as target. Its thickness was 7.17 g / cm^2 or 0.0181 atoms / barn. The sample was placed at a 12.85 m flight distance. At this distance the unfiltered neutron flux $\Phi(E)$ is approximately

$$\Phi(E) = 7.0\times10^3 \cdot E^{-0.9} \quad \text{neutrons} / (\text{cm}^2 \cdot \text{s} \cdot \text{eV}) \,. \tag{73}$$

In order to avoid a substantial absorption of gamma rays, the sample has been positioned in such a way that the plane of the sample was making an angle of 60° with the neutron beam direction while the germanium detector was placed under an angle of 120°, as is shown in figure 31. The sample was viewed by a coaxial intrinsic germanium detector of 70% efficiency relative to the ^{60}Co gamma lines. In order to absorb neutrons scattered from the sample, a considerable amount of shielding was used. Details can be found in section 2.3 on page 35.

For each event, the amplitude (ADC) information, measured for the gamma energy range 0.3-5 MeV, and the time-of-flight (TOF) information, digitized into bins with a width of

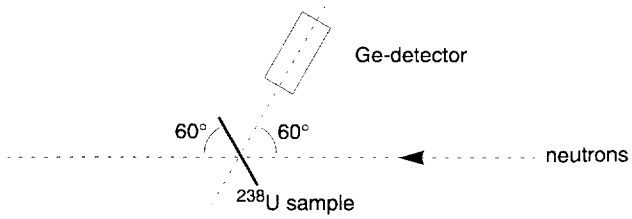

Figure 31: Schematic layout of the sample and detector with respect to the neutron beam for the ^{238}U experiment.

32 up to 256 ns, were recorded in listing mode. The sorting of the listmode data provided the gamma-ray spectra of 79 different TOF-intervals.

4.4. Data analysis

The TOF-spectrum, obtained with the total number of gamma-ray pulses in the energy range 0.3-5 MeV, is plotted versus the neutron energy in figure 32 on a logarithmic scale in order to make the small *p*-wave resonances more clearly visible. One should note the absence of any isotopic structure other than due to $^{238}U(n,\gamma)$, thanks to the extremely low content of ^{235}U in the sample (9 ppm) and to the efficient absorption of scattered neutrons. The arrows indicate the position of the *s*- and *p*-wave resonances. At the higher energies in this figure the resonances start to overlap seriously.

Only one resonance that is known not to be from ^{238}U is present in this TOF spectrum. The resonance at 11.9 eV could be identified as an *s*-wave resonance of ^{195}Pt due to the characteristic gamma rays of 333 and 358 keV of the spectrum of ^{196}Pt. The amount could be roughly estimated to be due to about 90 ppm natural Pt. Probably this impurity has been introduced into the sample during its preparation in a Pt crucible.

A comparison with a previous measurement using a sample containing much more ^{235}U (2000 ppm), shows that a small resonance at 57.9 eV, listed as a ^{238}U *p*-wave resonance in ref. [63], is in fact belonging to ^{235}U. In figure 33 a part of the time-of-flight spectrum in the vicinity of 57.9 eV is shown for the 9 ppm sample and the 2000 ppm sample. The structure at 57.9 eV is not present or much weaker in the measurement with the very pure ^{238}U sample, so justifying the assumption that it is due to ^{235}U.

On the whole, we sorted out 79 gamma-ray spectra of 8192 channels corresponding to as many TOF intervals, each one being associated with an *s*-wave resonance, a *p*-wave resonance or a "background" region in between resonances. In order to obtain the pure capture yield of a given resonance, the gamma-spectrum corresponding to one or more nearby background regions was subtracted from the raw data after proper normalization. For

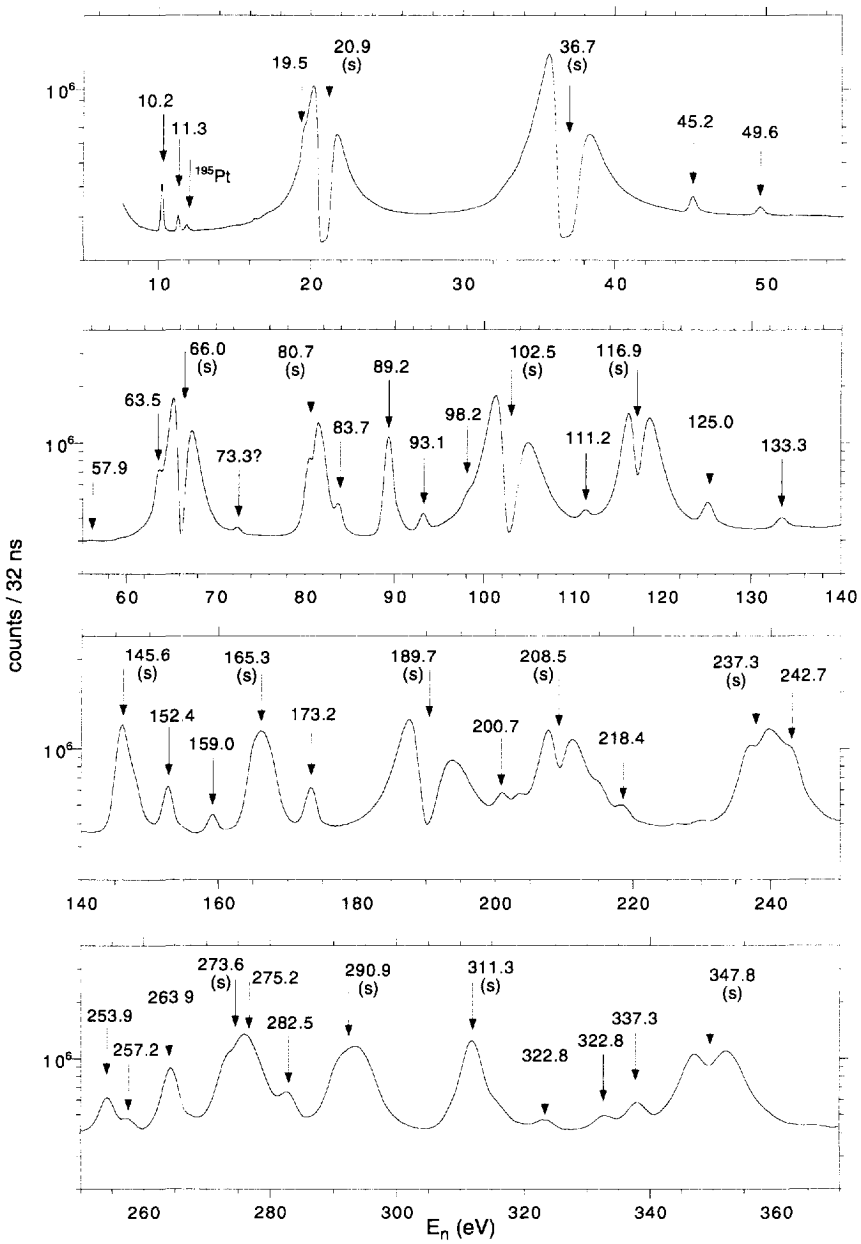

Figure 32: The TOF spectrum for $^{238}U(n,\gamma)^{239}U$ on a logarithmic scale with the resonance energies indicated. The *s*-wave resonances are distinguished with (s).

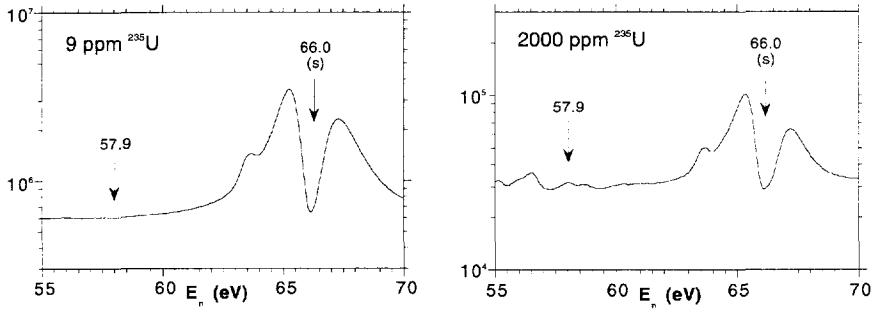

Figure 33: Comparison of the actual measurement with a 9 ppm ^{235}U sample with a previous measurement with a 2000 ppm ^{235}U sample, providing evidence that the 57.9 eV resonance is not belonging to ^{238}U but to ^{235}U.

some *p*-wave resonances which are located on the shoulder of a nearby *s*-wave resonance, the yield was fitted with the program REFIT [81]. The fraction of *s*-wave capture in the given TOF-interval was determined whereafter the appropriate *s*-wave spectrum was subtracted. In this way the gamma-ray spectrum corresponding only to the *p*-wave resonance can be derived. This procedure was applied to the *p*-wave resonances at 63.52, 83.68, 98.20, 124.97, 242.73 and 351.86 eV.

The FWHM of gamma-ray peaks is not only a function of the gamma-ray energy but also of the time-of-flight. This effect is due to the electronic signal handling in response of the

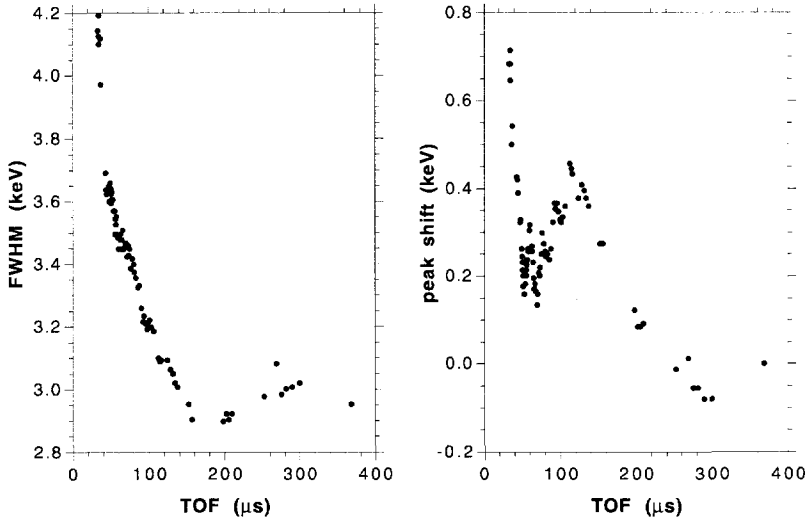

Figure 34: The FWHM and shift in the position of the 1001 keV gamma ray of natural ^{238}U as a function of the time-of-flight.

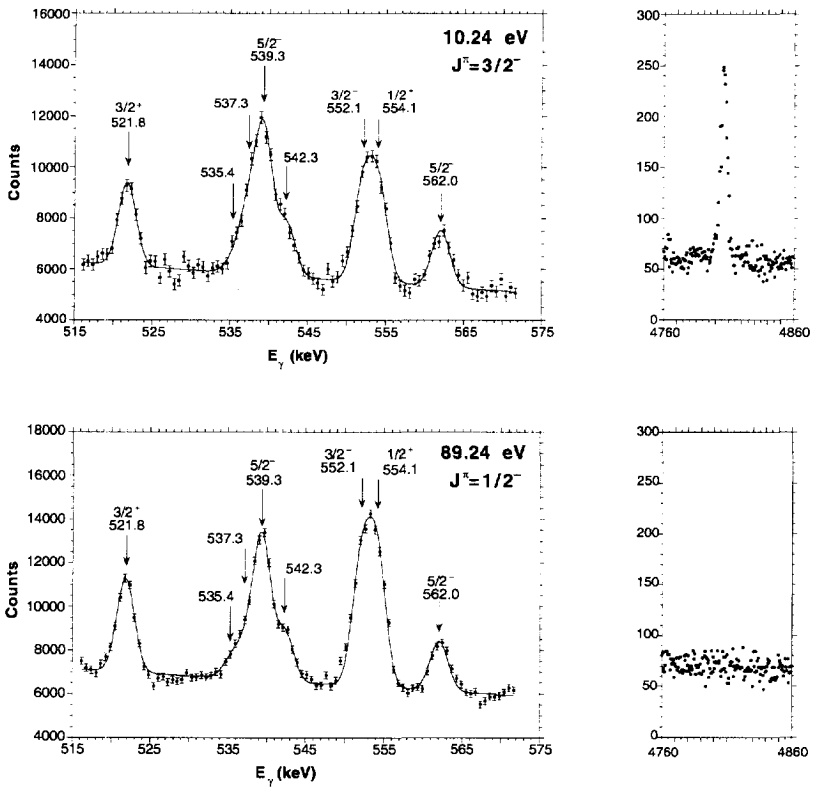

Figure 35: Two examples of a fit of the capture gamma-ray spectrum in the 515-575 keV energy range for two *p*-waves of different spin. On the right is shown the region around the 4806 keV transition to the $5/2^+$ ground state, observed only in the $J = 3/2$ resonance.

gamma flash. In the same way also the position of the gamma-ray peaks change as a function of the flight time. The natural activity of the ^{238}U decay chain provides a means to determine these variations since these gamma rays are independent from the time-of-flight. In figure 34 the FWHM and the shift in the position of the 1001 keV natural gamma ray is plotted as a function of the flight time.

For the gamma-ray spectra an accurate energy calibration as well as a determination of the FWHM of the peaks was obtained from nearby resolved peaks belonging to spectra with high counting statistics, typically *s*-wave resonances. Then both peak positions as well as their widths were kept fixed in the fitting of the gamma-ray spectra of the *p*-wave resonances. The gamma-ray peaks have been fitted with a standard Gaussian peak shape. The width of the channels of the gamma-ray spectra was approximately 0.6 keV per channel.

4.5. Results from low-energy gamma rays

Sections of the spectra of the two most intense p-wave resonances at 10.24 eV and 89.24 eV are shown in figure 35. The data in the region 515-575 keV are fitted with eight known transitions. At the top of each peak the energy and the spin and parity of the deexcited state, taken from the literature, are shown. Since the effective FWHM resolution at these lines is about 2.7 keV, it is not possible to resolve all transitions. One may notice that in the upper part of figure 35 the doublet dominated by the 539 keV line, from a $J^{\pi} = 5/2^{-}$ state, is higher than the multiplet at 552-554 keV, deexciting states with $J^{\pi} = 1/2^{+}, 3/2^{-}$. In the lower part it is the opposite. Because it is clear from section 1.2.4 on page 16 that a 5/2 state is populated more by a 3/2 capture state than by a 1/2 state, we assigned $J^{\pi} = 3/2^{-}$ to the 10.24 eV resonance and $J^{\pi} = 1/2^{-}$ to the 89.24 eV resonance.

Table 7: Values of the ratio $R = (I_{537} + I_{539}) / (I_{552} + I_{554})$ for 17 ^{238}U s-wave and 14 p-wave resonances.

s-waves E_0 (eV)	ratio R	p-waves E_0 (eV)	ratio R
20.9	0.464±0.008	10.24	0.749±0.028
36.7	0.480±0.008	11.31	0.571±0.059
66.0	0.540±0.008	45.17	0.672±0.069
80.7	0.523±0.012	63.52	0.621±0.020
102.5	0.494±0.010	83.68	0.527±0.036
116.9	0.593±0.014	89.24	0.560±0.012
145.6	0.534±0.017	93.14	0.619±0.077
165.3	0.555±0.019	124.97	0.785±0.069
189.7	0.578±0.027	152.42	0.770±0.042
208.5	0.457±0.015	158.98	0.830±0.111
237.3	0.464±0.018	173.18	0.599±0.038
273.6	0.682±0.027	242.73	0.553±0.020
290.9	0.445±0.021	253.90	0.715±0.059
311.3	0.557±0.033	263.94	0.878±0.035
347.8	0.561±0.043		
376.9	0.492±0.037		
434.0	0.598±0.051		

More quantitatively, we computed the ratio R of the intensities of the two doublets $R = (I_{537} + I_{539}) / (I_{552} + I_{554})$ for those resonances having sufficient statistics. In fact, also the gamma ray at 554 keV is a doublet as can be seen from figure 30. In table 7 the values of this ratio is given for 17 s-wave and 14 p-wave resonances. In figure 36 the ratios are plotted as a function of the resonance energy for both the s-wave and the p-wave resonances. This figure shows a splitting of the ratios into two groups for the p-wave reso-

nances. The weighted averages of the ratios for each group are shown by the two horizontal lines which can be associated to the J = 1/2 and 3/2 p-wave resonances. For the s-wave resonances, all having spin J = 1/2, there is not such a splitting, as is expected. The ratios for these $1/2^+$ s-wave resonances are slightly lower than those for the $1/2^-$ p-wave resonances, suggesting a small parity dependence, but considerably below the values of the

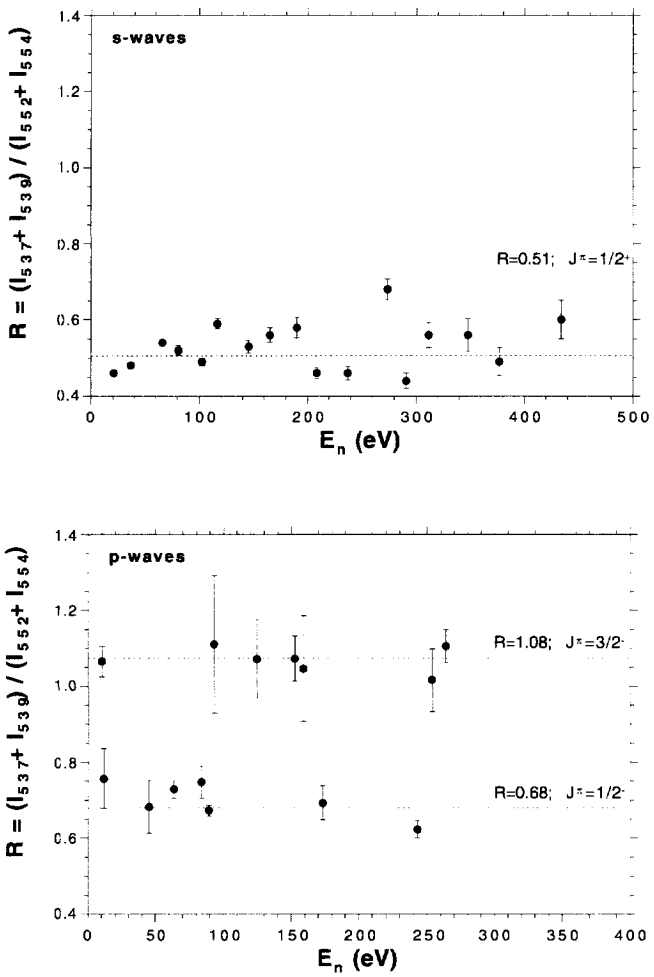

Figure 36: The ratios R between the sums of the intensities of the indicated gamma lines plotted versus the energy for 17 s-wave (upper) and 14 p-wave resonances (lower).

$3/2^-$ p-wave resonances. The large difference between the ratios for the spin 1/2 and spin 3/2 resonances is in accordance with the model simulations discussed in chapter 3.

4.6. Results from high-energy gamma rays

High-energy gamma-ray spectra were also investigated in p-wave resonances and four primary transitions at 4806.4, 4612.5, 4049.7 and 3744.0 keV, leading to $J^\pi = 5/2^+$ states, were observed in some of them. One can derive the approximate relative intensities of the primary gamma rays by assuming that the experimentally measured resonance capture area is proportional to the capture cross section. This assumption is justified because the gamma energy range covers the whole spectrum except for the first 300 keV and because the sample is thin. Thus the area of a primary gamma ray divided by the total number of counts in the resonance is in good approximation proportional to the intensity. To obtain the absolute intensities one can find the normalization constant using well known intensities from the literature. The areas of the mentioned peaks were fitted and the corresponding intensities normalized to those given in ref. [141] for the 20.87 eV s-wave resonance. A list of these intensities, in units of photons per 100 neutrons captured, is given in table 8 for nine p-wave resonances which were on this basis assigned as $J = 3/2$ p-wave resonances. For two resonances which were not corrected for the strong contamination of s-wave capture, we give only a lower limit of the intensities. On the right hand side of figure 35 the 4806.4 keV transition to the $5/2^+$ ground state for the 10.24 eV p-wave resonance is shown. This transition is not visible in the case of the 89.24 eV p-wave resonance.

Table 8: Experimental intensities, in photons per 100 neutron captures, of primary gamma-ray transitions leading to $J^\pi = 5/2^+$ states.

E_γ	E_n(eV)								
(keV)	**10.24**	**19.53**	**93.14**	**98.20**	**253.9**	**263.9**	**282.5**	**351.9**	**439.7**
4806.4	0.41 ± 0.08	>0.45			1.63 ± 0.33	1.34 ± 0.25	1.81 ± 0.33	5.44 ± 0.93	>0.89
4612.5				2.19 ± 0.45	3.60 ± 0.65	0.81 ± 0.18	1.68 ± 0.33	2.65 ± 0.59	>0.71
4049.7		>0.70	0.61 ± 0.15						
3744.0	0.19 ± 0.04								

In figure 37 the high-energy gamma-ray spectra without background correction are shown for the nine resonances listed in table 8. The spectra of the resonances at 19.53 and at 439.7 eV contain a large part of the gamma rays of nearby s-wave resonances. The lines indicated with arrows are transitions to $5/2^+$ states. The admixing of s-wave spectra does

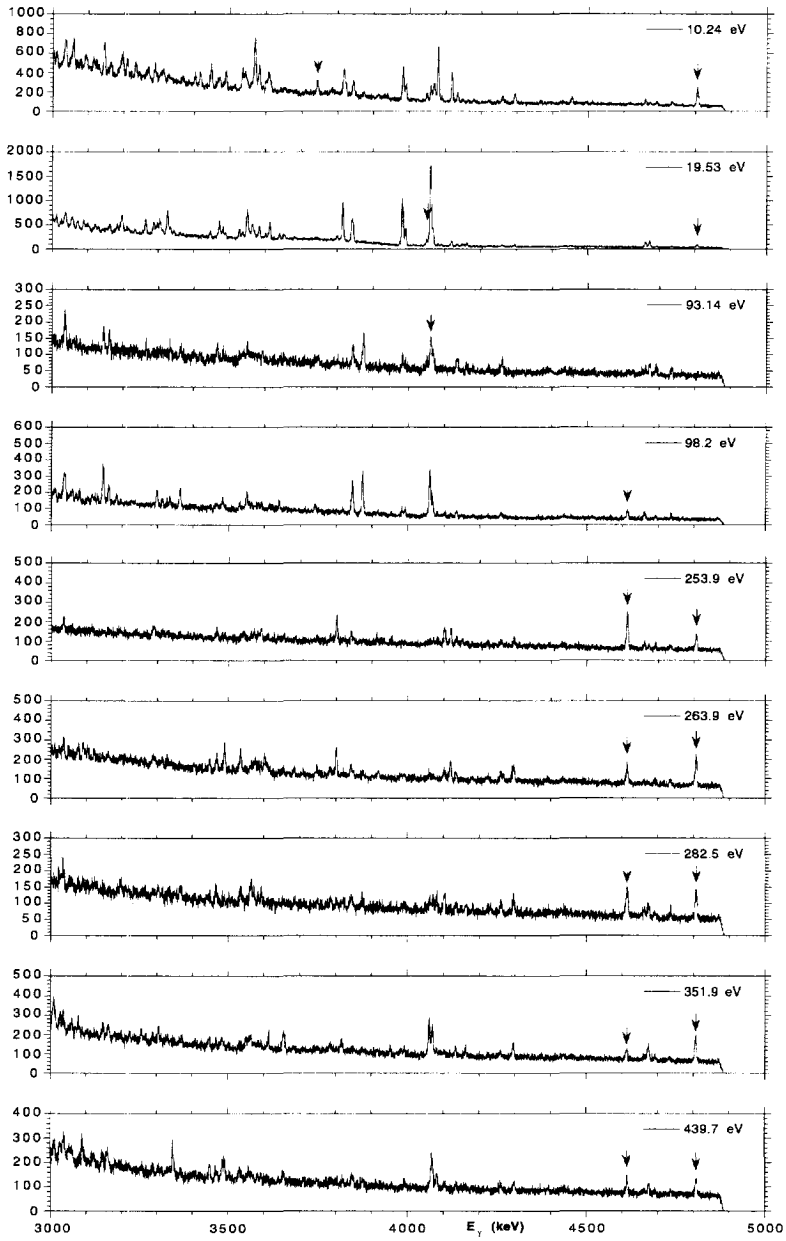

Figure 37: The high-energy gamma-ray spectra for 9 ^{238}U *p*-wave resonances showing a primary transition to a $5/2^+$ state and therefore indicating a $3/2^-$ resonance spin.

not influence the conclusions because in the case of an s-wave resonance, these transitions have $E2$ character and their contribution can therefore be neglected.

4.7. Concluding remarks

The results of the spin determinations are summarized in table 7. The assignments based on both the low-level population method and on information from primary transitions are shown and are in complete agreement with each other. The assigned p-wave resonances contain all the p-wave resonances of which PNC effects have been measured [50]. The knowledge of these p-wave resonance spins allows to make a more accurate estimate of the root-mean-square PNC matrix element. This will be treated in chapter 6.

Table 9: List of the present spin assignments for 19 ^{238}U p-waves.

E_0 (eV)	low level population	primary transitions	adopted
10.24	3/2	3/2	3/2
11.31	1/2		1/2
19.53		3/2	3/2
45.17	1/2		1/2
63.52	1/2		1/2
83.68	1/2		1/2
89.24	1/2		1/2
93.14	3/2	3/2	3/2
98.20		3/2	3/2
124.97	3/2		3/2
152.42	3/2		3/2
158.98	3/2		3/2
173.18	1/2		1/2
242.73	1/2		1/2
253.90	3/2	3/2	3/2
263.94	3/2	3/2	3/2
282.46		3/2	3/2
351.86		3/2	3/2
439.75		3/2	3/2

The present spin assignments can be used to derive the average level spacing of the J = 1/2 p-wave resonances. Taking the seven J^{π} = 1/2$^-$ resonances between 11.31 and

242.73 eV, we can calculate the average spacing $D_{1,J=1/2} \approx 39$ eV. This should be compared with the average spacing of s-wave resonances $D_0 \approx 21$ eV given in ref. [63].

Chapter 5

The spins of neutron *s*- and *p*-wave resonances in ^{113}Cd(n,γ)

5.1. Introduction

After the detection of PNC in a large number of *p*-wave resonances of ^{238}U [49,50] and in ^{232}Th [51], nuclei near the mass region $A = 100$ have been investigated by the TRIPLE group. One of these nuclei is ^{113}Cd [31]. The helicity dependence of the absorption cross section of this nucleus was studied using a capture gamma-ray detector, in contrast with the ^{238}U and ^{232}Th experiments, in which the helicity dependence of the total cross section was measured using a neutron detector in a transmission experiment.

The situation in ^{113}Cd is also different in the way that both ^{238}U and ^{232}Th have a ground state spin and parity $J^{\pi} = 0^{+}$, giving rise to *s*-waves with $J^{\pi} = 1/2^{+}$ which admix into the $1/2^{-}$ *p*-waves. Neutron capture in the even-odd nucleus ^{113}Cd with ground state spin and parity $J^{\pi} = 1/2^{+}$ gives rise to *s*-wave resonances with $J^{\pi} = 0^{+}$ or 1^{+} and *p*-wave resonances having spin and parity 0^{-}, 1^{-}or 2^{-}. Parity nonconservation may occur at the 0^{-} and 1^{-} *p*-wave resonances and is related to the $j = 1/2$ parts of their total neutron widths in experiments with polarized beams and unpolarized targets. For 0^{-} resonances this is equal to the total neutron width but for the 1^{-} resonances the $j = 1/2$ parts are unknown fractions of the neutron widths. For a complete analysis in fact not only the *p*-wave resonance spins but also the channel spin fractions must be known [41]. Because in the case of ^{113}Cd the *s*-wave resonances have two possible spins, it is not only important to know the *p*-wave resonance spins but it is also necessary to know the spins of the *s*-wave resonances of ^{113}Cd in order to be able to analyse the PNC-effects.

Also for historical reasons ^{113}Cd is interesting because it was this nucleus where Abov *et al.* discovered for the first time parity nonconservation in the neutron-nucleus system [21]. The Dubna group thereafter investigated PNC in the ^{113}Cd *p*-wave resonances at 7 and 22 eV [142] and found considerable PNC effects in the 7 eV resonance.

In fact, the *s*-wave resonances of ^{113}Cd in the epithermal energy region are quite well known and even some of the *s*-wave spins are already known from the literature [63]. Information about the *p*-wave resonances was not yet available until recently, Frankle

et al. [143] identified 23 p-wave resonances in the neutron energy range up to 500 eV. In this chapter we will discuss the experiments that have lead to the spin assignments of 23 s-wave and 21 p-wave resonances. The results have been published [138,144].

5.2. Resonance spin assignment method

Also in this experiment we have applied the low-level population spin assignment method to determine the spin of the neutron s- and p-wave resonances. The relative populations of the excited states are determined by measuring the intensities of gamma transitions deexciting them. In order to increase the spin effect and also to avoid any problem of normalization to the total neutron capture rate in the individual resonances, it is convenient to measure the intensity ratio of two transitions depopulating levels of different spin. Usually, the larger the spin difference, the larger the effect. The transitions to be chosen should conform to this rule and at the same time should be strong enough to be observed in most p-wave resonances.

The structure of ^{114}Cd is quite well known [135,145,146] and its level structure, which resembles to some extent a vibrational character, is adequately understood [147]. A simplified partial level scheme of ^{114}Cd is shown in figure 38. The gamma-ray and level energies are taken from ref. [135] for low energy and from ref. [146] for high energy primaries when available. Several gamma rays with an intensity of more than 4% in thermal capture are present in the energy range between 500-1000 keV with initial levels having spin and parity 0^+, 2^+ and 4^+. The explicitly indicated transitions in figure 38 are the most prominent ones and as such good candidates for the spin assignment method. Especially the gamma rays of 576 and 725 keV, deexciting a 0^+ and a 4^+ state respectively, exhibit a large spin dependence according to the simulations described in chapter 3 as well as confirmed by this experiment.

Also shown in figure 38 are high-energy primary gamma rays which can give useful information about the spin in the case of a p-wave resonance. A primary transition to a 0^+ state indicates an $E1$ transition from a 1^- resonance state. Transitions to 0^+ states from 0^- resonances are forbidden and those from 2^- initial states have $M2$ multipolarity, which is several orders of magnitude weaker than an $E1$ transition. However, the absence of strong transitions to 0^+ states does not rule out the possibility of an initial 1^- state due to the Porter-Thomas fluctuations, which can reduce the intensity of $E1$ transitions significantly, making its detection impossible in practise. Similarly, a strong transition to a 3^+ state must be an $E1$ transition coming from an initial 2^- resonance state. For 0^- resonances, there are no such indicative transitions. In total five primary transitions to 0^+ states and two to 3^+ states are known and are indicated in figure 38.

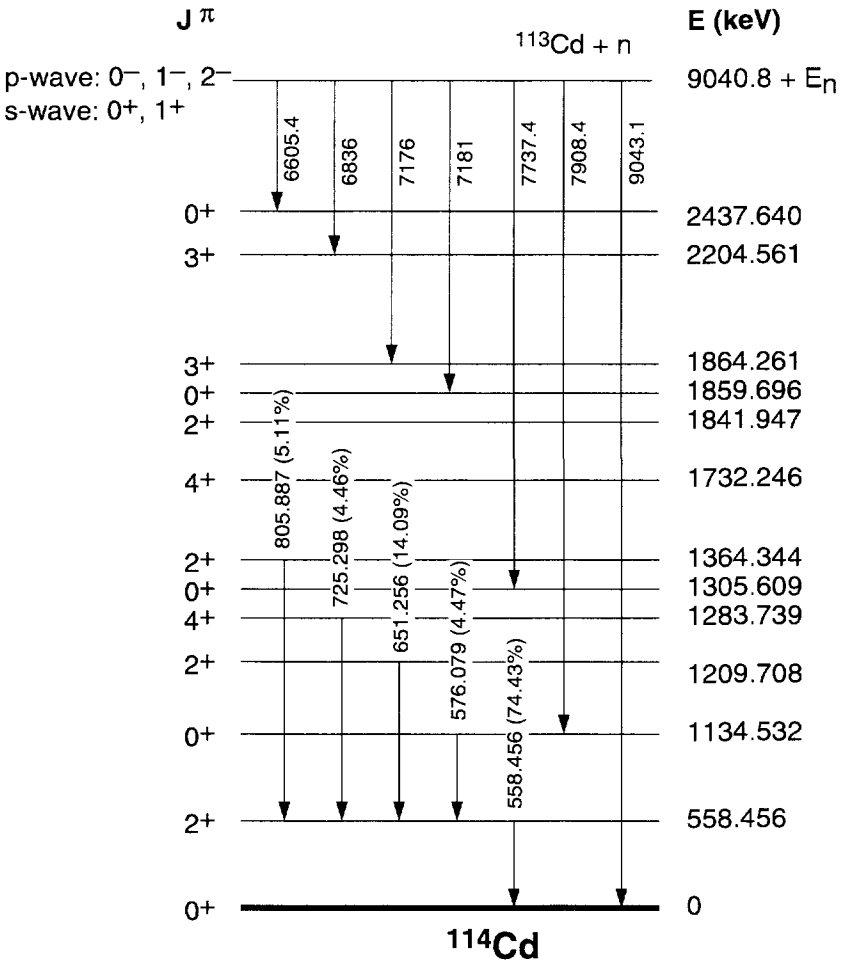

Figure 38: A simplified level scheme of ^{114}Cd showing the levels and transitions of interest for the spin assignment method. The gamma-ray energies are taken from ref. [135] for low energy and from ref. [146] for high energy transitions. The level energies are from ref. [135].

5.3. Description of the experiment

The linac was operating at similar conditions as during the ^{238}U experiment described in chapter 4. In order to absorb slow neutrons, a filter of natural B_4C of 0.335 g/cm^2 thick-

ness was used. Also a 1 cm thick lead disc was placed in the beam in order to decrease the intensity of the gamma-flash. However, the count rate in the *s*-wave resonances was not reduced as in the uranium experiment. Since ^{113}Cd is a stable isotope there is no additional background radiation. Therefore, a larger activity due to *s*-wave capture from the sample, which was also smaller compared to the ^{238}U sample, could be accepted.

We used a highly enriched ^{113}Cd metal disc (93.35%) of 90 mm diameter, about 1.65 mm thick and a total weight of 91.2 g. The sample was obtained from the Russian State Pool of Isotopes via the Joint Institute of Nuclear Research in Dubna. The thickness of the sample was 1.434 g/cm^2 or 0.00764 atoms/barn. The isotopic abundance and the chemical composition have been analysed in the originating institute and the results are shown in table 10.

Table 10: Isotopic and chemical composition of the enriched Cd sample

Cd isotope	contents (%)	element	contents (%)
106	<0.010	Fe	<0.003
108	<0.010	Al	<0.004
110	0.138	Si	<0.004
111	0.264	Cr	<0.001
112	2.930	Ni	<0.001
113	93.350 ± 0.090	Cu	0.006
114	3.110	Pb	<0.0005
116	0.208	Sb	0.003
		Sn	<0.0005
		Zn	0.008

The sample was placed at a 12.85 m flight distance, perpendicular to the neutron beam and was viewed by two coaxial intrinsic germanium detectors of 70% efficiency, both placed at opposite sides of the sample perpendicular to the neutron beam, as is schematically shown in figure 39. The whole assembly was shielded with lead and paraffin as described in paragraph 2.3.1 on page 35.

The amplitude information from the two germanium detectors was processed with two 8k fast ADCs for the gamma energy range 0.3-9 MeV, in coincidence with the time-of-flight (TOF) information, measured with a 25 bit multiple shot time digitizer. The converted values of the ADCs were merged together resulting in a 16k ADC value. The events were recorded in listmode on the 1 Gbyte hard disk of the PC-based data acquisition system. The listmode data were stored on an Exabyte tape unit. In total an amount of 20 Gbyte of raw data was collected during 700 hours of effective beam time.

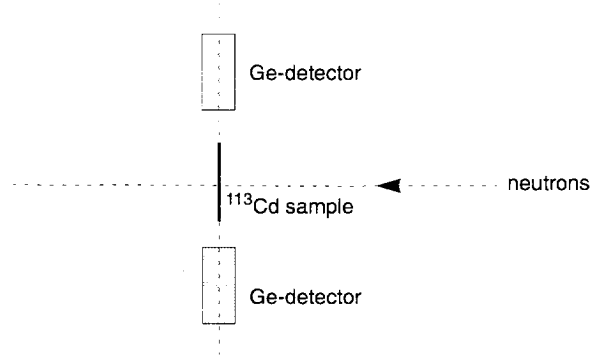

Figure 39: Schematic layout of the sample and the detectors with respect to the neutron beam for the ^{113}Cd experiment.

5.4. Data analysis

The total number of gamma-ray pulses corresponding to $0.3 < E_\gamma < 9.0$ MeV and collected in 32 ns wide TOF channels, is plotted versus neutron energy in figure 40 on a logarithmic scale to show the *p*-wave resonances more clearly. In a first analysis we have sorted out about 150 8k gamma-ray spectra corresponding to TOF intervals associated with resonances and "background" regions in between resonances for both detectors.

Several weak peaks were observed in the TOF spectrum of which some were not mentioned in ref. [63]. Characteristic gamma rays made clear that some of these structures were belonging to other Cd isotopes. Resonances of the even-odd nucleus ^{111}Cd could be distinguished by their 617 keV gamma-ray, while resonances from the even-even isotopes ^{110}Cd, ^{112}Cd and ^{114}Cd were identified by means of characteristic gamma rays in the energy range 300-500 keV.

When a small resonance was not from a Cd isotope other than ^{113}Cd, and not recognized as an impurity, then it was believed to be a new *p*-wave resonance since the ^{113}Cd sample is very pure. This was the case for small peaks at 33, 125, 146, 178, 203, 299, 312, 351, 385, and 422 eV. The resonance at 312 eV coincides with a listed *s*-wave resonance of ^{111}Cd, but the gamma ray spectrum is dominated by lines from ^{113}Cd so there is certainly a *p*-wave resonance of ^{113}Cd at this energy.

Conversely, we did not observe evidence for resonances at 106.1, 194.8 and 210.9 eV, mentioned in ref. [143], but it should be noted that these resonances fall on tails of strong *s*-wave resonances. The peaks at 125 and 146 eV were already mentioned in ref. [63] as unassigned resonances of Cd. From the peaks above 500 eV, we determined the spins of

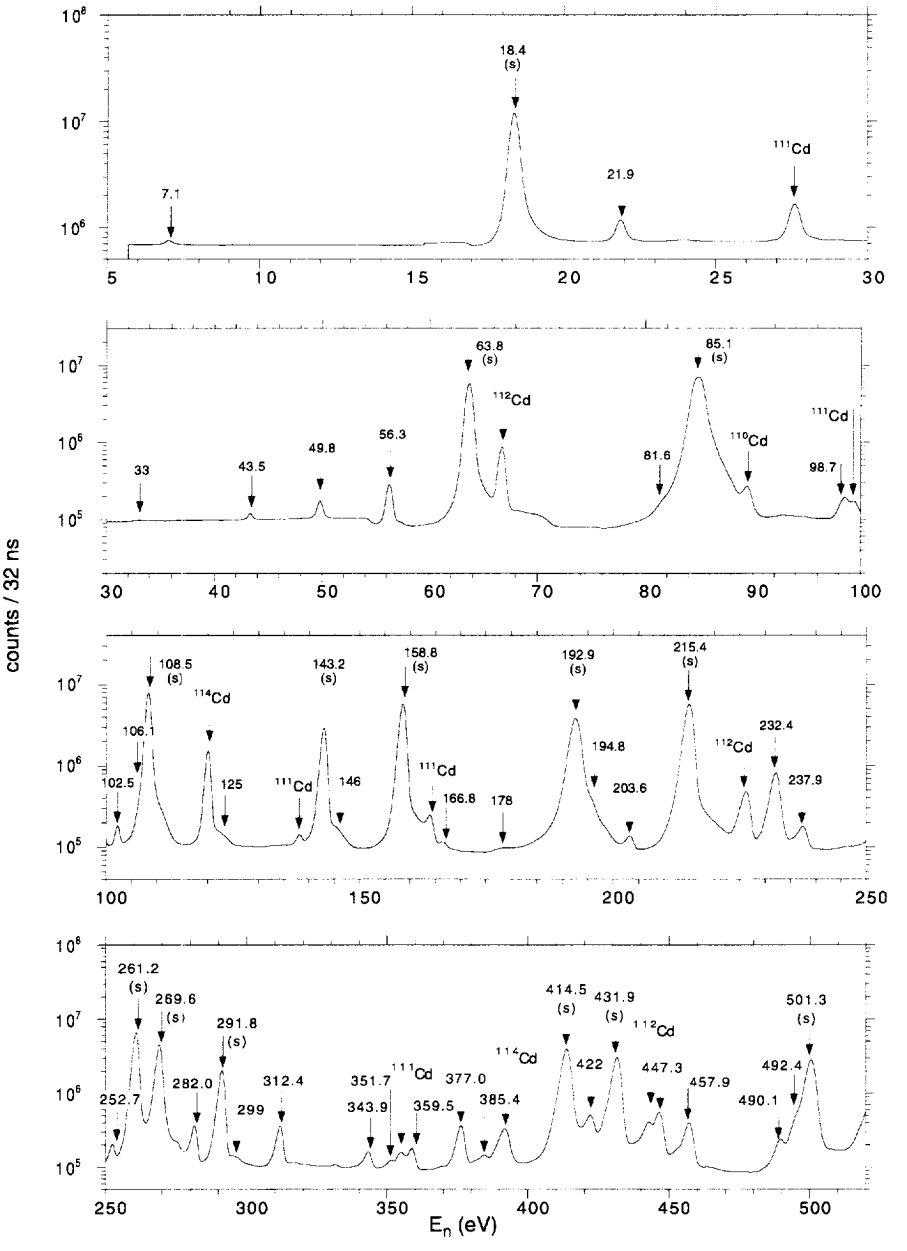

Figure 40: The TOF spectrum for $^{113}Cd(n,\gamma)^{114}Cd$ on a logarithmic scale with the *s*- and *p*-wave resonances indicated. Also some *s*-wave resonances of other Cd isotopes are visible.

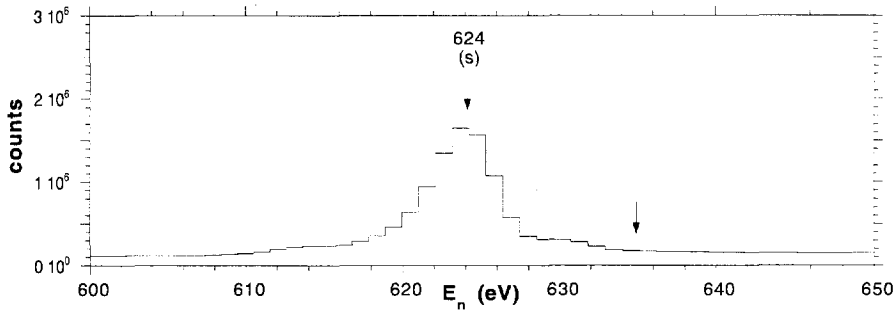

Figure 41: Part of the time-of-flight spectrum around 600 eV. An *s*-wave resonance is located at 624 eV while no evidence for a resonance at 634.9 eV [63] is found.

the resonances listed in ref. [63], assuming them to be *s*-wave resonances because of their large neutron widths. We found no evidence for an *s*-wave resonance in ^{113}Cd at 634.9 eV, as mentioned in ref. [63], but a nearby large *s*-wave resonance is located at 624 eV, as is shown in figure 41. This resonance is related to ^{113}Cd since the characteristic secondary ^{114}Cd gamma transitions are observed.

The gamma-ray spectra corresponding to the resonance regions have been corrected for the background influence. The areas of several peaks of interest have been fitted with both a symmetric Gaussian peak shape and with an asymmetric peak shape for the two detectors. Low-energy capture gamma-ray spectra in the 525-850 keV region are plotted on a logarithmic scale in figure 42 for three *p*-wave resonances of different spin. The energies of the five transitions quoted in figure 38 and the J^{π} values of the corresponding deexcited states are given above each peak. The intensity of the strong 558 keV transition depopulating the first excited (2^+) state, which is presumably little affected by the initial spin value, can be considered in first approximation as a measure of the number of neutrons captured in a given resonance. Compared to that, the intensity of the 725 keV transition, from a 4^+ level, shows an increase with the resonance spin. On the contrary, the 576 keV line, from a 0^+ level, decreases with increasing value of the spin of the resonance state. This behaviour is in agreement with the basic assumption of the present spin assignment method, namely that the population of a given low-lying state increases when the difference between its spin and that of the resonance decreases. The corresponding spectra for the 0^+ and 1^+ *s*-waves are very similar to those of the 0^- and 1^- *p*-waves.

5.5. Results from low-energy gamma rays

Several possible ratios of the intensities of gamma rays have been calculated for each group of resonances. We have tried the ratios of gamma rays depopulating states with different spin, notably those of 576, 651, 725, 806 and 1400 keV. In the case of *s*-wave resonances, due to the good statistics the values of each ratio split up clearly into two groups

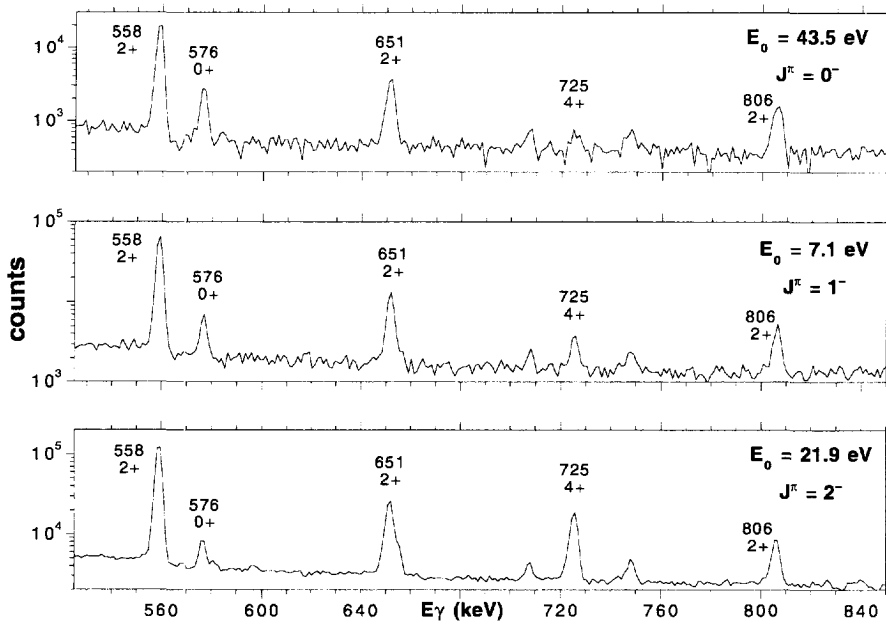

Figure 42: Three examples of the capture gamma-ray spectrum in the 525-850 keV energy region for the first three *p*-wave resonances having different spins.

and the results of the spin assignments obtained by the various ratios are entirely consistent amongst each other. Some of the examined *s*-wave resonance spins were already known and given in the literature [63]; the current assignments confirm these values.

In the case of *p*-wave resonances, where, due to counting statistics, background and contamination from nearby resonances are more important, not all these ratios gave a clear splitting in three groups. We found that the ratio $R = I_{725}/I_{558}$ was the most useful. Values of this ratio are plotted in figure 43 for *s*-wave and *p*-wave resonances. To distinguish the different groups of spins more clearly, we have plotted the ratios R in increasing order so that a jump in two consecutive values on the y-axis indicates a change of spin. As the number of groups into which the data will split is known *a priori*, this treatment is justified. There is still a spread in each spin group due to a complex variety of influences from background corrections and other resonances and due to the fact that the gamma decay is not an entirely statistical process but that still some structure effects may favour specific gamma cascades. The 23 *s*-wave resonances in figure 43 split into two groups of four 0^+ and nineteen 1^+ resonances while the 21 *p*-wave resonances can be divided into three groups of three 0^-, ten 1^- and eight 2^- resonances. The numerical values of the ratio are given in table 11 and the spin assignments resulting from them are summarized in table 14

on page 100. The *p*-wave nature of resonances has been accepted on basis of ref. [143]. The energies are based on the energy calibration of this experiment.

In figure 43 also the ratio as calculated by the model simulations, described in section 3.7. on page 62, is shown. The gray regions represent the spread (one standard deviation) of the simulated ratio using the Kadmenskii photon strength function and the backshifted Fermi gas level density. The simulated ratios are in good agreement with the experimental data.

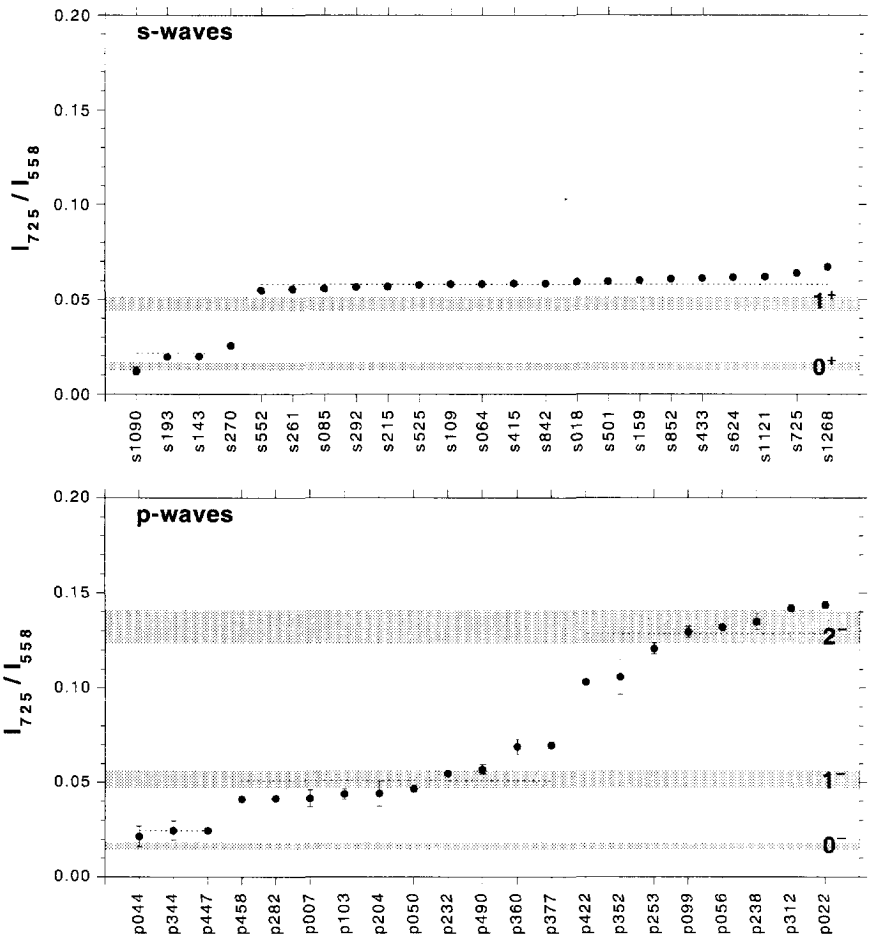

Figure 43: The ratio of the intensities of the 725 keV and the 558 keV gamma-rays, for both *s*- and *p*-wave resonances, in increasing order. The dotted lines indicate the weighted mean of each spin group. The gray regions represent the results of the numerical simulations.

Table 11: Values of the ratio I_{725} / I_{558} for 23 *s*-waves and 21 *p*-waves in ^{113}Cd

s-waves E_0 (eV)	ratio I_{725} / I_{558}	*p*-waves E_0 (eV)	ratio I_{725} / I_{558}
18.41	0.0121±0.0021	7.08	0.0215±0.0053
63.82	0.0197±0.0002	21.91	0.0247±0.0050
85.13	0.0198±0.0002	43.50	0.0247±0.0012
108.5	0.0254±0.0002	49.81	0.0410±0.0014
143.2	0.0550±0.0007	56.32	0.0413±0.0013
158.8	0.0554±0.0002	98.7	0.0415±0.0046
192.9	0.0559±0.0001	102.5	0.0439±0.0027
215.4	0.0567±0.0004	203.6	0.0440±0.0066
261.2	0.0570±0.0002	232.4	0.0467±0.0017
269.6	0.0578±0.0006	237.9	0.0546±0.0008
291.8	0.0583±0.0001	252.7	0.0570±0.0027
414.5	0.0583±0.0001	282.0	0.0689±0.0042
432.5	0.0585±0.0003	312.4	0.0698±0.0018
501.3	0.0586±0.0009	343.9	0.1030±0.0015
525.3	0.0592±0.0001	351.7	0.1059±0.0093
552.2	0.0597±0.0004	359.5	0.1209±0.0029
624.3	0.0602±0.0002	377.0	0.1296±0.0029
724.8	0.0609±0.0009	422.3	0.1320±0.0010
842.4	0.0613±0.0004	447.3	0.1350±0.0040
851.9	0.0619±0.0011	457.9	0.1419±0.0019
1089.9	0.0622±0.0011	490.1	0.1437±0.0018
1120.9	0.0638±0.0015		
1268.4	0.0672±0.0012		

5.6. Results from high-energy gamma rays

Strong primary gamma transitions to 0^+ and to 3^+ states have been observed in several *p*-wave resonances, indicating $E1$ transitions from respectively 1^- and 2^- resonances. Because the low-lying states in ^{114}Cd are well separated, also the primary transitions populating them are distinctly spaced and therefore adequately identifiable. Indications for 2^- *p*-wave resonances were obtained from the gamma rays of 7179 and 6838 keV, leading to 3^+ states. This is shown in figure 44 for the three resonances at 22, 56 and 312 eV. Gamma rays of 9043, 7908, 7737, 7183 and 6605 keV, transitions to 0^+ states, indicate 1^- *p*-wave resonances. They were observed in the case for the 8 *p*-wave resonances of which the spectra are shown in figure 45. The spins of *p*-wave resonances that are obtained by detection of primary gamma rays are also listed in table 14. These data are consistent with the assignments from the low-level population method.

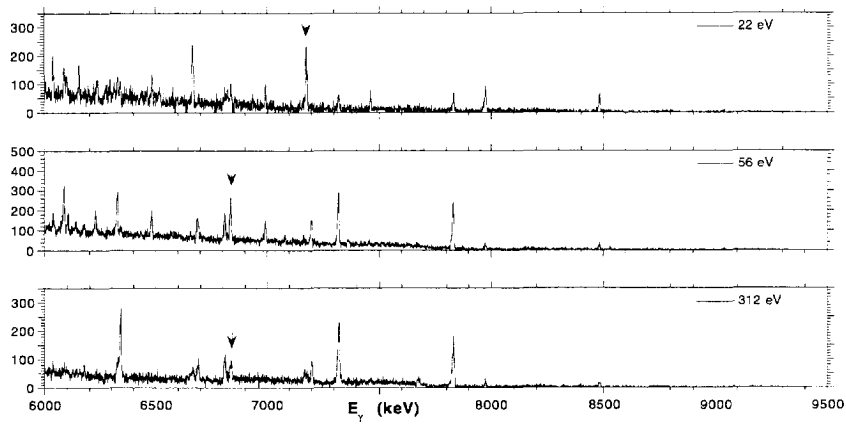

Figure 44: The high-energy gamma-ray spectra for three ^{114}Cd p-wave resonances showing primary transitions to 3^+ states (arrows), therefore indicating a 2^- resonance state.

5.6.1 determining the absolute intensity of primary gamma rays

In order to derive the absolute intensities in photons per neutron capture, it is necessary to normalize the intensities to the total capture rate. One method, described by Coceva [121], is to use the fact that every gamma cascade will, in absence of metastable states, end at the ground state. So for many capture events, the sum of the intensities $\sum A_{j0}$ of the gamma rays going from any state j to the ground state, equals the number of observed captured neutrons and is directly proportional to the total radiation width Γ_γ. Not all the gamma rays are observed because of the energy dependent efficiency $\varepsilon(E_\gamma)$ of the detector, which has to be taken into account. This means that the total number of captured neutrons C_i in a resonance i is

$$C_i = \sum_j A_{j0}/\varepsilon(E_{\gamma j0}). \tag{74}$$

In general, the sum is rapidly converging with increasing gamma energy and in practise it is sufficient to incorporate only gamma transitions from the first few lowest levels to the ground state. The total number of photons per captured neutron I_γ for a gamma ray, which is also the fraction of the total radiation width, is then in the same way proportional to the capture rate. So the intensity $I_{\gamma if}$ of a (primary) transition $i \rightarrow f$ is related to the partial width $\Gamma_{\gamma if}$ and total radiation width $\Gamma_{\gamma i}$ as

$$I_{\gamma if} = \frac{\Gamma_{\gamma if}}{\Gamma_{\gamma i}} = \frac{A_{if}/\varepsilon(E_{\gamma if})}{\sum_j A_{j0}/\varepsilon(E_{\gamma j0})}. \tag{75}$$

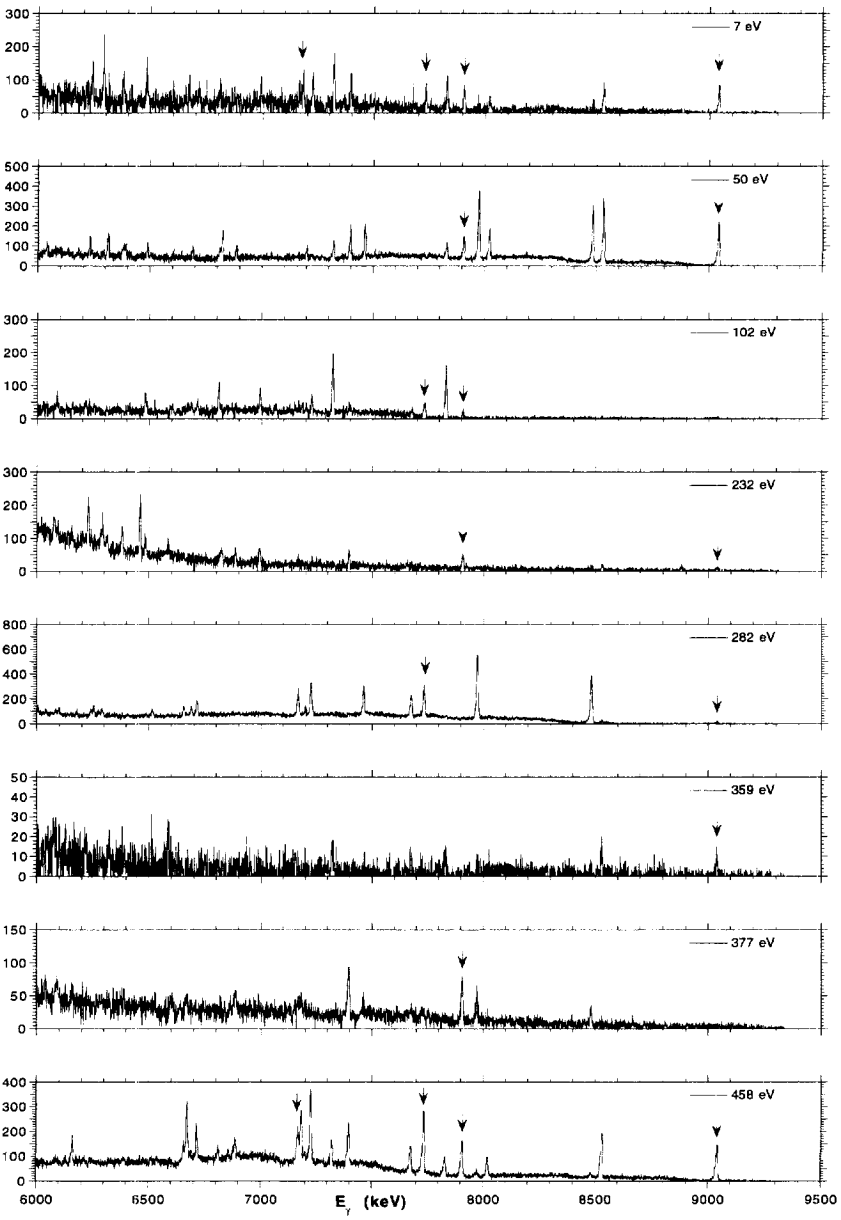

Figure 45: The high-energy gamma-ray spectra for eight ^{114}Cd *p*-wave resonances showing primary transitions to 0^+ states (arrows), therefore indicating a 1^- resonance state.

One of the main advantages is that the quantities used in eq. 75 are included in one single capture experiment, except for the efficiency curve $\varepsilon(E_\gamma)$ of the detector. Therefore there is no need to measure the neutron flux separately for normalization purposes. It is also not necessary to know the absolute efficiency but only a quantity proportional to it because it appears in both the numerator and denominator in eq. 75.

However, one needs to be able to detect the gamma-ray transitions to the ground state for the first few states because they contain the main part of the sum of eq. 74. In the case of ^{114}Cd, up to an energy of about 2500 keV, six gamma transitions decay directly to the ground state. These are the gamma-ray transitions from the levels at 558 (2^+), 1209 (2^+), 1364 (2^+), 1841 (2^+), (2047 (2^+)) 2456 (1^-) and (2525 (2^+)) keV. Also the 0^+ levels at 1134, 1306, 1859 and 2437 keV, shown in figure 38, decay to the 0^+ ground state but these are internal conversion and internal pair production transitions and are therefore not observed. The observed gamma ray of 1306 keV is not originating from the 1306 keV level but from the 1864 keV level.

5.6.2 detector efficiency

To determine the efficiency of our germanium detectors as a function of energy, it is possible to use the gamma rays of thermal neutron capture. This has the advantage that the geometrical distribution and attenuation of the gamma source is exactly the same as in the

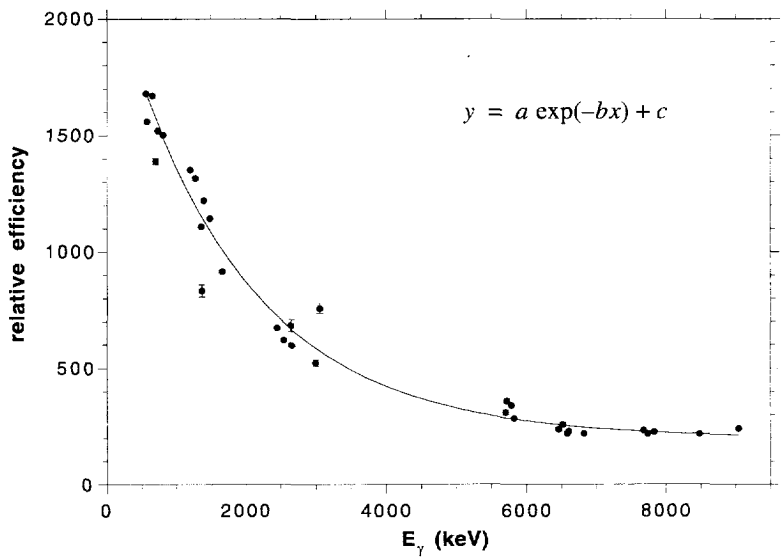

Figure 46: The relative efficiency of a germanium detector, measured with gamma rays form thermal neutron capture in ^{113}Cd(n,γ).

resonance capture experiment. The intensities of these thermal capture gamma rays are rather well known from ref. [146].

We performed a separate measurement of the gamma-ray spectrum of ^{113}Cd(n,γ) selecting the events having the neutron energy within the thermal energy range. The linac was operating at 100 Hz so that the long flight times could be measured. From this thermal spectrum 33 isolated and relatively strong gamma rays with energies ranging from the first excited state at 558 keV up to the neutron threshold at 9043 keV were taken. Next the areas of these peaks were determined and each area was divided by the intensity known from ref. [146]. The quantity obtained in this way is proportional to the detection efficiency. In figure 46 this relative efficiency is plotted against the gamma-ray energy. The error bars correspond only to the determination of the area, because for the published gamma-ray intensities from thermal capture no errors are given. These errors are likely to be small. The obtained data appear at high energy as a nearly constant nonzero value, and the data can be fitted well by the sum of a constant and an exponentially decaying curve. The fitted curve is used as the efficiency curve $\varepsilon(E_\gamma)$ in the determination of the gamma-ray strengths in the resonances.

5.6.3 theoretical estimates of primary gamma-ray intensities

One can use the models for photon strength functions of section paragraph 3.3 on page 49 in order to obtain an estimate for the strength of the gamma rays. The absolute intensity expressed in photons per capture is obtained by dividing the partial widths by the total radiation width. We assume here a constant radiation width of 0.16 eV [63,143] for all resonances. The intensity expressed in photons per 10 000 neutrons are listed in table 12 for primary gamma rays of 7, 8 and 9 MeV with a resonance spin $J = 0$, 1 and 2.

Table 12: The theoretical predictions of the intensities of primary gamma rays in ^{113}Cd(n,γ).

E_γ (MeV)	I_γ (/10000 n) $J = 0$			I_γ (/10000 n) $J = 1$			I_γ (/10000 n) $J = 2$		
	E1 (L)	E1 (K)	M1	E1 (L)	E1 (K)	M1	E1 (L)	E1 (K)	M1
7.0	35.2	18.6	2.0	12.5	6.6	0.7	8.6	4.5	0.5
8.0	62.4	39.9	3.0	22.2	14.2	1.1	15.2	9.7	0.7
9.0	103.7	83.8	4.3	36.9	29.8	1.5	25.3	20.4	1.1

For these estimates both the Lorentzian shape (L) and the Kadmenskii model (K) was used for the $E1$ radiation while for the $M1$ radiation the single particle model was used. For the level density in all cases the backshifted Fermi gas model was employed. We see from the table that the $E1$ intensity is always at least about a factor 10 larger than the $M1$ radiation. Of course these values are average intensities and the intensity of individual gamma-ray transitions fluctuates with a Porter-Thomas distribution around these values.

5.6.4 fits of primary gamma rays of resonances

The intensities of several pronounced primary gamma rays of p-wave resonances were derived using the above mentioned procedure. The following table gives these intensities.

Table 13: Experimental absolute intensities (per 10 000 neutrons) of primary gamma rays from 1^- and 2^- resonances, populating respectively 0^+ and 3^+ states.

	L_γ (/ 10 000 neutrons)					
	E_γ (keV)					
E_n (eV)	9043 $\rightarrow 0^+$	7908 $\rightarrow 0^+$	7737 $\rightarrow 0^+$	7179 $\rightarrow 3^+$	7183 $\rightarrow 0^+$	6838 $\rightarrow 3^+$
7.1	42.2±8.7	29.5±10.4	24.5±9.7			
21.9				43.8±5.0		
49.8	96.1±5.9	48.6±5.4				
56.3						32.3±3.2
102.5		18.0±6.0	32.7±12.7			
232.4		6.8±1.8				
282.0			104.8±9.4			
312.4						39.4±13.0
359.5	36.6±28.3					
377.0		42.8±18.4				
457.9	94.3±8.1	94.4±7.8	148.5±10.2		75.9±15.2	

One can see that for most of these gamma rays the intensity is in the same order of magnitude as the theoretical estimates for $E1$ radiation. The only exception seems to be the resonance at 232 eV, for which the intensity is found to be lower than the other gamma rays, hence being either a weak $E1$ or a strong $M1$ transition. But in figure 45 it can be seen that nearly the entire radiation width for the primary gamma rays is concentrated in the gamma ray of 7908 keV, strongly suggesting an $E1$ transition. The normalization constant of eq. 74 is likely to contain a large part of the underlying wing of the s-wave resonance at 215 eV, in this way reducing the deduced intensity for the p-wave resonance.

5.7. Concluding remarks

The spin determinations obtained in this way are summarized in table 14 for 23 s-wave and 21 p-wave resonances. The spins of the s-wave resonances indicated with an * were already known from ref. [63]. The spins for the p-wave resonances obtained with the low-level population method and with the use of primary gamma rays, are completely consistent with each other.

The low-level population method could be successfully applied to the case of ^{113}Cd in order to determine the spins of both *s*- and *p*-wave resonances. Numerical simulations have supported these assignments and confirmed the application of the method. Additionally, it was possible to determine the absolute intensities of several primary gamma rays and use the strength of specific primary transitions to derive several of the resonance spins.

Table 14: spin assignments for 23 *s*-wave and 21 *p*-wave resonances in ^{113}Cd

***s*-waves** E_0 **(eV)**	J^π **adopted**	***p*-waves** E_0 **(eV)**	J^π **low lev. pop.**	J^π **primary**	J^π **adopted**
18.41*	1^+	7.08	1^-	1^-	1^-
63.82*	1^+	21.91	2^-	2^-	2^-
85.13*	1^+	43.50	0^-		0^-
108.5*	1^+	49.81	1^-	1^-	1^-
143.2	0^+	56.32	2^-	2^-	2^-
158.8	1^+	98.7	2^-		2^-
192.9*	0^+	102.5	1^-	1^-	1^-
215.4*	1^+	203.6	1^-		1^-
261.2*	1^+	232.4	1^-	1^-	1^-
269.6*	0^+	237.9	2^-		2^-
291.8	1^+	252.7	2^-		2^-
414.5*	1^+	282.0	1^-	1^-	1^-
432.5*	1^+	312.4	2^-	2^-	2^-
501.3	1^+	343.9	0^-		0^-
525.3*	1^+	351.7	2^-		2^-
552.2*	1^+	359.5	1^-	1^-	1^-
624.3	1^+	377.0	1^-	1^-	1^-
724.8	1^+	422.3	2^-		2^-
842.4	1^+	447.3	0^-		0^-
851.9*	1^+	457.9	1^-	1^-	1^-
1089.9	0^+	490.1	1^-		1^-
1120.9	1^+				
1268.4*	1^+				

Chapter 6

Estimation of the root mean squared parity nonconserving matrix element

6.1. Introduction

In the investigation of parity nonconservation in neutron p-wave resonances the longitudinal asymmetries are measured as explained in section 1.1.4 on page 9. From the measured longitudinal asymmetries $P_i \pm \delta P_i$, one wants to extract information about the expectation value of the root-mean-squared parity nonconserving matrix element M. This quantity contains the overall information about the strength of the weak interaction in the compound nucleus considering that the individual matrix elements of the parity nonconserving interaction are supposed to be samples from a Gaussian distribution with mean zero and variance M^2.

In the case of target nucleus spin $I = 0$, like ^{238}U and ^{232}Th, the s-wave resonances have spin $J = 1/2$ while the p-wave resonances may have spin $J = 1/2$ or $3/2$; only the former can be admixed by the $J = 1/2$ s-wave resonances. Therefore, in the estimation procedure of M only the data for the $J = 1/2$ p-wave resonances should be included. The measured asymmetries for the $J = 3/2$ p-wave resonances must be consistent with zero and can possibly be used to derive information about systematic errors. Additionally, the effects can only be measured in a limited number of resonances (in the hitherto published data 16 for ^{238}U [50] and 23 for ^{232}Th [51]). Although the experimental data might seem to be somewhat indigent, the statements derived from it are quite far-reaching, and the subject deserves a careful statistical analysis.

The parity nonconservation measurements are experimentally difficult and require a attentive analysis, especially to extract the smaller effects. The p-wave resonances showing small asymmetries and large relative errors can have either spin 1/2 or spin 3/2, the latter of course with a theoretical longitudinal asymmetry equal to zero. Even with a measured asymmetry of the order of twice the quoted error there is a fair possibility that it is not a spin 1/2 p-resonance. This generates an uncertainty in the analysis of the PNC data. The best way to get around this problem is knowing the resonance spins.

In the following the procedure of estimating M from the PNC data for a spin zero nucleus will be described. PNC data concerning the zero spin target nucleus ^{238}U have been published [49,50]. The spin assignments of this thesis make in this case a more accurate estimate of M possible. If the target nucleus has a nonzero spin the problem is more complicated because the s-wave resonances can have different spins and also the unknown $j = 1/2$ fraction of the neutron width at the entrance channel comes into play as explained in section 1.1.5 on page 10. This case will not be discussed here, notably the PNC data of ^{113}Cd have not yet been published by the TRIPLE group.

When the spins of the resonances are not known, a somewhat *ad hoc* procedure concerning the spins has been applied to derive an estimate of M. Two approaches have been developed for this situation and will be discussed here. One is from the TRIPLE group, as used in the analysis of the ^{238}U [50] and ^{232}Th [51] data, and another one has been first proposed by Bunakov [152,153] and is applied in this thesis to the case of ^{238}U.

The estimation of M, described in this chapter, is based on the maximum likelihood method. The theory for maximum likelihood estimation is well established and can be found in many textbooks on statistics, for example Kendall and Stuart [154]. Also the Baysian approach has been described extensively in the literature and good examples can be found in Eadie *et al.* [155] and Barlow [156]. A brief outline of the maximum likelihood method will be given in the section 6.3.

6.2. The distribution of the reduced asymmetries

6.2.1 the longitudinal asymmetries

The hypothetical error-free longitudinal asymmetries R_i in a p-wave resonance labelled i are related to the PNC mixing matrix elements V_{ij} relating this p-wave resonance and the s-wave resonance labelled j as (see also eq. 12 on page 12)

$$R_i = \sum_j \frac{2V_{ij}}{E_{s,j} - E_{p,i}} \cdot \frac{\gamma_n^{s,j}}{\gamma_n^{p,i}} = \sum_j A_{ij} V_{ij} \tag{76}$$

where the matrix elements V_{ij} are assumed to be samples of a Gaussian distribution with zero mean and variance M^2, denoted by $N(0, M^2)$. All terms other than V_{ij} are encapsulated into the factors A_{ij}. The energy difference as well as the neutron channel amplitudes γ_n in eq. 76 are supposed to have a random sign and to be independent of each other and of the considered resonance i. In fact, the neutron channel amplitudes γ_n are not known, but the neutron widths $\Gamma_n = \gamma_n^2$ are. Because of the assumption of random sign of the amplitudes, $\Gamma_n^{1/2}$ is used instead of γ_n. In the absence of any observational errors the expectation values $E\{R_i\}$ and $E\{R_i^2\}$ are given by

$$E\{R_i\} = E\{\sum_j A_{ij}V_{ij}\} = \sum_j A_{ij}E\{V_{ij}\} = 0 \tag{77}$$

and

$$E\{R_i^2\} = E\{\left(\sum_j A_{ij}V_{ij}\right)\left(\sum_j A_{ij}V_{ij}\right)\} = \sum_j A_{ij}^2 E\{V_{ij}^2\} = A_i^2 M^2 \tag{78}$$

where the quantity A_i is defined by

$$A_i^2 = \sum_j A_{ij}^2 \tag{79}$$

and the elements A_{ij} are calculated from the resonance energies and neutron widths

$$A_{ij} = \frac{2}{E_{s,j} - E_{p,i}}\left(\frac{\Gamma_n^{s,j}}{\Gamma_n^{p,i}}\right)^{1/2}. \tag{80}$$

Usually, this quantity can be determined quite well from known resonance parameters. The influence on the p-wave resonance of more distant s-wave resonances is very limited.

6.2.2 random variables

Now consider the quantities R_i to be samples of a random variable (RV) r with distribution $N(0, M^2)$. What will be observed in a measurement are the observations P_i that can be regarded as samples from the random variable p defined as

$$p = r + d \tag{81}$$

where d is the observational error, also a RV. In fact, for each observation i an individual standard deviation D_i is derived from the measurements and the actual error is a sample from the RV d_i, supposed to be normally distributed as $N(0, D_i^2)$. In this context, the observational variances D_i^2 are not supposed to have a common distribution. Therefore, the observations do not form a single RV, but a set of RVs p_i

$$p_i = r + d_i. \tag{82}$$

Assuming that r and d_i are independent of each other and that r is independent of i, the probability density function of p_i is the convolution of r and d_i

$$f_{p_i}(p_i) = f_r(r) * f_{d_i}(d_i) \tag{83}$$

where the symbol * denotes the convolution operation. In this case of Gaussian distribution we use the fact that the convolution of two Gaussians $N(\mu_1, \sigma_1^2)$ and $N(\mu_2, \sigma_2^2)$ is again a Gaussian function $N(\mu_1 + \mu_2, \sigma_1^2 + \sigma_2^2)$ [157]. For each RV p_i holds

$$E\{p_i\} = 0 \tag{84}$$

$$E\{p_i^2\} = A_i^2 M^2 + D_i^2. \tag{85}$$

The observations P_i and D_i^2 can be transformed into the new quantities $X_i = P_i/A_i$ and $e_i^2 = D_i^2/A_i^2$. The X_i are then samples of the RVs x_i with the properties

$$E\{x_i\} = 0 \tag{86}$$

$$E\{x_i^2\} = M^2 + e_i^2. \tag{87}$$

The probability density function of the RVs x_i is then

$$f_i(x_i) = \frac{1}{\sqrt{2\pi\,(M^2 + e_i^2)}} \exp\left(\frac{-x_i^2}{2\,(M^2 + e_i^2)}\right). \tag{88}$$

The quantities X_i, which we will call reduced asymmetries, are a sample from the Gaussian distribution function eq. 88 with zero mean and variance $M^2 + e_i^2$. The problem is reduced to estimating the variance M^2 of the distribution $N(0, M^2 + e_i^2)$ from a set of data with errors $X_i \pm e_i$. At least, if it is known which PNC data from which resonances have to be included. In fact, the quoted errors e_i are the square roots of the measured variances. The probability density function given by eq. 88 is the typical relation between the observed values X_i and the expectation value of the root-mean-squared parity nonconserving matrix element M [49,50,53].

In the case of a target nucleus spin with $I = 0$ and with the spins of the resonances known, one can take the data from the $J = 1/2$ p-waves, determine the mixing factors A_i from all the s-waves into the p-wave i and then apply a maximum likelihood procedure to derive a value for M. This will be discussed for ^{238}U in section 6.4.4.

6.3. Maximum likelihood method

An estimator $\hat{\vartheta}$ is the procedure applied to a given set of data X_i in order to obtain a numerical value for a parameter ϑ of the parent distribution function. Such a procedure

can be of any kind and to distinguish between "good" and "bad" estimators three basic properties have to be considered: consistency, bias and efficiency.

An estimator is *consistent* if it tends to the true value ϑ when the number of data values N goes to infinity

$$\lim_{N \to \infty} \hat{\vartheta} = \vartheta . \tag{89}$$

For finite N the estimator $\hat{\vartheta}$ will in general not give the true value ϑ. If the probability density function of $\hat{\vartheta}$ is symmetric around ϑ, the estimator is said to be *unbiased*. This means that the expectation value $E\{\hat{\vartheta}\}$ equals the true value ϑ. Unbiasedness and consistency do not imply each other.

The variance of an estimator gives a measure of how close $\hat{\vartheta}$ is to the true value ϑ. If one estimator has a smaller variance than another, it is said to be more *efficient*. A lower limit on the variance of an estimator exists, the Cramér-Rao lower bound (CRLB) on the variance. For an unbiased estimator the expression, known as the Cramér-Rao inequality, is

$$\mathrm{Var}(\hat{\vartheta}) \geq \frac{-1}{E\{d^2 \ln L(\vartheta)/d\vartheta^2\}} \tag{90}$$

where $L(\vartheta)$ is the likelihood function defined as the joint probability density function, which is the product of the probability density functions of the independent data X_i, as a function of ϑ

$$L(\vartheta) = P(\vartheta|x) = \prod_i P_i(X_i, \vartheta) . \tag{91}$$

The likelihood function is also the basis of a class of estimators that is widely used, the maximum likelihood estimators. This estimator is the value of ϑ that maximizes $L(\vartheta)$. Standard statistical techniques as weighted mean and least squares minimization are based on the maximum likelihood method.

The maximum likelihood estimator has some attractive properties that makes it so commonly used. It is a consistent estimator and for large N, the asymptotic limit, it becomes unbiased. Again for $N \to \infty$, the variance reaches its lowest possible value, the CRLB. Besides, the estimator is invariant under parameter transformations. This means that if we do not want to estimate ϑ but a function of it, $f(\vartheta)$, the estimator $\hat{f}(\vartheta)$ will have a maximum in the likelihood function $L(f(\vartheta))$ at $f(\hat{\vartheta})$. This means that one can choose the most suitable form of a parameter to find the maximum and the result is the same when the parameter is for example ϑ^2 or $\sqrt{\vartheta}$.

Although this is true for the value where the maximum of the likelihood function occurs, this is not true for the biasedness of an estimator. For small N far from the asymptotic limit, the maximum likelihood estimator is generally biased and even if ϑ is an unbiased estimator, a related estimator $f(\vartheta)$ is usually not.

This property makes it also easy to derive confidence intervals. Because there is always a parameter transformation possible that turns the logarithm of the likelihood function $\ln L(\vartheta)$ into a parabola, like in the Gaussian case, one can derive a 68% or 1σ and a 95.4% or 2σ confidence interval from the points where $\ln L(\vartheta)$ is 1/2 respectively 2 lower than the maximum value $\ln L(\vartheta_{max})$

$$\ln L(\vartheta_{max}) - \ln L(\vartheta_{1\sigma}) = \frac{1}{2} \tag{92}$$

$$\ln L(\vartheta_{max}) - \ln L(\vartheta_{2\sigma}) = 2. \tag{93}$$

This is always true, also for finite N [155]. But it should be stressed that for small N the likelihood can be highly non-Gaussian and the limits corresponding to the 95.4% confidence interval may be much larger than twice the 1σ limits although it is often referred to as a 2σ interval.

In fact, the full definition of the likelihood function originates from the Bayesian post probability in Bayes theorem for conditional probabilities [155]

$$L(\vartheta) \equiv P(\vartheta \mid x) = \frac{P(x \mid \vartheta) P(\vartheta)}{P(x)} \tag{94}$$

where $P(x \mid \vartheta)$ is the probability density function of a random variable x given a parameter ϑ and where in contradistinction to eq. 91 also the two marginal distributions $P(x)$ and $P(\vartheta)$ are involved.

So far this is all generally accepted. The point where the world of statisticians is divided into two groups, the "Bayesians" and "Classicals", is the interpretation of $P(\vartheta)$, the prior knowledge on the parameter ϑ. "Classicals" will not accept any prior knowledge and say that before an experiment nothing is known about ϑ and therefore $P(\vartheta)$ should be uniform and constant (note that this concept of a probability function in the Bayesian context is less strict than the mathematical probability). On the contrary, "Bayesians" will use any information on ϑ that is available and put this into $P(\vartheta)$. If for example it is known that ϑ is always positive, then $P(\vartheta) = u(\vartheta)$, the unit step function.

If ϑ denotes a PNC root mean squared matrix element, it is clear that ϑ cannot be negative. On the other hand, ϑ cannot be infinitely large, because of its limited strength. The lower limit of zero is clear. One could also take an upper limit, but the chosen shape of

$P(\vartheta)$ will be completely subjective. This is the major drawback of the Bayesian approach. Not everybody agrees on the prior information and this can be quite a subjective affair.

The marginal distribution $P(x)$ in eq. 94, as it is independent of ϑ, normalizes the likelihood function and is defined as

$$P(x) = \int P(x|\vartheta)P(\vartheta)d\vartheta. \tag{95}$$

In the Bayesian approach the likelihood function defined in eq. 94 becomes in this way a probability distribution. There is not any more a true value ϑ which can be estimated as in the classical approach, but ϑ is a random variable whose distribution function is given by eq. 94.

6.4. Estimation of *M* when the spins are known

It is an old and trivial problem to estimate the variance of the distribution from a set of numbers $X_1 \ldots X_N$, sampled from a normal distribution $N(\mu, \sigma^2)$. If the distribution has a known mean μ and an unknown variance σ^2, its estimator $\widehat{\sigma^2}$ is generally taken as

$$\widehat{\sigma^2} = \frac{1}{N}\sum_{i=1}^{N}(X_i - \mu)^2. \tag{96}$$

This estimator is unbiased, the expectation value $E\{\widehat{\sigma^2}\}$ equals the true value σ^2. The estimator is also consistent, i.e. $\widehat{\sigma^2}$ converges to σ^2 as N increases.

It is less trivial to estimate the variance of the distribution when the set of numbers are not just numbers but observations having observational uncertainties: $X_1 \pm e_1 \ldots X_N \pm e_N$ as is the case in data obtained from parity nonconservation experiments. The data X_i are distributed as $N(0, M^2)$, a Gaussian distribution with known mean zero and an unknown variance M^2. The way how to obtain an estimator for the quantity M is described next.

6.4.1 estimating *M* from data with errors.

Now we do not have a set of N observations $X_1 \ldots X_N$, but a set of observations with uncertainties $X_1 \pm e_1 \ldots X_N \pm e_N$. The quantities e_i^2 are considered to be the variance of the normally distributed error in observation labelled i. Each observation X_i is a sample of a random variable x_i of which the distribution is given by eq. 88. The joint probability density function $f(x_1, \ldots, x_N)$, assuming that the x_i are independent, for the N random variables x_i is written as the product

$$f(x_1, \ldots, x_{N_i}) = \prod_{i=1}^{N} \frac{1}{\sqrt{2\pi\,(M^2 + e_i^2)}} \exp\left(\frac{-x_i^2}{2\,(M^2 + e_i^2)}\right). \tag{97}$$

The general construction of the maximum likelihood function is to take the joint probability density function and substitute the observations. This is a function of only one parameter, the parameter M to be estimated. So to estimate M using the maximum likelihood method, we take eq. 97 and substitute the observations $X_1 \ldots X_N$ to obtain the likelihood function of the parameter M

$$L(M) = \prod_{i=1}^{N} \frac{1}{\sqrt{2\pi\,(M^2 + e_i^2)}} \exp\left(\frac{-X_i^2}{2\,(M^2 + e_i^2)} \right) \tag{98}$$

or its logarithm, called the log likelihood function

$$\ln L(M) = -\frac{1}{2} N \ln 2\pi - \frac{1}{2} \sum_{i=1}^{N} \ln(M^2 + e_i^2) + \sum_{i=1}^{N} \frac{-X_i^2}{2\,(M^2 + e_i^2)}. \tag{99}$$

Finding the maximum of a function is the same as finding the maximum of its logarithm. We take the first derivative to M of the log likelihood function and put it equal to zero to find the maximum, which is a necessary condition

$$0 = \frac{d}{d(M)} \ln L(M) = \left(\sum_{i=1}^{N} \frac{-1}{M^2 + e_i^2} + \sum_{i=1}^{N} \frac{X_i^2}{(M^2 + e_i^2)^2} \right) M \tag{100}$$

which gives the trivial solution $M = 0$ or

$$\sum_{i=1}^{N} \frac{M^2 + e_i^2 - X_i^2}{(M^2 + e_i^2)^2} = 0. \tag{101}$$

Putting the first derivative of $L(M^2)$ to M^2 equal to zero gives the same result eq. 101. The solution of this implicit equation gives the maximum likelihood value which has in general to be solved numerically. For finite N, this value is in general biased. However, the solution $\hat{M}^2$ or $\widehat{M^2}$ of this equation has not necessarily a positive value (note that $\widehat{M^2}$ means the estimate of M^2 and that $\hat{M}^2$ means the square of $\hat{M}$). Large values of e_i^2 compared to X_i^2 can give a negative solution M^2, which has not a physical meaning. In this case the other solution $M = 0$ of eq. 101 gives the correct value. In fact, this seems to be a logical consequence: if the observations X_i^2 are small compared to their variances e_i^2, they may be not a parity nonconserving matrix element, but values consistent with zero. For a set of PNC data, all belonging to the Gaussian distribution and with not reasonably small variances, eq. 101 can be directly applied because the maximum is certainly at a positive value.

variance

Although it may be convenient to transform the searched parameter in order to find the maximum likelihood value, the invariance principle holds only for the maximum. As soon as the variance or confidence limits for a parameter are derived, they can not be transformed into limits for a transformed estimator.

One can derive the CRLB for an unbiased estimator $\hat{M}$ using eq. 90 which gives

$$\mathrm{Var}(\hat{M}) \geq -1/E\{\frac{d^2 \ln L(M)}{d(M)^2}\} = -1/E\left\{\sum_{i=1}^{N} \frac{M^2 - e_i^2}{(M^2+e_i^2)^2} + \sum_{i=1}^{N} \frac{x_i^2(-3M^2+e_i^2)}{(M^2+e_i^2)^3}\right\} \quad (102)$$
$$= 1/\sum_{i=1}^{N} \frac{2M^2}{(M^2+e_i^2)^2}$$

while taking the CRLB for the estimator $\widehat{M^2}$ gives

$$\mathrm{Var}(\widehat{M^2}) \geq -1/E\{\frac{d^2 \ln L(M^2)}{d(M^2)^2}\} = -1/E\left\{\sum_{i=1}^{N} \frac{1}{2(M^2+e_i^2)^2} - \sum_{i=1}^{N} \frac{x_i^2}{(M^2+e_i^2)^3}\right\} \quad (103)$$
$$= \left(1/\sum_{i=1}^{N} \frac{1}{2(M^2+e_i^2)^2}\right).$$

Given the set of variances e_i^2, the CRLB is the smallest possible variance of the unbiased estimator, which is often not reached for small N. It can be beneficial to estimate the variance by numerical simulations while making some assumptions about the values of e_i^2, as done in section 6.4.3. The inequality of eq. 90 on page 105 becomes an equality in the asymptotic limit for $N \rightarrow \infty$. In practice this limit can not be reached with a small sample and the variance will be larger. Sometimes it is more convenient to quote the confidence limits derived from eq. 92 or eq. 93, like in this case because of the asymmetric shape of L due to one-side boundness of the parameter M^2. Also then it is necessary to specify if they have been derived from $L(M)$ or from $L(M^2)$.

6.4.2 behaviour of the solution of eq. 101

However, the solution of eq. 101 can give negative values for M^2 if the e_i are large. In that case the maximum likelihood is found for the trivial solution $M = 0$. Apart from the general case we can distinguish two special cases, namely the situation where the uncertainties are zero and where they have all the same nonzero value $e_i = e$.

the uncertainties are zero

Of course, in this case where $e_i = 0$, eq. 101 reduces to eq. 96, the usual estimate of the variance with $\mu = 0$

$$\widehat{M^2} = \frac{1}{N}\sum_{i=1}^{N} X_i^2. \tag{104}$$

It is easy to show that the expectation of the estimator is

$$E\{\widehat{M^2}\} = E\left\{\frac{1}{N}\sum_{i=1}^{N} x_i^2\right\} = \frac{1}{N}NM^2 = M^2 \tag{105}$$

so this is an unbiased estimator. The variance of this estimator can be shown to be [156]

$$\mathrm{Var}(\widehat{M^2}) = \frac{2M^4}{N}. \tag{106}$$

If not $\widehat{M^2}$ but $\hat{M}$ is used as an estimator, the variance becomes

$$\mathrm{Var}(\hat{M}) = \frac{M^2}{2N}. \tag{107}$$

These two variances are the CRLB from eq. 102 and eq. 103, corresponding to all values of e_i set to zero.

the uncertainties have all the same value

If all uncertainties are equal, $e_i = e$, eq. 101 reduces to

$$\widehat{M^2} = -e^2 + \frac{1}{N}\sum_{i=1}^{N} X_i^2. \tag{108}$$

This shows the possibility of negative solutions if the X_i^2 are small compared to e^2. Also this estimator is unbiased as the expectation of the estimator is

$$E\{\widehat{M^2}\} = E\left\{-e^2 + \frac{1}{N}\sum_{i=1}^{N} x_i^2\right\} = -e^2 + M^2 + e^2 = M^2. \tag{109}$$

6.4.3 simulations to derive the bias and variance

However, the general case, and what happens in practice, is that all the uncertainties are different. In that case eq. 101 has to be solved numerically to get a value for the estimator and the bias cannot be calculated analytically. To have an idea of its magnitude it is possible to generate a data set of N values $X \pm e$, estimate M from it and repeat this many times. The mean value of all these estimates is the expectation value of the estimator.

In the following simulations, we took a fixed value M_{fix} for M and a sample of N values r_i from the distribution $N(0, M_{fix}^2)$. To each of these values we added an error ε_i. For the simulations we assume that the errors have a Gaussian distribution $N(0, e_i^2)$. Normally, there is no underlying distribution for the variances of these error distributions and we have to make an assumption about it. Arbitrarily we have taken the variances e_i^2 chosen from a normal distribution $N(0, \Sigma^2)$, with Σ representing the average spread in the variances.

Then, from these generated values $x_i = r_i + \varepsilon_i$ and the variances e_i^2 the most likely value M has been calculated using the likelihood eq. 98. This procedure is repeated a large number of times (here typically 50 000 times). The calculations have been performed for a fixed value $M_{fix} = 1$ and several values of Σ while N was ranging from 2 to 40.

The average values of the estimates $\langle \hat{M} \rangle$ and $\langle \widehat{M^2} \rangle$ have been calculated as well as their variances using

$$\mathrm{Var}(\hat{M}) = \langle (\hat{M} - \langle \hat{M} \rangle)^2 \rangle = \langle \hat{M}^2 \rangle - \langle \hat{M} \rangle^2 \tag{110}$$

and

$$\mathrm{Var}(\widehat{M^2}) = \langle (\widehat{M^2} - \langle \widehat{M^2} \rangle)^2 \rangle = \langle (\widehat{M^2})^2 \rangle - \langle \widehat{M^2} \rangle^2 . \tag{111}$$

In figure 47 the average values $\langle \hat{M} \rangle$ and $\langle \widehat{M^2} \rangle$ are plotted as a function of the number of observations N for 4 values of the parameter Σ, namely 0, 0.5, 1.0 and 2.0. We see the general trend that the larger Σ becomes, the larger the deviation from $M_{fix} = 1$ is, so the larger the bias is. This effect decreases as expected with increasing N. When N goes to infinity, the expectation values of $\langle \hat{M} \rangle$ and the square root of $\langle \widehat{M^2} \rangle$ tend to each other as the invariance principle states. Both values tend also to the value M_{fix}, so the bias goes to zero. However, for a small number N, there are considerable differences between the two estimates, as can be seen from figure 47. In fact for $\Sigma = 0$ the estimator $\langle \widehat{M^2} \rangle$ is unbiased while $\langle \hat{M} \rangle$ has certainly a bias for finite N. So the bias is not the same for the two estimators. There is not a simple relation connecting the two estimators when Σ differs from zero.

Also in figure 47 the variances defined by eq. 110 and eq. 111 are plotted as a function of N. Of course, the larger Σ is, the larger the variance becomes. The values for $\Sigma = 0$ correspond well to respectively eq. 106 and eq. 107, of which the curves (in solid lines) are also shown in the figure. These results hold only in the hypothetical case that the variances have the same underlying distribution. In the context of longitudinal asymmetry measurements this is not necessarily the case and both estimators can be used but their bias may be different. Assuming a Gaussian distribution in the ^{238}U case for the first seven values e_i of the sixth column in table 15, we can deduce $\Sigma = 0.41$.

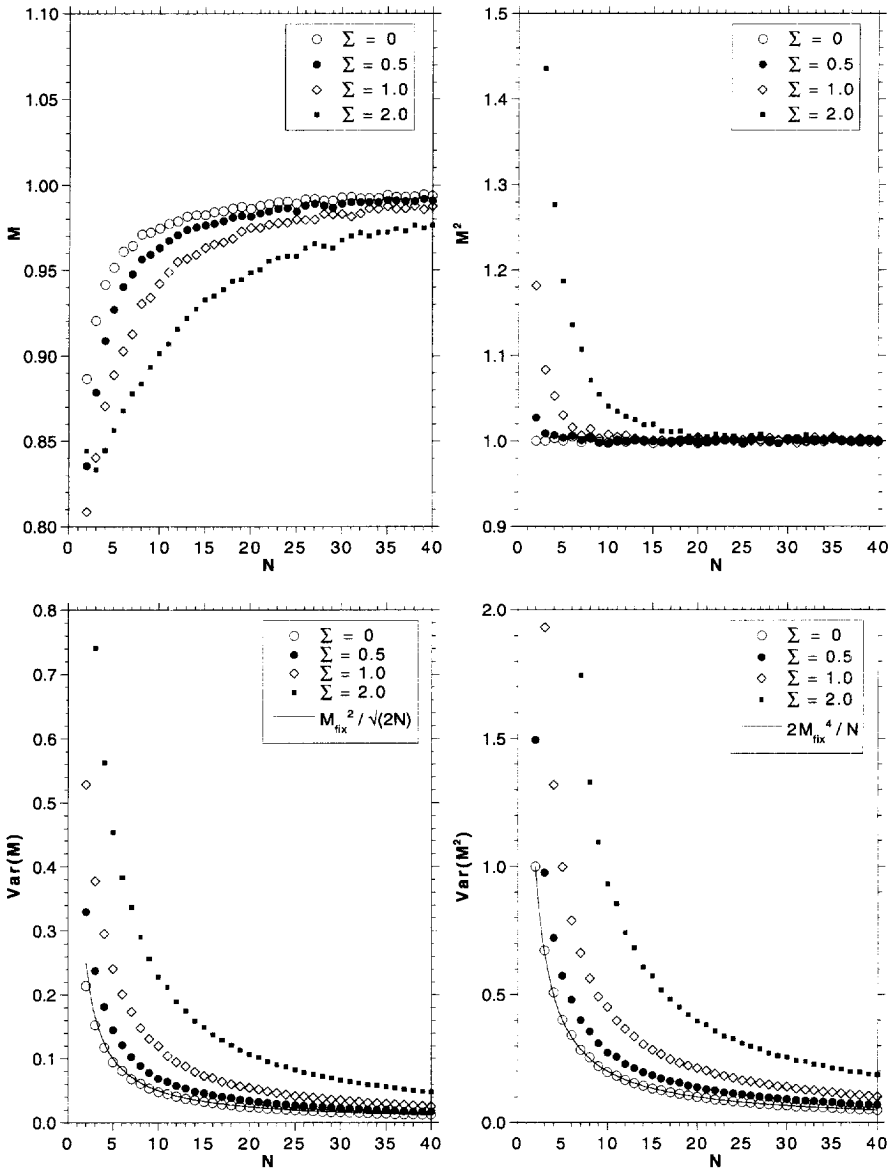

Figure 47: The average values of the estimators for M (upper left) and M^2 (upper right) as well as their variances in a comparable form as a function of the sample size N. The solid curves in the lower graphs represent the variances according to eq. 106 and eq. 107.

6.4.4 application to the ^{238}U case

The measurements of the TRIPLE collaboration concerning parity nonconservation in neutron resonances in ^{238}U should be interpreted in a different way now that the spins are known. In table 15 the seven resonances having spin $J = 1/2$ and the nine having $J = 3/2$ together with the measured properties are given. We can apply the maximum likelihood

Table 15: The PNC parameters for the 16 measured resonances of ^{238}U [50]. With the present spin assignments a division in seven spin 1/2 and nine spin 3/2 p-wave resonances can be made.

	E_n (eV)	P_i (%)	dP_i	$\|A_i\|$ (1/eV)	X_i(meV)	e_i(meV)	X_i/e_i
	11.3	0.67	0.37	47.13	0.14	0.08	1.75
	45.2	-1.31	2.10	34.82	-0.38	0.60	0.63
	63.5	2.63	0.40	34.42	0.76	0.12	6.33
$J = 1/2$	83.7	1.96	0.86	13.58	1.44	0.63	2.29
	89.2	-0.24	0.11	4.70	-0.52	0.24	2.17
	173.1	1.04	0.71	7.80	1.33	0.91	1.46
	242.7	-0.61	0.63	4.87	-1.26	1.28	0.98
	10.2	-0.16	0.08	24.61	-0.07	0.03	2.33
	93.1	-0.03	2.30	24.59	-0.01	0.94	0.01
	98.0	-2.18	1.30	54.21	-0.40	0.24	1.67
	125.0	1.08	0.86	10.56	1.02	0.82	1.24
$J = 3/2$	152.4	-0.14	0.56	4.38	-0.32	1.29	0.25
	158.9	-0.36	1.37	8.57	-0.41	1.59	0.26
	253.9	-0.16	0.65	3.25	-0.49	2.00	0.25
	263.9	-0.01	0.42	2.46	-0.05	1.72	0.03
	282.4	0.41	1.40	4.95	0.82	2.82	0.29

method from eq. 98 and calculate the value for M together with the confidence limits from eq. 92. Doing so results in

$$\hat{M} = 0.58 \,{}^{+0.33}_{-0.20} \text{ or } {}^{+0.88}_{-0.32} \text{ meV} \tag{112}$$

where the first and second error pairs correspond to the 68% and the 95.4% confidence interval respectively, also referred to as 1σ and 2σ in the case of a Gaussian distributed error. The CRLB from eq. 102 gives for the minimum possible variance

$$\sqrt{\text{Var}(\hat{M})} = 0.23\,. \tag{113}$$

bias removal by means of the jackknife method

It must be stated that this estimate of eq. 112 is probably biased and that the unbiased estimate may be somewhat larger as is suggested by the simulations. It is possible to remove

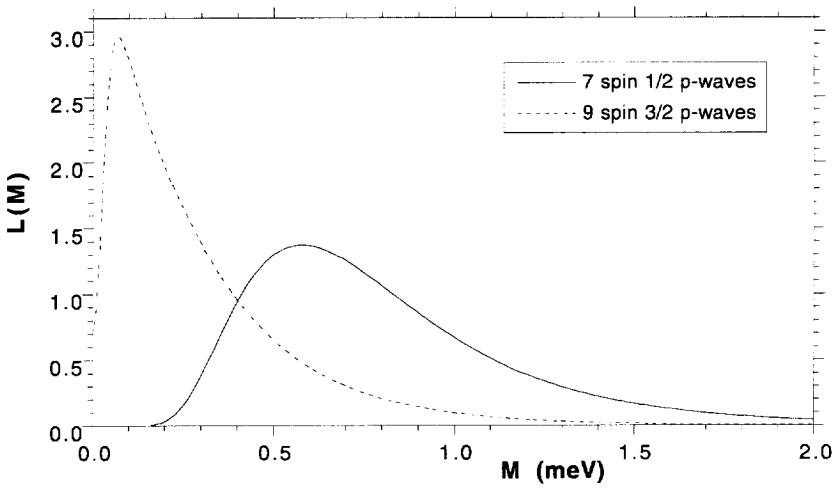

Figure 48: The likelihood functions for the seven spin 1/2 p-waves, resulting in the estimate of eq. 112 and for the nine spin 3/2 p-waves, resulting in the estimate of eq. 116.

the bias by using the method of the jackknife [154]. This consists of taking out at a time one of the N observations to make an estimate t_{N-1} with the remaining $N-1$ values and using the average value $\langle t_{N-1} \rangle$ to obtain

$$t'_N = N t_N - (N-1) \langle t_{N-1} \rangle . \tag{114}$$

This new estimate t'_N is biased only to order $1/N^2$. The variance remains practically the same as the uncorrected estimated. We take here the CRLB for the variance because it is very close to the asymmetric interval of the estimate of eq. 112. Applying this procedure gives the new value

$$\hat{M} = 0.63 \pm 0.23 \quad \text{meV} . \tag{115}$$

application to spin 3/2 data

It is interesting to apply the estimation to the data of the nine p-wave resonances with spin $J = 3/2$. There is no PNC effect in these resonances expected and M should be equal to zero. The estimate $\hat{M}$ should therefore be consistent with zero. Using the values of the nine spin 3/2 resonances gives

$$\hat{M} = 0.07 \, ^{+0.15}_{-0.04} \quad \text{meV} \tag{116}$$

where the errors represent the 68% confidence limits. Both likelihood functions, normalized to unity, are plotted in figure 48. Although the latter maximum likelihood value is

nearly zero, the slow fall-off for increasing M might suggest the presence of some systematic errors.

6.5. Unknown spins: estimate according to TRIPLE

If the resonance spins are not known, only a part of the available data has a $N(0, M^2)$ distribution whereas the other part should be consistent with zero. Values X_i which are much larger than their errors, two or three standard deviations or more, are likely to indicate a genuine PNC effect. But small values of X_i cannot be accurately measured and might have a value much less than two standard deviations. For these cases it is not clear whether this is a PNC effect or not.

In order to estimate M^2 from the ^{238}U data, an assumption has to be made about the possibility of each of the two cases: one needs to know the occurrence of a spin 1/2 p-wave resonance and a spin 3/2 p-wave resonance. It is known that for low spins the density of levels with spin J is in good approximation proportional to $2J + 1$. Therefore, one can say that the occurrence of $J = 1/2$ p-wave resonances is 1/3 and the fraction of $J = 3/2$ p-wave resonances is 2/3.

So the measured value X_i has a probability of 1/3 to be distributed as $N(0, M^2 + e_i^2)$ and a probability of 2/3 to be consistent with zero. The error e_i makes that the latter value has

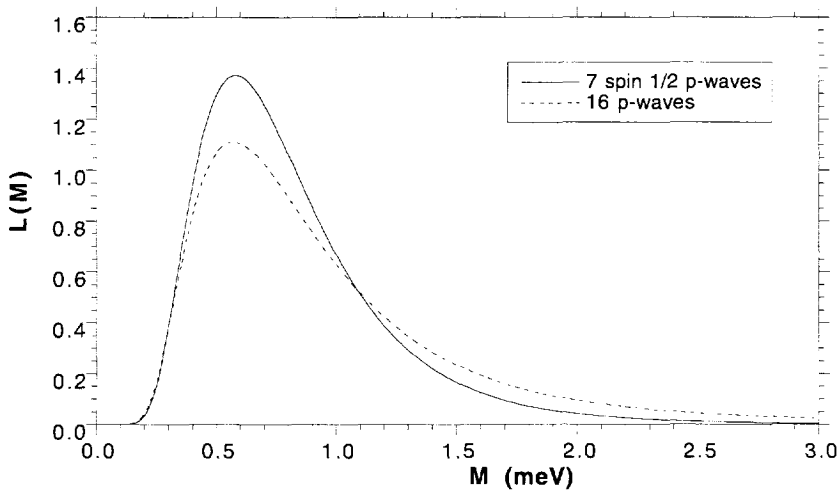

Figure 49: The likelihood function for the sixteen p-waves with spin 1/2 and 3/2 p-waves, resulting in the estimate of eq. 118, compared to the likelihood function for the seven spin 1/2 p-waves.

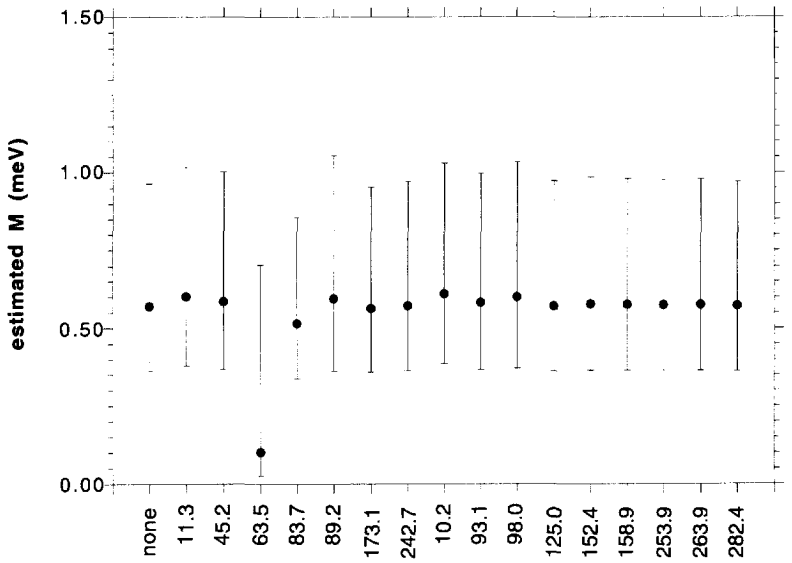

Figure 50: The estimate of M using only fifteen of the sixteen resonances from table 15 with the indicated resonance removed.

a distribution $N(0, e_i^2)$. Accepting this, we can write the likelihood function as the product of the sum of the probability functions [49,50] as

$$L(M) = \prod_{i=1}^{N} \left(\frac{1}{3} \frac{1}{\sqrt{2\pi\,(M^2 + e_i^2)}} \exp\left(\frac{-X_i^2}{2\,(M^2 + e_i^2)} \right) + \frac{2}{3} \frac{1}{\sqrt{2\pi e_i^2}} \exp\left(\frac{-X_i^2}{2e_i^2} \right) \right). \tag{117}$$

Calculating the maximum and the confidence intervals using all investigated sixteen resonances of the ^{238}U target nucleus gives

$$\hat{M} = 0.57 \,{}^{+0.39}_{-0.21} \text{ or } {}^{+1.17}_{-0.33} \text{ meV} \tag{118}$$

to be compared with the estimate when the spins are known. In figure 49 this likelihood function of eq. 117 is plotted together with the case with known resonance spins for comparison. Because the function is not normalizable due to the constant term it contains, the integral up to 10 meV [50] is used for normalization. Both curves give the maximum at nearly the same value of M. This is likely due to the small relative error for the PNC effect of the 63.5 eV resonance.

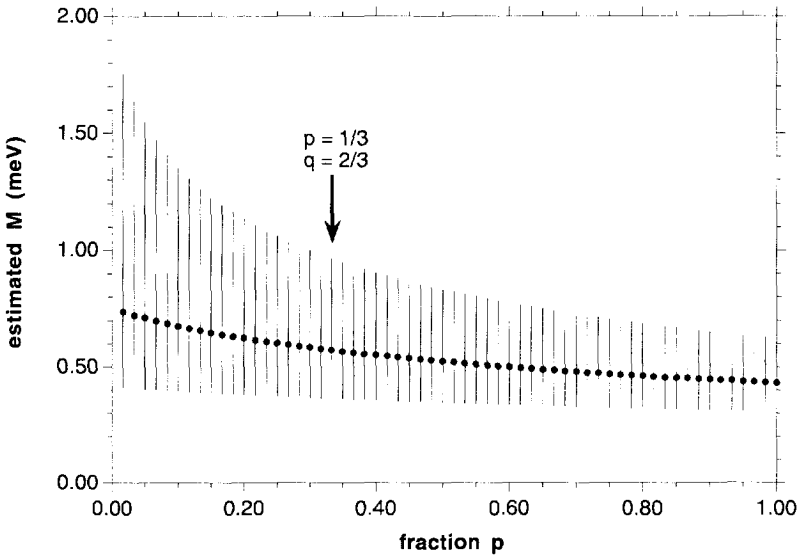

Figure 51: The estimate of M as a function of the fraction $J = 1/2$ p-wave resonances.

6.5.1 sensitivity to one resonance

In fact, eq. 117 turns out to be insensitive to the measurements with small so-called statistical significances X_i/e_i. In that case the second term in eq. 117, independent of M, dominates the sum. For the resonance at 63.5 eV listed in table 15 the statistical significance is 6.3, the largest one. It is in fact the value for this resonance that determines largely the maximum of the likelihood function. We can illustrate this by making the estimate of M but instead of taking all sixteen resonances, we take only fifteen of them, leaving out one of the resonances at a time. In figure 50 these estimates together with their 68% confidence interval are plotted. The x-axis shows the resonance for which the value was taken out of the estimation. The first point corresponds with the estimate eq. 112. It is clear that the resonance at 63.5 eV entirely dominates the estimate. As soon as it is excluded, the value of M drops to a very low value. Also it seems not to make any difference whether the data for a spin 1/2 or a spin 3/2 p-wave resonance is left out of the procedure.

6.5.2 sensitivity to the fraction of spin 1/2 resonances

The estimate derived from eq. 117 is not only sensitive to the accuracy of one measured data point, also the factors 1/3 and 2/3 influence the estimate. Although they have been included for good physical reasons, the ratio 1:2 of the numbers of $J = 1/2$ and 3/2 p-wave resonances can not be taken for granted, especially not for such a small sample of resonances in a narrow energy region. It is interesting to see how the estimate will change if the factors are different. In figure 50 the estimate is plotted as a function of the fraction spin 1/2 p-wave resonances, ranging from 0 to 1, together with the 1σ intervals as error

bars. In this case, the spin assignments have proven that the assumption about the 1:2 ratio happens to be justified.

6.6. Unknown spins: estimate according to Bunakov

6.6.1 likelihood function with conditional probabilities

The treatment proposed by Bunakov [152,153] is completely based on conditional probabilities, of which a summarized interpretation of the idea is given here. In the case that a resonance has the right spin the conditional probability for an observed value $X \pm e$ and the underlying M is again

$$P(x|M) = \frac{1}{\sqrt{2\pi\,(M^2+e^2)}}\exp\left(\frac{-x^2}{2\,(M^2+e^2)}\right). \tag{119}$$

The probability that a resonance has the right spin is given by p, whereas the probability that a resonance has not the right spin is given by $q = 1-p$. The measurements in N resonances are therefore Bernoulli trials: one performs N measurements and each measurement has a chance p to have the right spin in order to follow eq. 119. The likelihood function has to be constructed by taking into account each of these probabilities that r out of N resonances have the right spin for parity nonconservation.

The case with $r = 0$ means that all the resonances have spin 3/2 and cannot show PNC. The prior information is then that $M = 0$. In the likelihood function the total probability is concentrated at zero: $P(M|x) = \delta(M)$, with $\delta(M)$ meaning the Dirac delta function. With $r \neq 0$, one has to shuffle through all the possible combinations of a set K_r, containing the $N!/\,(r!\,(N-r)!)$ equally probable combinations of r values, and weigh this set by the normalized binomial factors $P(K_r)$

$$P(K_r) = \frac{1}{N!/\,(r!\,(N-r)!)}\,\frac{p^r q^{N-r} N!/\,(r!\,(N-r)!)}{1-q^N} = \frac{p^r q^{N-r}}{1-q^N}. \tag{120}$$

This has to be repeated for all the sets K_r with r ranging from 1 to N. Doing so this results in the likelihood function

$$L(M) = P(M|\{x_i\}) = \sum_{r=1}^{N}\left(P(K_r)\sum_{K_r}(pP(M|K_r) + q\delta(M))\right) \tag{121}$$

The term $q\delta(M)$ contributes only at $M = 0$ and is further of little importance for the shape of the likelihood function. So in order to calculate the $L(M)$, one needs to know the functions $P(M|K_r)$, the conditional probability for a particular subset of K_r. This is given by

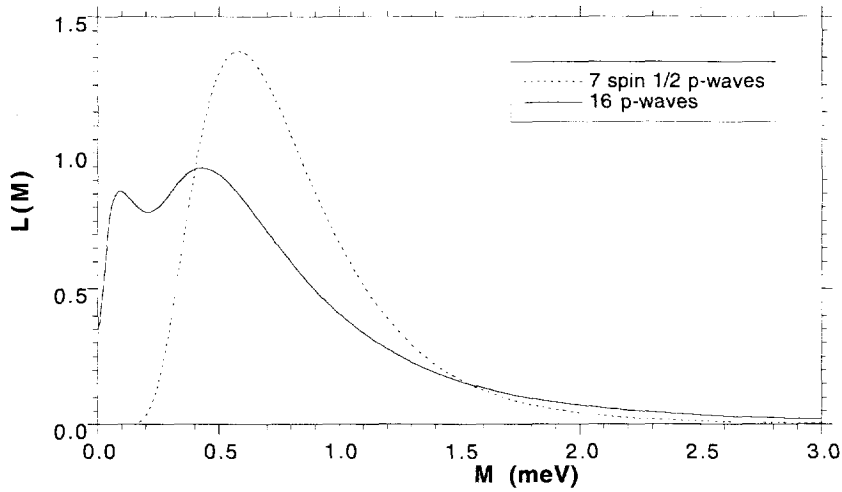

Figure 52: The likelihood function for the sixteen p-wave resonances with spin 1/2 and 3/2, according to the likelihood function of eq. 121, compared to the likelihood function for the seven p-wave resonances.

$$P(M|K_r) = \frac{1}{C_{K_r}} \cdot \prod_{i \in K_r} \frac{1}{\sqrt{2\pi\,(M^2 + e_i^2)}} \exp\left(\frac{-x_i^2}{2\,(M^2 + e_i^2)} \right) u(M) \qquad (122)$$

including the unit step function $u(M)$. The normalization constant C_{K_r} for the subset is given by

$$C_{K_r} = \int_0^\infty \prod_{i \in K_r} \frac{1}{\sqrt{2\pi\,(m^2 + e_i^2)}} \exp\left(\frac{-x_i^2}{2\,(m^2 + e_i^2)} \right) dm. \qquad (123)$$

A data set of N values (X_i, e_i) requires the calculation $2^N - 1$ of these normalization integrals, needed for the evaluation of $L(M)$.

A problem with eq. 123 is that the integrals of this type exist only for $i \geq 2$. For the elements $i = 1$ of the set K_r the integral becomes infinite, corresponding to impossible situation of trying to estimate the variance out of one number. This problem can be avoided by taking a finite interval for the possible range of M, so modifying the prior knowledge about M from the unit step function $u(M)$ into a function with a more subjective upper limit. However, the larger N becomes, the smaller are the binomial factors $P(K_r)$ and the smaller is the contribution of the $i = 1$ elements to the likelihood function eq. 121.

6.6.2 application to the case of ^{238}U

We have implemented this calculation in a recursive computer code, using standard integration algorithms [103] and applied this to the case of the measurements of ^{238}U. There was no noticeable difference between the curve including the $i = 1$ elements with a normalization and the one omitting them. In figure 52 this likelihood function for unknown spins is shown again together with the likelihood function for the seven spin 1/2 p-wave resonances.

An interesting detail is that this function shows two maxima, one at $M = 0.091$ and one at $M = 0.43$ meV. This is due to the fact that here the data of all resonances have a more equal weight than in the case of the likelihood function of eq. 117. The first maximum might be ascribed to the asymmetries of the spin 3/2 p-wave resonances which are not entirely zero, as shown in figure 48. The second maximum can then be attributed to the real asymmetries of the spin 1/2 p-wave resonances. The advantage of this method is that it is not dominated by one data point with a small relative error.

6.7. Concluding remarks

The problem of estimating the expectation value of the root-mean-squared parity nonconserving matrix element M results in a maximum likelihood procedure in the case that the spins of the p-wave resonances are known. We are dealing with a small sample of resonances in the case of parity nonconserving measurements and therefore the estimates are usually biased. Numerical simulations give an indication of the bias and variance of the estimate in the small sample size region. A procedure of bias removal of order $1/N$ with the jackknife method has been applied to the PNC data of spin 1/2 neutron p-wave resonances of ^{238}U which has given a new estimate $M = 0.63$ meV. This value can be used together with eqs. 13 and 14 on page 13 and $D_{1,J=1/2} \approx 39$ eV from page 84 to derive for the ratio of the parity nonconserving and conserving strength in the effective nucleon-nucleon potential $\alpha_P \approx 3\times10^{-7}$.

When the spins are not known, additional assumptions have to be made, notably on the distribution of the resonances that can and cannot show a PNC effect. Two procedures, also based on maximum likelihood have been used until now for the estimation of M in ^{238}U. One of them assigns very large weights to values with small relative errors and the corresponding estimate coincides nearly with the case where the spins are known due to one value. The other estimation procedure accords a more moderate weight resulting in two maxima in the likelihood function, tentatively designated to the contribution of the spin 1/2 and 3/2 p-wave resonance asymmetries. The latter method is quite attractive but a disadvantage is the very long calculation time that is needed to evaluate the likelihood function of eq. 121. This makes it also difficult to apply a bias removal. However, both methods result in the same likelihood function when the spins of the resonances are known.

Conclusions

The knowledge of the spins of neutron resonances is important for the correct analysis of parity nonconservation measurements. The spin assignment method applied in the experiments described in this thesis is the low-level population method where the dependence of the intensity of specific secondary gamma rays on the resonance spin of the compound nucleus, formed by neutron capture, is investigated. This approach works very well for those nuclei in which the gamma decay behaves in a statistical way. The method was already known for its application in the case of *s*-wave resonances. It has now thoroughly been established as a powerful method for spin assignment of *p*-wave resonances which are on the average a factor 1000 weaker than *s*-wave resonances in the epithermal neutron energy range. In addition the observation of primary gamma transitions to levels with known spins has given information about resonance spins.

Spins have been successfully assigned to 19 neutron *p*-wave resonances of ^{238}U, of which seven were found to be $J^{\pi} = 1/2^{-}$. Using only the parity nonconservation data of this spin group, it was possible to determine a more accurate estimate for the root mean squared parity nonconserving matrix element, thus replacing the earlier estimated strength, derived with a procedure containing some assumptions about the resonances.

In the case of ^{113}Cd, spins of 23 neutron *s*-wave resonances as well as of 21 *p*-wave resonances have been determined. Those are essential for the analysis of recently obtained PNC data.

Numerical simulations confirm the resonance spin dependence of the low-level populations and are therefore an important tool for evaluating the feasibility of a spin assignment experiment. However, to obtain reliable results from simulations, it is necessary to dispose of detailed information about the excitation spectrum of the nucleus in the low-lying discrete level region. On the basis of the experience gained in this thesis work, it is recommended to perform first some numerical simulations before undertaking a time consuming spin assignment experiment.

Spin assignment of neutron resonances is not only important for the study of parity nonconservation, but also for future investigations in time reversal invariance in neutron resonances, where the knowledge of resonance spins is required.

Acknowledgements

With pleasure I have stayed for the past three years at the Institute of Reference Materials and Measurements preparing my PhD work. I would like to thank the directors of the Institute, Prof. W. Müller and Prof. A. J. Deruytter, for accepting and supporting this work.

I am very thankful to my thesis advisor Prof. Hans Postma for having introduced me into this interesting field of physics. His large erudition and many discussions have stimulated me a lot. My daily supervisor Franco Corvi familiarized me with the many facets of research and I owe him for the numerous debates which he larded with sundry anecdotes. Together with the skilful technical assistance of Kostas Athanassopulos and in the beginning also Sandro Mauri, it was possible to work within a pleasant and dedicated team.

I am grateful to Yuri Popov and Edouard Sharapov from the JINR in Dubna for the enjoyable collaboration during the experiment on cadmium. I want as well to thank Frantisek Becvar and Pavel Cejnar from Charles University in Prague for their help and cooperation with the program DICEBOX. Also I would like to express my gratitude to Prof. A. van den Bos from Delft University for his constructive remarks about the statistical problems I encountered.

I would like to thank Hermann Weigmann for his support and his accurate reading of the manuscript. I am also indebted to Paul ter Meer for his proficient aid with computing and for keeping me regularly informed about the latest developments in informatics. Also my roommate Olivier Haeberlé helped me to keep seeing things from the bright sight.

Of the many people who have made the realization of this thesis possible I want to mention especially Cesare Cervini, Mick Moxon, Charles Nazareth, Stephan Oberstedt, Peter Rullhusen and the staff from the drawing office, from the workshop and of course the linac operators. I want also to thank the musicians of our local band for the many great moments we had.

Finally, I want to thank Valérie Desbruns, my parents, family and friends for their support and the interest they have shown in my activities.

References

[1] T. D. Lee and C. N. Yang, *Phys. Rev.* **104**, (1956) 254
[2] C. S. Wu et al., *Phys. Rev.* **105**, (1957) 1413
[3] H. Frauenfelder and E. M. Henley, *Subatomic Physics*, Prentice-Hall, London (1991)
[4] M. J. Musolf et al., *Phys. Rep.* **239** (1994) 1
[5] R. Carosi et al., *Phys. Lett.* **B237** (1990) 303
[6] M. Karlsson et al., *Phys. Rev. Lett.* **64** (1990) 2976
[7] E. Ambler et al., *Phys. Rev.* **106** (1957) 1361
[8] H. Postma et al., *Physica* **23** (1957) 259
[9] H. Postma et al., *Physica* **24** (1957) 157
[10] J. H. Christenson et al., *Phys. Rev. Lett.* **13**, (1964) 138
[11] A. Abashian et al., *Phys. Rev. Lett.* **13**, (1964) 243
[12] B. Winstein and L. Wolfenstein, *Rev. Mod. Phys.* **65**(4), (1993) 1113
[13] R. Adler et al., *Phys. Lett.* **B286** (1992) 180
[14] K. S. Krane, *Phys. Rev.* **C4** (1971) 1906
[15] J. Bendahán et al., *Hyperfine Interactions* **34** (1987) 139
[16] C. Broude et al., *Z. Phys.* **A336** (1990) 133
[17] R. P. Feynman and M. Gell-Mann, *Phys. Rev.* **109**, (1958) 193
[18] E. G. Adelberger and W. C. Haxton, *Ann. Rev. Nucl. Part. Sci.* **35**, p.501, (1985)
[19] N. Neubeck et al., *Phys. Rev.* **C10**, (1974) 320
[20] F. Gönnenwein et al., *Nucl. Phys.* **A567**, (1994) 303
[21] Y. G. Abov et al., *Phys. Lett.* **12**, (1964) 25
[22] E. Warming et al., *Phys. Lett.* **25B**(3), (1967) 200
[23] Y. G. Abov et al., *Phys. Lett.* **27B**(1), (1968) 16
[24] E. Warming, *Phys. Lett.* **25B**(9), (1969) 564
[25] Y. G. Abov et al., *Sov. J. Nucl. Phys.* **16**, (1973) 670
[26] J. L. Alberi et al., *Phys. Rev. Lett.* **29**, (1972) 518
[27] M. Forte et al., *Phys. Rev. Lett.* **64B**, (1980) 298
[28] B. Heckel et al., *Phys. Lett.* **119B**, (1982) 298
[29] E. A. Kolomensky et al., *Phys. Lett.* **107B**, (1981) 272
[30] V. P. Alfimenkov et al., *Nucl. Phys.* **A398**, (1983) 93
[31] S. Seestrom et al., Proc. 2nd Int. Sem. on Interaction of Neutrons with Nuclei, Dubna, 26-28 April 1994, in course of publication
[32] J. R. Vanhoy et al., *Z. Phys.* **A333**, (1989) 229
[33] C. R. Gould et al., *Int. J. of Mod. Phys.* **A5**(11), (1990) 2181
[34] A. L. Barabanov et al., *Phys. Rev. Lett.* **70**(9), (1993) 1216
[35] Y. Takahashi et al., *Phys. Lett.* **B326** (1994) 27
[36] H. M. Shimizu, *Nucl. Phys.* **B37a** (1994) 75
[37] V. E. Bunakov and V. P. Gudkov, *Nucl. Phys.* **A401** (1983) 93
[38] O. P. Sushkov and V. V. Flambaum, *Sov. Phys. Usp.* **25** (1982) 1
[39] B. Desplanques, *J. Phys. Colloq.* **45** (1984) 55
[40] H. A. Weidenmüller in *Fundamental Symmetries in Nuclei and Particles*, edited by H. Henrikson and P. Vogel, World Scientific (1989) 30

[41] H. Postma, Proc. 2nd Int. Sem. on Interaction of Neutrons with Nuclei, Dubna, 26-28 April 1994, in course of publication
[42] H. M. Shimizu et al., *Nucl. Phys.* **A552**, (1993) 293
[43] C. M. Frankle et al., *Phys. Rev.* **C46**, (1992) 1542
[44] S. A. Biryukov et al., *Sov. J. Nucl. Phys.* **45**(6), (1987) 937
[45] E. I. Sharapov et al. in *Capture gamma-ray spectroscopy*, edited by R. W. Hoff, AIP (1990) 756
[46] Y. Masuda et al., *Nucl. Phys.* **A504** (1989) 269
[47] C. D. Bowman et al., *Phys. Rev.* **C39** (1989) 1721
[48] V. W. Yuan et al., *Phys. Rev.* **C44** (1991) 2187
[49] J. D. Bowman et al., *Phys. Rev. Lett.* **65**(10), (1990) 1192
[50] X. Zhu et al., *Phys. Rev.* **C46**(2), (1992) 768
[51] C. M. Frankle et al., *Phys. Rev.* **C46**(2), (1992) 778
[52] S. Seestrom, private communication
[53] V. E. Bunakov et al., *Phys. Rev.* **C42**(4), (1990) 1718
[54] M. B. Johnson et al., *Phys. Rev. Lett.* **67**(3), (1991) 310
[55] N. Auerbach, *Phys. Rev.* **C45**(2), (1992) 514
[56] A. Müller and H. L. Harney, *Phys. Rev.* **C45**(4), (1992) 1955
[57] V. V. Flambaum, *Phys. Rev.* **C45**(1), (1992) 437
[58] V. V. Flambaum and O. K. Vorov, *Phys. Rev. Lett.* **70**(26), (1993) 4051
[59] S. E. Koonin et al., *Phys. Rev. Lett.* **69**(8), (1992) 1163
[60] M. H. Urin and O. N. Vyazankin, *Phys. Lett.* **B305** (1993) 187
[61] J. D. Bowman et al., *Annu. Rev. Nucl. Part. Sci.* **43** (1993) 829
[62] J. B. French et al., *Ann. Phys. (N.Y.)* **181** (1988) 198
[63] S. F. Mughabghab et al., *Neutron Cross Sections; Neutron resonance parameters and thermal cross sections*, Academic Press, New York, (1981)
[64] M. S. Moore, *Phys. Rev.* **C18** (1978) 1328
[65] E. R. Reddingius et al., *Nucl. Phys.* **A218** (1974) 84
[66] C. Coceva et al., *Nucl. Phys.* **A117** (1968) 586
[67] G. P. Georgiev et al. in *Capture Gamma-Ray Spectroscopy and related topics*, edited by J. Kern, World Scientific (1993) 581
[68] J. J. Bosman and H. Postma, *Nucl. Instr. Meth.* **148** (1978) 331
[69] H. Postma and J. F. M. Potters, *Physica* **45** (1970) 559
[70] A. J. Ferguson, *Angular Correlation Methods in Gamma-ray Spectroscopy*, North-Holland Publ. Comp., Amsterdam, (1965)
[71] K. J. Wetzel and G. E. Thomas, *Phys. Rev.* **C1**(4), (1970) 1501
[72] W. P. Poenitz and J. R. Tatarczuk, *Nucl. Phys.* **A151** (1970) 569
[73] M. R. Bath et al., *Phys. Rev.* **C2** (1970) 2030
[74] F. Corvi et al., *Nucl. Phys.* **A203** (1973) 145
[75] L. Aldea et al., *Czech. J. of Phys.* **B28** (1978) 17
[76] H. Postma, *Phys. Rev.* **C24**(5), (1981) 2322
[77] B. J. Allen in *Neutron Radiative Capture*, edited by R. E. Chrien, Pergamon Press (1984) 1
[78] A. Bohr and B. R. Mottleson, *Nuclear Structure*, W. A. Benjamin, New York, (1969)
[79] C. E. Porter and R. G. Thomas, *Phys. Rev.* **104** (1956) 483
[80] S. F. Mughabghab in *Neutron Cross Sections and Technology*, edited by J. A. Harvey and R. L. Macklin, Knoxville, Tenn., 1971
[81] M. C. Moxon and J. B. Brisland, *GEEL REFIT. A least squares fitting program for resonance analysis of neutron transmission and capture data*, United Kingdom Atomic Energy Athority, Harwell, (1991)
[82] J. E. Lynn, *The theory of neutron resonance reactions*, Clarendon Press, Oxford, (1968)
[83] K. H. Beckurts and K. Wirtz, *Neutron Physics*, Springer Verlag (1964)

[84] S. Cierjacks, Eds., *Neutron Sources For Basic Physics and Applications* (1983)
[85] K. H. Böckhoff et al., *Nucl. Sci. Eng.* **106** (1990) 192
[86] J. M. Salomé and R. Cools, *Nucl. Instrum. Methods* **179**(1), (1981) 13
[87] J. M. Salomé, *Physicalia* **8**(4), (1986) 261
[88] D. Tronc et al., *Nucl. Instrum. Methods in Phys. Res.* **A228** (1985) 217
[89] A. Brusegan, IRMM, Geel, private communication
[90] C. Coceva et al., ENEA, Bologna, private communication
[91] P. Goedtkindt, *Experimental studies of energy spectra and interference effects of transition readiation sources*, Ph.D Thesis, University of Brussels, 1993
[92] O. Haeberlé, *Electromagnetic radiation generated by an electron interacting with a diffraction grating*, Ph.D Thesis, Université Louis Pasteur, Strasbourg, 1994
[93] C. Wagemans, IRMM, Geel, private communication
[94] F. Corvi, IRMM, Geel, private communication
[95] C. Coceva in *Neutron energy standards for nuclear measurements*, edited by H. Condé, OECD/NEA (1992) 83
[96] Data acquisition system manual, CMTE-FAST Daten Systeme, GmbH, Munich, Germany, 1990
[97] F. Gunsing et al., *DataSort, a listmode sorting application*, Macintosh Scientific and Technical Users Association, Inc., CD-ROM, (1993)
[98] L. A. McNelles and J. L. Campbell, *Nucl. Inst. Methods* **127** (1975) 73
[99] K. Debertin and R. G. Helmer, *Gamma- and X-Ray Spectrometry with Semiconductor Detectors*, North-Holland, Amsterdam, Oxford, New York, Tokyo, (1988)
[100] W. Westmeier, *Elegant computer code*, IRMM, Geel, Belgium, (1982)
[101] I. A. Slavic, *Nucl. Instrum. Methods* **134** (1976) 285
[102] A. J. Ketikian et al., *Nucl. Instrum. Methods in Phys. Res.* **A314** (1992) 578
[103] W. H. Press et al., *Numerical Recipes, The art of scientific computing*, Cambridge University Press, Cambridge, (1989)
[104] F. Becvar and S. Ulbig, *Dicebox computer code*, Charles University, Prague, (1991)
[105] J. J. Collins et al., *Comp. in Phys.* **6**(6), (1992) 630
[106] R. Toral and A. Chakrabarti, *Comp. Phys. Comm.* **74** (1993) 327
[107] M. Hennecke, *Comp. Phys. Comm.* **79** (1994) 261
[108] P. L'Ecuyer, *Comm. of the ACM* **31**(6), (1988) 742
[109] F. James, *Comp. Phys. Comm.* **60** (1990) 329
[110] K. G. Hamilton, *Comp. Phys. Comm.* **75** (1993) 105
[111] K. S. Krane, *Introductory Nuclear Physics*, Wiley & Sons, New York, (1988)
[112] P. M. Endt, *At. Data and Nucl. Data Tables* **26** (1981) 47
[113] J. M. Blatt and V. F. Weisskopf, *Theoretical Nuclear Physics*, Wiley & Sons, New York, (1952)
[114] F. Becvar et al., *Phys. Rev.* **C46**(4), (1992) 1276
[115] J. Honzatko et al. in *Capture Gamma-Ray Spectroscopy and related topics*, edited by J. Kern, World Scientific (1993) 572
[116] G. A. Bartholomew, *Ann. Rev. Nucl. Sci.* **11** (1961) 259
[117] C. M. McCullagh et al., *Phys. Rev.* **C23**(4), (1981) 1394
[118] J. Kopecky and M. Uhl, *Phys. Rev.* **C41**(5), (1990) 1941
[119] B. L. Berman and S. C. Fultz, *Rev. Mod. Phys.* **47**(3), (1975) 713
[120] S. G. Kadmenskii et al., *Sov. J. Nucl. Phys.* **37**(2), (1983) 165
[121] C. Coceva, *Nuovo Cimento* **A107**(1), (1994) 85
[122] J. Kopecky and R. E. Chrien, *Nucl. Phys.* **A468** (1987) 285
[123] P. Cejnar and J. Kern, *Nucl. Phys.* **A561** (1993) 317
[124] W. V. Prestwich et al., *Z. Phys.* **A315** (1984) 103
[125] J. Kopecky, in *Neutron-Capture Gamma-Ray Spectroscopy and Related Topics*, edited by

T. von Egidy et al., Institute of Physics (1981) 426
[126] C. Bloch, *Phys. Rev.* **93**(5) (1954) 1094
[127] A. Gilbert and A. G. W. Cameron, *Can. J. Phys.* **43** (1965) 1446
[128] J. R. Huizenga and L. G. Moretto, *Ann. Rev. Nucl. Sci.* **22** (1972) 427
[129] N. Cerf, *Phys. Rev.* **C50** (1994) 2
[130] N. Cerf, *Nucl. Phys.* **A554** (1993) 85
[131] T. von Egidy et al., *Nucl. Phys.* **A481** (1988) 189
[132] T. von Egidy in *Neutron capture gamma-ray spectroscopy*, (1969) 541
[133] M. R. Schmorak, *Nucl. Data Sheets* **40** (1983) 1
[134] M. R. Schmorak, *Nucl. Data Sheets* **66** (1992) 839
[135] J. Blachot and G. Marguier, *Nucl. Data Sheets* **60** (1990) 139
[136] F. Corvi, F. Gunsing et al. in *Time Reversal Invariance and Parity Violation in Neutron Reactions*, edited by C. R. Gould, J. D. Bowman and Y. Popov, World Scientific (1994) 79
[137] F. Gunsing et al. in *Capture Gamma-Ray Spectroscopy and Related Topics*, edited by J. Kern, World Scientific (1994) 797
[138] F. Corvi, F. Gunsing et al., Proc. Int. Conf. on Nuclear Data for Science and Technology, Gatlinburg, 1994
[139] H. G. Börner et al., *Z. Phys.* **A286** (1978) 31
[140] A. K. Jain et al., *Rev. Mod. Phys.* **62**(2), (1990) 393
[141] O. A. Wasson et al., *Phys. Rev.* **C4**(3), (1971) 900
[142] V. P. Alfimenkov et al., *Sov. J. Nucl. Phys.* **54**(6), (1991) 907
[143] C. M. Frankle et al., *Phys. Rev.* **C45**(5), (1992) 2143
[144] F. Gunsing et al., Proc. 2nd Int. Sem. on Interaction of Neutrons with Nuclei, Dubna, 26-28 April 1994, in course of publication
[145] T. v. Egidy and W. Kaiser, *Z. Phys.* **201** (1961) 378
[146] A. Mheemeed et al., *Nucl. Phys.* **A412** (1984) 113
[147] R. F. Casten et al., *Phys. Lett.* **B297** (1992) 19
[148] C. M. Frankle et al., *Phys. Rev. Lett.* **67**(5), (1991) 564
[149] N. Auerbach and J. D. Bowman, *Phys. Rev.* **C46**(6), (1992) 2582
[150] C. H. Lewenkopf and H. A. Weidenmüller, *Phys. Rev.* **C46**(6), (1992) 2601
[151] V. P. Gudkov, *Phys. Rev.* **C47**(1), (1993) 372
[152] V. E. Bunakov, Report NP-66-1993 1935, Petersburg Nuclear Physics Institute Gatchina (1993).
[153] V. E. Bunakov in *Time Reversal Invariance and Parity Violation in Neutron Reactions*, edited by C. R. Gould, J. D. Bowman and Y. Popov, World Scientific (1994) 61
[154] M. G. Kendall, A. Stuart and K. Ord, *Advanced theory of statistics*, Vol. 2, Hodder & Stoughton, London (1991)
[155] W. T. Eadie et al., *Statistical Methods in Experimental Physics*, North Holland, Amsterdam, (1988)
[156] R. J. Barlow, Statistics, *A Guide to the Use of Statistical Methods in the Physical Sciences*, Wiley & Sons, New York, (1989)
[157] A. Papoulis, Probability, *Random Variables and Stochastic Processes*, McGraw-Hill, (1984)